MAJORANA BOX SYSTEMS: FROM QUANTUM TRANSPORT TO SELF-CORRECTING QUBITS

INAUGURAL-DISSERTATION

ZUR ERLANGUNG DES DOKTORGRADES DER
MATHEMATISCH-NATURWISSENSCHAFTLICHEN FAKULTÄT DER
HEINRICH-HEINE-UNIVERSITÄT DÜSSELDORF

VORGELEGT VON

MATTHIAS GAU

AUS MÖNCHENGLADBACH

DÜSSELDORF, APRIL 2020

Aus dem Institut für Theoretische Physik, Lehrstuhl IV
der Heinrich-Heine-Universität Düsseldorf

Gedruckt mit der Genehmigung der
Mathematisch-Naturwissenschaftlichen Fakultät
der Heinrich-Heine-Universität Düsseldorf

Berichterstatter:

1. Prof. Dr. Reinhold Egger
2. PD Dr. Hermann Kampermann
3. Prof. Dr. Fabian Hassler

Tag der mündlichen Prüfung: 08.07.2020

Abstract

In engineered condensed matter systems, Majorana fermions are realised as quasiparticle excitations, called Majorana bound states, at the surface of the aforementioned topological superconductors. Majorana bound states are their own antiparticles and thereby have zero charge, energy, and no spin. While those properties make them hard to detect, they give rise to several interesting features, such as their non-Abelian exchange statistics. Consequently, Majorana bound states are of immense fundamental interest and applications in quantum information processing are promising.

Within the context of this thesis, Majorana boxes, which are mesoscopic charging islands harbouring Majorana bound states, are considered from two different perspectives. Setups with multiple coupled Majorana boxes, which are connected by short nanowire segments, are key ingredients to recent Majorana qubit and code network proposals. Therefore, the first perspective is concerned with quantum transport in such coupled Majorana box systems. It includes the construction and study of the low-energy theory for multi-terminal junctions with normal leads connected to the coupled box devices. Starting with a single box, where the topological Kondo effect is reproduced, a distinction between simple and non-simple Majorana-lead junctions is made. The latter breaks local fermion parities and thereby results in a low-energy theory, which, in contrast to previously discussed single box systems, is not purely bosonic. Within the scope of this thesis two examples with non-simple Majorana-lead junctions are discussed in terms of their transport characteristics. Those transport signatures can be used to test the nonlocality of Majorana-based systems and thereby the integrity of the underlying Majorana qubits.

The second perspective is given by Majorana boxes in the presence of environmental electromagnetic noise. Coupling the Majorana box setups to quantum dots, one can engineer driven dissipative protocols for stabilisation and manipulation of robust quantum states. Within this thesis it is shown that the time evolution of the Majorana sector is governed by a Lindblad master equation over a wide parameter regime. For a single Majorana box, arbitrary pure states, alternatively dark states, can be stabilised by adjusting suitable gate voltages. If the Majorana box harbours more than four Majorana bound states, the introduced protocols also allow for the stabilisation of fault-tolerant Bell states. Thereby, a single driven dissipative Majorana box works as a self-correcting quantum memory. For devices with two coupled boxes, one can engineer manifolds of degenerate dark states, which allow for the encoding of a dark qubit. For such a qubit, not only the stored quantum information, but also manipulation protocols are protected by the driven dissipative mechanism. Therefore, one can anticipate exceptionally high fault tolerance levels due to a conspiracy of autonomous error correction and topology.

Zusammenfassung

In konstruierten Systemen kondensierter Materie werden Majorana-Fermionen als Quasiteilchenanregungen, sogenannte gebundene Majorana-Zustände, an der Oberfläche der oben genannten topologischen Supraleiter realisiert. Majorana-Anregungen sind ihre eigenen Antiteilchen und haben dadurch keine Ladung, Energie und Spin. Während diese Eigenschaften es schwierig machen Majorana-Zustände zu detektieren, führen diese zu interessanten Merkmalen, wie zum Beispiel ihrer nicht-Abelschen Austauschstatistik. Folglich sind Majorana-Zustände von grundlegendem Interesse und Anwendungen in der Quanteninformationsverarbeitung sind vielversprechend.

Im Rahmen dieser Arbeit werden mesoskopische Ladungsinseln mit Majorana-Zuständen, sogenannte Majorana-Boxen, unter zwei verschiedenen Aspekten betrachtet. Systeme aus mehreren gekoppelten Majorana-Boxen, welche durch kurze Nanodrahtsegmente verbunden sind, sind wichtige Bestandteile jüngster Vorschläge für Majorana-basierte Quanten-Bits und Code-Netzwerke. Daher besteht der erste Aspekt aus Quantentransport durch Systeme aus gekoppelten Majorana-Boxen. Dieser umfasst die Konstruktion und Analyse der Niedrigenergietheorie für normale Leitungen, welche an die gekoppelten Boxen angeschlossen sind. Ausgehend von einer einzelnen Box, in der der topologische Kondo-Effekt auftritt, wird zwischen einfachen und komplexen Majorana-Kontakten unterschieden. Letztere brechen lokale Fermionparitäten und führen dadurch zu einer Niedrigenergietheorie, die im Gegensatz zu zuvor diskutierten Systemen aus einzelnen Boxen nicht rein bosonisch ist. Im Rahmen dieser Arbeit werden zwei Beispiele mit komplexen Majorana-Kontakten hinsichtlich ihrer Transporteigenschaften diskutiert. Diese Vorhersagen können verwendet werden, um die Nichtlokalität von Majorana-basierten Systemen und damit die Integrität der zugrunde liegenden Majorana Quanten-Bits zu testen.

Der zweite Aspekt besteht aus Majorana-Boxen unter Berücksichtigung des elektromagnetischen Hintergrundes. Durch die Kopplung der Majorana-Boxen an Quantenpunkte können getriebene dissipative Protokolle zur Stabilisierung und Manipulation robuster Quantenzustände entwickelt werden. In dieser Arbeit wird gezeigt, dass die zeitliche Entwicklung des Majorana-Sektors über ein breites Parameterregime durch eine Lindblad-Mastergleichung beschrieben ist. Für eine einzelne Majorana-Box können beliebige reine Zustände, auch dunkle Zustände genannt, durch Einstellen geeigneter Gatespannungen stabilisiert werden. Wenn die Box mehr als vier Majorana-Zustände enthält, ermöglichen die eingeführten Protokolle auch die Stabilisierung fehlertoleranter Bell-Zustände. Dabei arbeitet eine einzelne getrieben-dissipative Majorana-Box als selbstkorrigierender Quantenspeicher. Für Systeme mit zwei gekoppelten Boxen kann man Mannigfaltigkeiten entarteter dunkler Zustände konstruieren, die die Kodierung eines dunklen Quanten-Bits ermöglichen. Für ein solches Qubit werden nicht nur die gespeicherte Quanteninformation, sondern auch Manipulationen durch den getrieben-dissipativen Mechanismus geschützt. Daher kann man aufgrund eines Zusammenspiels von autonomer Fehlerkorrektur und Topologie außergewöhnlich hohe Fehlertoleranzniveaus erwarten.

Contents

Chapter 1

Introduction

The story of the Majorana fermion started more than 80 years ago, when Italian physicist Ettore Majorana formulated a real solution of the Dirac equation, [Majorana, 1937]. What at first might seem to be a technicality, indeed has sincere consequences for the quantum mechanical particle, whose wave function obeys Dirac's equation. One of those consequences is a Majorana fermion being its own antiparticle. The hermitian conjugate of a Majorana is the operator itself, and thereby creation and annihilation of a Majorana fermion correspond to equal physical processes. Inevitably, a Majorana fermion then has to be charge-neutral.

Even though the first proposals for Majorana fermions were formulated in the context of particle physics, 20 years ago ideas appeared on how to obtain such fermions as low-energy quasiparticles in condensed matter systems. In [Reed, 2000], Majorana bound states are shown to appear in vortices of two-dimensional chiral p-wave superconductors. Within the presented thesis the focus lies on one-dimensional systems, where the pioneering ideas were conceived by Alexei Kitaev in [Kitaev, 2001]. He showed that in an one-dimensional lattice with nearest-neighbour interaction and p-wave pairing, there exist a certain parameter regime in which Majorana bound states appear at the edge of the chain. Consequently, the corresponding phase is referred to as topological.

For almost 10 years the proposals of Kitaev remained purely theoretical and elusive as there are no p-wave superconductors in nature. In 2010, Oreg, *et al.*, [Oreg, 2010], and Lutchyn, *et al.*,[Lutchyn, 2010], established an one-dimensional nanowire construction of Kitaev's lattice toy model. Here, strong spin-orbit coupling with a Zeeman field allows the semiconductor nanowire to become effectively spinless. When proximitised by a conventional s-wave superconductor, this leads to p-wave superconductivity. This led to rapid progress in the Majorana field. In [Mourik, 2012] first experimental signatures of Majorana bound states were reported. In the following years, different signatures, like the ground-state degeneracy, [Albrecht, 2016], or resonant transport signatures, see [Nichele, 2017] and [Zhang, 2018], were observed. Although several groups have confirmed those findings, a conclusive experiment is still to be carried out. Good candidates for such experiments are braiding of Majorana excitations to reveal their non-abelian statistics, cf. [Alicea, 2012], or the topological Kondo effect, see [Béri, 2012] and [Altland, 2013].

Majorana bound states are not only of fundamental interest, but could also become useful tools for quantum computation. Here, Majorana devices can be used as topologically protected quantum memory, or alternatively, in [Alicea, 2011] discussed braiding protocols allow for the implementation of protected gates. Furthermore, based on the one-dimensional nanowire construction, [Plugge, 2017] and [Karzig, 2017] proposed a floating island harbouring at least four Majorana excitations to serve as elementary building block for several quantum error correcting platforms. As Majorana-based implementations, [Landau, 2016], are expected to have a reduced overhead in quantum error correction compared to conventional platforms, [Terhal, 2015], they could become essential for the long-term goal of achieving large-scale, fault-tolerant quantum computers.

As coupling multiple Majorana islands is key for the construction of surface codes, chapter 3 provides details on transport in such coupled Majorana box systems when probed by normal-conducting leads. These transport experiments could become essential for testing larger topological networks. Here the theoretical framework is introduced allowing for an extensive study of an arbitrary coupled box setup. Furthermore, it contains details on two examples; one being the loop qubit, proposed in [Karzig, 2017], and a two-tetron device, which is the minimal coupled box setup allowing for the implementation of an entangling gate.

In chapter 4, the Majorana island is revisited in the context of an open quantum system. Electromagnetic fluctuations, which are present in any Majorana experiment, provide a natural way for dissipation. By carefully engineering the Majorana system, one can benefit from the dissipation, and thereby, establish a driven dissipative protocol, which autonomously stabilises the Majorana qubit. Whereas the native Majorana qubit relies on active error correction, the driven dissipative version stabilises quantum states for an indefinite time. Furthermore, such open systems allow for the stabilisation of a degenerate state manifold - a dark space. As long as state manipulation protocols remain in the dark space, one could achieve self-correcting quantum computation, making the need for active error correction obsolete.

In chapter 5, the contribution of this work to quantum transport and quantum computation in Majorana box systems is summarised. Here, the different results are linked to current developments towards achieving topological quantum computation. Furthermore, this chapter concludes with an outlook on interesting future research. Especially for the driven dissipative Majorana devices, several conceptually different directions to pursue are presented.

Whenever possible, this thesis provides details on general techniques or results, which can be transferred to other problems in the context of Majorana boxes. Therefore, within this thesis any general concept is described by conventional letters, e.g. H for an arbitrary Hamiltonian, whereas caligraphic symbols refer to specific examples, e.g. $\mathcal{H}_{\mathrm{dot}}$ describing the Hamiltonian of a certain quantum dot. All three publications included in this thesis can be found in the attachment.

Chapter 2

Fundamental Principles

This chapter provides the foundation necessary to understand the calculations and effects explained in chapters 3-4. Beginning with Majorana fermions as a real solution to the Dirac equation, their general properties are introduced. In condensed matter systems superconducting systems turn out to be good candidates for hosting Majorana fermions. Therefore a famous lattice toy model (Kitaev chain), which connects the existence of Majorana excitations to p-wave superconductivity and thereby topological superconductors are discussed. Based on the ideas of this toy model, an one-dimensional nanowire realisation of such topological superconductors is considered, as it provides the primary ingredient for all systems of interest in this thesis. Since the topological degeneracy due to Majorana zero modes is fragile in terms of single electron tunneling events, multiple topological superconductors can be protected by charging effects. For this purpose, the general mechanism of addressing Majorana fermions on such charging islands is introduced. Furthermore, the protection by charging effects allows for a simplification of the representation of Majorana operators by Pauli operators. The corresponding spin structure on such charging islands is then studied in terms of quantum transport. Here, the most important techniques are introduced in order to prepare for chapter 3. Moreover, the nonlocality of the Majorana fermions gives rise to the topological Kondo effect, which emerges for a single charging island being addressed by more than three leads. The concepts introduced here are then generalised in chapter 3 for a network of Majorana islands. Because of the duality between a spin-1/2 particle and a qubit, such Majorana charging islands form Majorana box qubits. In order to discuss these systems with respect to quantum computation, quantum gates will be introduced. Afterwards the Majorana platform is analysed in terms of the requirements for quantum computers. This will serve as a starting point for chapter 4, where an additional protection mechanism will be introduced, leading to self-stabilising Majorana qubits. In order to achieve this, the environment of the qubit will no longer be neglected and the system will be considered open. Therefore, the general description of open quantum systems by Lindblad master equations is introduced here. First, the microscopic derivation of such a master equation is shown. Afterwards, two different approaches of determining the steady-state solution and characteristic times of approaching that solution are presented.

2.1 Majorana fermions in condensed matter systems

This subsection is dedicated to Majorana fermions as (quasi-)particles, which are of fundamental interest. Starting in Sec. 2.1.1 with Ettore Majorana's original discovery of a real solution to the Dirac equation in 1937, [Majorana, 1937], the defining properties of Majorana fermions and their consequences are discussed. After a short detour over condensed matter systems, which fail to host Majorana fermions, Kitaev's lattice toy model [Kitaev, 2001] is presented in Sec. 2.1.2. In this toy model the emergence of Majorana fermions is linked to the existence of effective spinless superconductivity. Therefore, Sec. 2.1.3 contains an 1D wire proposal, [Oreg, 2010] and [Lutchyn, 2010], which can be seen as an experimentally feasible realisation of the toy model introduced by Kitaev.
This subsection is loosely based on the excellent reviews by Alicea [Alicea, 2012], Leijnse and Flensberg [Leijnse, 2012] and Beenakker [Beenakker, 2013].

2.1.1 Majorana fermions

In [Majorana, 1937] Ettore Majorana discussed the Dirac equation

$$(i\gamma^{\mu}\partial_{\mu} - m)\,\psi(x) = 0. \tag{2.1}$$

Here, $\psi(x)$ is the wave function of a particle with mass m and x being a four-vector. If the matrices $\{\gamma^{\mu}\}$ obey

$$\{\gamma^{\mu}, \gamma^{\nu}\} = 2g^{\mu\nu} I_4, \qquad \gamma^0\gamma^{\mu}\gamma^0 = (\gamma^{\mu})^{\dagger} \tag{2.2}$$

the wave function corresponds to a particle with spin $\frac{1}{2}$. In the above equation $g^{\mu\nu} = diag\,(1, -1, -1, -1)$ and $I_4 = diag\,(1, 1, 1, 1)$ were used. Conventionally one solves Eq. (2.1) with the γ-matrices in the Dirac-Pauli representation. Nevertheless Ettore Majorana changed the game switching to a different basis, which is now called the Majorana representation:

$$\gamma^0 = \begin{pmatrix} 0 & \sigma^2 \\ \sigma^2 & 0 \end{pmatrix}, \quad \gamma^1 = \begin{pmatrix} i\sigma^1 & 0 \\ 0 & i\sigma^1 \end{pmatrix}, \quad \gamma^2 = \begin{pmatrix} 0 & \sigma^2 \\ -\sigma^2 & 0 \end{pmatrix}, \quad \gamma^3 = \begin{pmatrix} i\sigma^3 & 0 \\ 0 & i\sigma^3 \end{pmatrix}, \tag{2.3}$$

where σ^j are Pauli matrices. One can check that the γ matrices in Eq. (2.3) behave in accordance with Eq. (2.2). Thereby the solution of the Dirac equation in Majorana representation still describes a spin-1/2 particle. Furthermore all the above γ matrices have purely imaginary eigenvalues, resulting in Ettore Majorana's discovery of a real solution of the Dirac equation, $\psi^*(x) = \psi(x)$ [Majorana, 1937]. The importance of this result can be observed when thinking of the transformation between a particle and its antiparticle. This transformation involves complex conjugation of the respective field. Thus, the particle Ettore Majorana proposed can be seen as its own antiparticle. Because of this feature and the fractional spin the particle should have, one nowadays calls them *Majorana fermions* (MFs).
The above mentioned properties of MFs are relatively general, which is why there are numerous proposals for MFs spread over different fields in physics. Ettore Majorana originally thought about neutrinos being MFs. Even 80 years after the first formulation of this idea, it is still pursued in the high-energy community, [Avignone, 2008]. Here, researchers all over the world are trying to detect a neutrinoless double beta decay, which is only possible if neutrinos are indeed their own antiparticles. A very different approach

emerged in the condensed matter community, where MFs are considered to be quasiparticle excitations. Therefore the constituents of a MF in condensed matter systems are electrons and ions.

The idea of a MF being a quasiparticle paves the way for various proposals of realising such excitations. In a normal metal there are electrons and holes, which are able to annihilate each other. In the language of second quantisation this implies $c_s^\dagger$ creating an electron with spin s and c_s annihilating an electron. Alternatively, c_s creates a hole with spin s. Since electron and hole have opposite charges, which corresponds to c_s being non-hermitian, charge prevents a metal from hosting MFs. One can look at other quasiparticles in condensed matter systems such as in superconductors. In conventional superconductors electrons with opposite spin can pair up to form Cooper pairs, which then constitute the ground-state. This conventional pairing mechanism is called s-wave, since it involves opposite spin. Furthermore the spontaneous formation of Cooper pairs breaks charge conservation, which allows for the appearance of Bogoliubov quasiparticles, which are superpositions of electrons and holes

$$d = uc_\uparrow^\dagger + vc_\downarrow . \tag{2.4}$$

Conjugating Eq. (2.4) one obtains $d^\dagger = u^* c_\uparrow + v^* c_\downarrow^\dagger$. This implies that even if u and v are real-valued the spin still prevents these quasiparticles from being MFs. Unfortunately superconductivity in nature appears due to s-wave pairing of electrons, but the idea of effectively spinless superconductivity raised the Majorana field. This idea was first formulated by Alexei Kitaev in 2001 [Kitaev, 2001], where he introduced a toy model to discuss the emergence of MFs in a condensed matter system.

2.1.2 Kitaev chain

The starting point of the toy model introduced by Alexei Kitaev in [Kitaev, 2001] is an 1D lattice model with spinless electrons. Following the discussion in [Alicea, 2012] and [Leijnse, 2012] we start with the Hamiltonian

$$\mathcal{H}_{\text{chain}} = -\sum_k \mu_k c_k^\dagger c_k - \frac{1}{2}\sum_k \left(t c_k^\dagger c_{k+1} + \Delta e^{i\phi} c_k c_{k+1} + \text{h.c.} \right), \tag{2.5}$$

where c_k is the annihilation operator of an electron in site k. The chemical potential μ_k can be varied to change the occupation number $n_k = c_k^\dagger c_k$ in site k. Even though the ability to tune the chemical potential at any site individually will be crucial for braiding operations [Nayak, 2008], for the purpose of this chapter it also suffices to assume the isotropic case, where $\mu_k = \mu$. The next term in Eq. (2.5) describes nearest-neighbour hopping with amplitude t. The last term represents superconducting pairing of nearest-neighbour electrons with pairing strength Δ and phase ϕ. Since the electrons do not have spin, the pairing mechanism is p-wave, which is why this lattice model is of toy nature.

One elegant way to discuss the physics of this toy model is to switch from the Dirac to the MF representation. As discussed in Sec. 2.1.1, a MF is a real solution to the Dirac equation. One can use this result to write any Dirac fermion in terms of Majoranas, where the latter are essentially the real and imaginary part of the Dirac fermion. In the above model this basis change can be achieved by writing

$$c_k = \frac{e^{-i\frac{\phi}{2}}}{2} \left(\gamma_{k,2} + i\gamma_{k,1} \right). \tag{2.6}$$

Eq. (2.6) implies that there are now two MFs in site k. Moreover it reflects a consequence of the Majorana property, which was only implicitly mentioned in Sec. 2.1.1, that is: MFs are charge-neutral. The charge degree of freedom on the right side of Eq. (2.6) is hidden in the exponential prefactor. One can also invert the expression and thereby obtain

$$\gamma_{k,1} = -i\left(e^{i\frac{\phi}{2}}c_k - e^{-i\frac{\phi}{2}}c_k^\dagger\right), \qquad \gamma_{k,2} = e^{i\frac{\phi}{2}}c_k + e^{-i\frac{\phi}{2}}c_k^\dagger \tag{2.7}$$

With the above definitions one can check the defining properties of a MF. They are fermions, because the Dirac fermion algebra $\{c_k, c_l^\dagger\} = c_k c_l^\dagger + c_l^\dagger c_k = \delta_{kl}$ implies that the Majorana operators obey the Clifford algebra $\{\gamma_m, \gamma_n\} = 2\delta_{mn}$. Moreover, this in combination with Eq. (2.7) leads to a Majorana being its own antiparticle, because creation and annihilation are the exact same operations, i.e. $\gamma_m^2 = \gamma_m^\dagger \gamma_n = 1$. Here, another consequence of the Majorana property is shown: MFs have no well-defined occupation number. A Majorana mode is always empty and occupied at the same time, since $\gamma_m^\dagger \gamma_m = \gamma_m \gamma_m^\dagger = 1$. Such observations in condensed matter systems lead to the conclusion that a MF is an equal superposition of an electron and a hole, which is reflected in Eq. (2.7).

Writing the Hamiltonian in Eq. (2.5) in Majorana representation, one obtains

$$\mathcal{H}_{\text{chain}} = -\frac{1}{2}\sum_{k=1}^{N}\mu_k\left(1 + i\gamma_{k,2}\gamma_{k,1}\right) - \frac{i}{4}\sum_{k=1}^{N-1}\left[(\Delta + t)\gamma_{k,2}\gamma_{k+1,1} + (\Delta - t)\gamma_{k,1}\gamma_{k+1,2}\right] \tag{2.8}$$

This change of representation corresponding to a decomposition of Dirac fermions into Majoranas is depicted in Fig. 2.1. The above Hamiltonian includes operators of the form $i\gamma_{k,1}\gamma_{k,2}$, which, in contrast to the occupation number, have a well-defined eigenvalue. In literature, this eigenvalue is referred to as the Majorana parity, because it relates to the occupation of the complex fermion formed by the two Majoranas, i.e. $i\gamma_{k,1}\gamma_{k,2} = 1 - 2c_k^\dagger c_k$ [Leijnse, 2012]. Whereas the first term in Eq. (2.8) relates to the occupation of the electron in site k, the second and third term correspond to the occupation of Dirac fermions, which are not localised on a single site. This observation by Kitaev [Kitaev, 2001] manifests in different physical situations depending on the parameters μ_k, Δ and t. In order to clarify the physics of this model one can therefore look at the two limiting cases, which lead to different phases.

First, without hopping and pairing, i.e. $\Delta = t = 0$, the excitations are confined to their respective sites. If one furthermore assumes the case of an isotropic chemical potential ($\mu_k = \mu$), the Hamiltonian is given by

$$\mathcal{H}^1_{\text{chain}} = -\frac{\mu}{2}\sum_{k=1}^{N}\left(1 - i\gamma_{k,1}\gamma_{k,2}\right) = -\mu\sum_{k=1}^{N}c_k^\dagger c_k. \tag{2.9}$$

For a negative chemical potential, $\mu < 0$, the occupation of any of the original sites costs precisely μ. Therefore, the ground state without hopping and pairing is given by an empty chain, i.e. $n_k = c_k^\dagger c_k = 0$.

The second limiting case is given by the complete opposite, where no chemical potential favours the occupation of any site, i.e. $\mu = 0$. Thus, the physics is governed by hopping and pairing, which for simplicity are assumed to be of equal strength, $t = \Delta \neq 0$. In this case the last term in Eq. (2.8) is suppressed and one obtains

$$\mathcal{H}^2_{\text{chain}} = -\frac{t}{2}\sum_{k=1}^{N-1} i\gamma_{k,2}\gamma_{k+1,1} = t\sum_{k=1}^{N-1}\left(\tilde{c}_k^\dagger \tilde{c}_k - \frac{1}{2}\right). \tag{2.10}$$

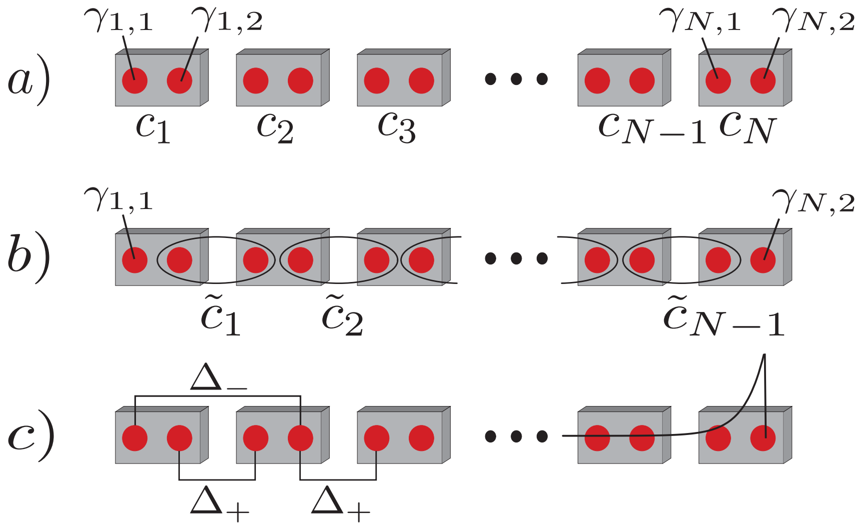

Figure 2.1: Schematic sketch of Kitaev's 1D lattice toy model. a) The fermionic sites (grey boxes) can be decomposed into MFs (red dots). Pairing the Majoranas on the same site leads to the topologically trivial phase. b) In the case of $\mu = 0$ and $t = \Delta \neq 0$ the ground state is formed by pairing MFs belonging to neighboring sites. The pairing is indicated by ovals, which then form the new $\tilde{c}_j$ fermions. At the very end of the chain two Majorana zero modes appear. The corresponding phase is topological. c) For $\Delta \neq t$ the two different coupling mechanisms in Eq. (2.8) are indicated as $\Delta_\pm = \Delta \pm t$. Their competition leads to an exponentially decaying Majorana wave function, which is shown on the right side of the chain. Based on [Leijnse, 2012].

It is important to note that in the above Hamiltonian only $N-1$ Majorana parities appear, because the toy model Hamiltonian in Eq. (2.5) does not pair the ends of the chain. Thus, pairing and hopping leaves two MFs untouched. The Hamiltonian can be diagonalised by constructing new Dirac fermions out of the coupled Majoranas according to $\tilde{c}_k = (\gamma_{k+1,1} + i\gamma_{k,2})/2$, see Fig. 2.1. Therefore, the new Dirac fermions are due to non-local pairing in terms of the original sites of the chain. Moreover, it now requires energy t to occupy the new fermionic mode $\tilde{c}_k^\dagger \tilde{c}_k$, which implies that the ground state is given by zero excitations in terms of the new Dirac fermions.

The main difference of this limit, compared to the situation in Eq. (2.9), is that the ground state here is given by $N-1$ empty modes. Therefore, the different phase originates from the fact that the MFs at the end are unpaired. Since they are absent from the Hamiltonian in Eq. (2.10), both Majoranas cost zero energy. In literature they are often referred to as *Majorana zero modes* (MZMs) [Alicea, 2012]. In analogy to the previous formation of Dirac fermions, one can construct a Dirac fermion out of the two MZMs, i.e. $f = (\gamma_{N,2} + i\gamma_{1,1})/2$. This new fermion is highly non-local in the sense that its constituents are located at the very beginning and end of the chain, which in principle could be infinitely long. Furthermore this non-local fermionic mode f, which costs zero energy, can either be empty or occupied - corresponding to $i\gamma_{1,1}\gamma_{N,2} = \pm 1$. Consequently, the ground state is two-fold degenerate and the two states differ only in their fermion parity. Since this ground-state degeneracy is due to the appearance of MZMs and therefore owed to the geometry of the system, it is called *topological degeneracy* [Nayak, 2008].

The two distinct phases discussed above are called (topologically) trivial and topological, where the topology comes from the existence of MZMs. Because electron pairing is essential, one can also distinguish between a conventional and a topological superconductor.

Due to the topological degeneracy, the latter can even exhibit odd-parity superconductivity, which in conventional superconductors is not possible, because the ground state is formed by Cooper pairs only.

Lifting the above constraints on both limits, i.e. for $\mu \neq 0$ and $\Delta \neq t \neq 0$, the situation changes slightly. For example, even if hopping and pairing is allowed, an infinitely strong chemical potential can lift the topological degeneracy leading to the trivial phase. On one hand, in [Kitaev, 2001] it was shown that the Majorana modes remain as long as the chemical potential is placed inside the gap, i.e. for $|\mu| < 2t$. On the other hand, even if μ is sufficiently small and the hopping and pairing are not of equal strength, one observes two different pairing mechanisms. In Eq. (2.8) we see that the second term ($\propto \Delta + t$) favours coupling of the inner Majoranas of different sites. On the contrary, the third term ($\propto \Delta - t$) favours pairing of outer Majoranas of different sites. In a 1D system the last coupling mechanism is naturally weaker, as Fig. 2.1 suggests. Nevertheless the competition between both pairing mechanisms leads to the Majorana mode being not completely localised at the ends of the lattice. In [Kitaev, 2001] it was shown that for a finite chain length L the Majorana wave function will decay exponentially from the edges $\propto e^{-L/\xi}$, where ξ is the Majorana localisation length. This length is proportional to the ratio of the above mentioned two processes, which is why the modes are sharply localised for $\Delta = t$ since $\xi \to 0$. Therefore, even in the toy model the chain has to be sufficiently long in order for the two *Majorana bound states* (MBSs) not to overlap and thereby physically pair. This pairing would lift the topological degeneracy.

The importance of this toy model can be observed by summarising the ingredients needed for topological superconductivity. The required geometry for the appearance of MBSs is a hard boundary, which is of no difficulty in realisation. The nearest-neihbour hopping is of no problem as well. The bottleneck of the model is given by the p-wave pairing, since electrons naturally come with a spin. Therefore, in 2001 Kitaev changed the question about how to obtain MFs in condensed matter systems to the question of how to obtain an effective p-wave superconductor. His paper [Kitaev, 2001] marks the beginning of Majorana physics in condensed matter, which is why the here discussed toy model is famously known as *Kitaev chain*.

2.1.3 Nanowire realisation

After the reformulation of the problem by Kitaev in 2001 it took nearly a decade for a feasible 1D proposal. In 2010 two groups independently came up with the same idea of an effective 1D p-wave superconductor, [Lutchyn, 2010] and [Oreg, 2010]. Their proposal is based on a 1D semiconducting nanowire, which is proximitised by an s-wave superconductor.

Following [Leijnse, 2012] one can start with the nanowire, where the respective Hamiltonian is given by

$$\mathcal{H}_0 = \sum_{\sigma=\uparrow,\downarrow} \int dr\, \psi_\sigma^\dagger(\boldsymbol{r}) H_0(\boldsymbol{r}) \psi_\sigma(\boldsymbol{r}), \tag{2.11}$$

with the single-particle Hamiltonian in its first quantised form

$$H_0(\boldsymbol{r}) = \frac{\boldsymbol{p}^2}{2m} - \mu + \alpha\, (\boldsymbol{E}(\boldsymbol{r}) \times \boldsymbol{p}) \cdot \boldsymbol{\sigma} + \frac{1}{2} g \mu_B \boldsymbol{B}(\boldsymbol{r}) \cdot \boldsymbol{\sigma}. \tag{2.12}$$

Here, m denotes the effective electron mass, μ is the chemical potential and the electrons momentum is given by $\boldsymbol{p}$. Furthermore, Eq. (2.12) includes spin-orbit interaction of strength α. Thus, $\boldsymbol{E}(\boldsymbol{r})$ is the electric field felt by the valence electrons. The last term describes an applied magnetic field $\boldsymbol{B}(\boldsymbol{r})$. g is the Landé g-factor and μ_B is the Bohr magneton. Finally, $\boldsymbol{\sigma}$ is a vector of Pauli matrices. As Eq. (2.11) indicates, the electrons have a spin and the here defined Hamiltonian is very general.

This nanowire is placed near the surface of a conventional s-wave superconductor, see Fig. 2.2. Therefore electrons can tunnel between both systems, which results in the wire's electrons sensing an effective 'proximity-induced' superconducting pairing field. The corresponding pairing Hamiltonian for the wire electrons can be written as

$$\mathcal{H}_S = \int dr\, dr'\, \psi_\downarrow(\boldsymbol{r})\Delta(\boldsymbol{r},\boldsymbol{r'})\psi_\uparrow(\boldsymbol{r'}) + \text{h.c.} \tag{2.13}$$

with pairing potential $\Delta\left(\boldsymbol{r},\boldsymbol{r'}\right)$. The Hamiltonian $\mathcal{H}_{\text{1D}}$ of the proximitised nanowire, which is exposed to an external electric and magnetic field, is then given by the sum of the two Hamiltonians, i.e. $\mathcal{H}_0 + \mathcal{H}_S$.

In order to study this system it is important to access the quasiparticle excitations, for which one needs to solve the Bogoliubov de Gennes equations. Thus, it is convenient to introduce Nambu spinors

$$\overline{\psi}(\boldsymbol{r}) = \begin{pmatrix} \psi_\uparrow(\boldsymbol{r}) \\ \psi_\downarrow(\boldsymbol{r}) \\ \psi_\downarrow^\dagger(\boldsymbol{r}) \\ -\psi_\uparrow^\dagger(\boldsymbol{r}) \end{pmatrix} \qquad \overline{\psi}^\dagger(\boldsymbol{r}) = \begin{pmatrix} \psi_\uparrow^\dagger(\boldsymbol{r}) \\ \psi_\downarrow^\dagger(\boldsymbol{r}) \\ \psi_\downarrow(\boldsymbol{r}) \\ -\psi_\uparrow(\boldsymbol{r}) \end{pmatrix} \tag{2.14}$$

and rewrite the total Hamiltonian of the nanowire as

$$\mathcal{H}_{\text{1D}} = \frac{1}{2}\int dr\, dr'\, \overline{\psi}^\dagger(\boldsymbol{r})\left[\overline{H}_0(\boldsymbol{r})\delta(\boldsymbol{r}-\boldsymbol{r'}) + \overline{\Delta}(\boldsymbol{r},\boldsymbol{r'})\right]\overline{\psi}(\boldsymbol{r'}). \tag{2.15}$$

Here, one defines two new 4×4 matrices according to

$$\overline{H}_0 = \begin{pmatrix} H_0(\boldsymbol{r})_{11} & H_0(\boldsymbol{r})_{12} & 0 & 0 \\ H_0(\boldsymbol{r})_{21} & H_0(\boldsymbol{r})_{22} & 0 & 0 \\ 0 & 0 & -H_0^*(\boldsymbol{r})_{11} & -H_0^*(\boldsymbol{r})_{12} \\ 0 & 0 & -H_0^*(\boldsymbol{r})_{21} & -H_0^*(\boldsymbol{r})_{22} \end{pmatrix}, \qquad \overline{\Delta}(\boldsymbol{r},\boldsymbol{r'}) = \begin{pmatrix} 0 & 0 & \Delta^* & 0 \\ 0 & 0 & 0 & \Delta^* \\ \Delta & 0 & 0 & 0 \\ 0 & \Delta & 0 & 0 \end{pmatrix}. \tag{2.16}$$

Since the here introduced Nambu space includes electron-hole space, one observes that the lower-right of $\overline{H}_0$ is the time-reversal of the upper-left, because holes are time-reversed electrons. So far, the problem was only reformulated and switching to Nambu space did not change any of the physics. It rather provides a convenient matrix representation. Nevertheless one explicitly includes hole excitations, which were absent in Eq. (2.11). Therefore, the reformulation doubled the number of eigenstates, reflecting that there is an underlying symmetry here. This is electron-hole symmetry relating eigenstates corresponding to electronic excitations to their hole counterpart.

Moreover, Eq. (2.15) now allows one to solve the Bogoliubov de Gennes equations for eigenstates $\overline{\psi}_i(\boldsymbol{r})$:

$$\overline{H}_0(\boldsymbol{r})\overline{\psi}_i(\boldsymbol{r}) + \int dr'\, \overline{\Delta}(\boldsymbol{r},\boldsymbol{r'})\overline{\psi}_i(\boldsymbol{r'}) = E_i\overline{\psi}_i(\boldsymbol{r}) \tag{2.17}$$

Conventionally Eq. (2.17) is diagonalised by a Bogoliubov transformation. Even though one could solve Eq. (2.17) in its general form, for the purpose of discussing an effective p-wave superconductor it suffices to simplify the above Hamiltonians by making some assumptions about the specific system.

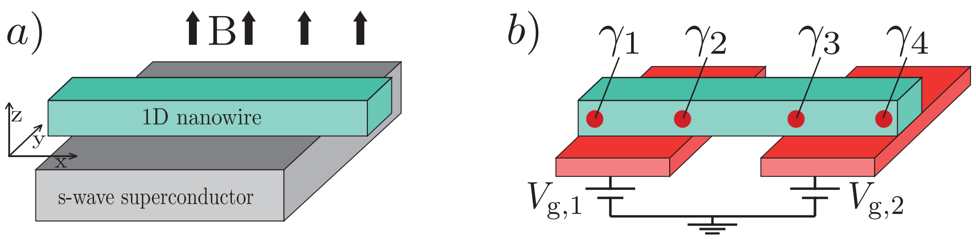

Figure 2.2: Schematic sketch of a topological p-wave superconductor. a) 1D nanowire is placed on top of a conventional s-wave superconductor. The applied magnetic field is chosen to be along the z-direction and the electric field is not shown. One can tune the chemical potential inside the wire by a set of gate electrodes, which are not shown in a), but would be on top of the wire. b) Same sketch as a) but rotated by π about the x-axis. Now the gate electrodes are shown and the superconductor is hidden. If the gate voltages $V_{\mathrm{g,j}}$ are tuned in such a way that the chemical potential in the respective region of the wire lies within the gap (discussed in the main text), the 1D wire will host four MZMs with operators γ_k with $k = 1, \dots, 4$. Based on [Alicea, 2012] and [Leijnse, 2012].

As Fig. 2.2 suggests, one can assume the 1D wire to be along the x-direction. Thus, for a true 1D system the only relevant momentum is given by k_x. The one-dimensionality comes from tuning the chemical potential by a set of gate voltages (shown in Fig. 2.2) to a regime, where only a single 1D subband is occupied. Furthermore, the wire is assumed to be long enough for quantisation effects to be neglected along the wire direction and thin enough not to occupy additional subbands. In real experiments one usually has no precise control of the direction of the electric field. Nevertheless, as Eq. (2.12) shows, only the crossproduct of the field with the momentum contributes to spin-orbit coupling. Therefore, one can assume $\boldsymbol{E} \simeq E_\perp \hat{e}_y$. Finally, the magnetic field can be assumed to be applied in z-direction. As one will see later on, the precise axes of the spin-orbit and magnetic field are of no importance as long as they are perpendicular to each other, [Alicea, 2012]. With the above assumptions Eq. (2.12) is reduced to

$$H_0 = \frac{k_x^2}{2m} - \mu + \tilde{\alpha} k_x \sigma_y + \tilde{B} \sigma_z, \tag{2.18}$$

where $\tilde{\alpha} = \alpha E_\perp$ is the strength of the spin-orbit field and $\tilde{B} = \frac{1}{2} g \mu_B B$ is the Zeeman field. By diagonalising Eq. (2.18), one can already see how an effective spinless regime emerges. Thus, one can switch off the superconductivity, i.e. $\Delta = 0$, in which case Eq. (2.18) essentially describes the total system. The energy eigenvalues for $\Delta = 0$ are given by

$$E_\pm(k_x) = \frac{k_x^2}{2m} - \mu \pm \sqrt{(\tilde{\alpha} k_x)^2 + \tilde{B}^2} \tag{2.19}$$

Starting by applying no magnetic field, i.e. $\tilde{B} = 0$, spin-orbit coupling shifts the two bands according to their spin, see Fig. 2.3 a). A small Zeeman field $\tilde{B} \neq 0$ will then lift the crossing at $k_x = 0$ leading to a gap between the upper and lower band, see Fig. 2.3 b). Inside the gap there exists only one effective spin direction. Therefore, the spin degree of freedom can be frozen out by placing μ inside the gap, $|\mu| < |\tilde{B}|$. Since the chemical potential usually varies along the wire, it is important to increase the size of the gap. As one can see in Fig. 2.3 c), this can be achieved by a larger Zeeman field.

Switching on the superconducting pairing, i.e. $\Delta > 0$, leads to a doubling of the number of bands due to electron-hole symmetry, see Fig. 2.3 d). For simplicity, one can assume the

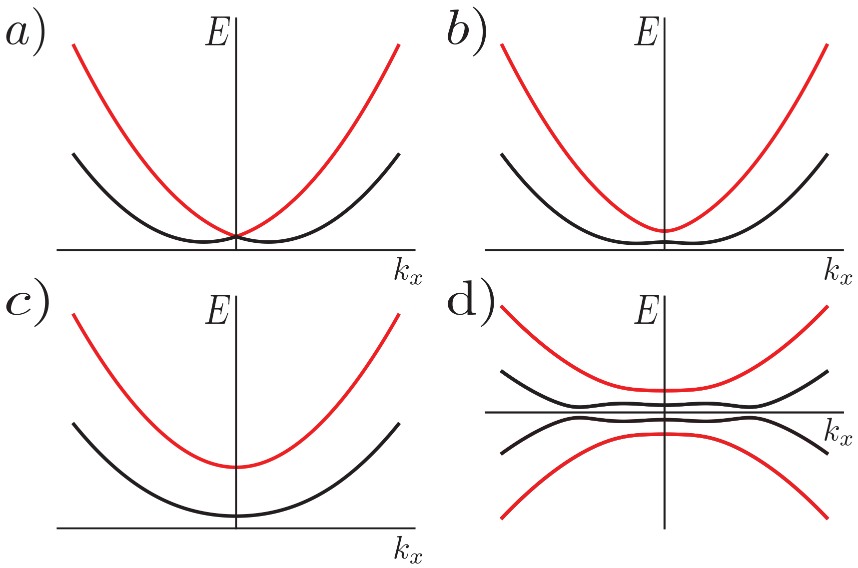

Figure 2.3: Eigenenergies of the proximitised nanowire. $E_+(k_x)$ in Eq. (2.19) is plotted in red. $E_-(k_x)$ is plotted in black. a) $\Delta = \tilde{B} = 0$. Spin-orbit coupling separates the bands according to their spin. b) $\Delta = 0$ and $\tilde{B} > 0$. The Zeeman field opens up a gap at $k_x = 0$. c) $\Delta = 0$ and a larger $\tilde{B}$ as in b). The gap increases with increasing Zeeman field. d) $\Delta \neq 0$. Proximity-induced superconductivity doubles the number of bands. Loosely based on [Leijnse, 2012].

proximity-induced superconductivity to arise from pairing electrons, which are at the exact same location. This implies that $\Delta(x, x') = \Delta\delta(x - x')$. With all the above assumptions solving the Bogoliubov de Gennes equations is equivalent to the diagonalisation of the following Hamiltonian

$$\mathcal{H}_{\text{BdG}} = \begin{pmatrix} \frac{k_x^2}{2m} - \mu + \tilde{B} & -i\tilde{\alpha}k_x & \Delta & 0 \\ i\tilde{\alpha}k_x & \frac{k_x^2}{2m} - \mu - \tilde{B} & 0 & \Delta \\ \Delta & 0 & -\frac{k_x^2}{2m} + \mu + \tilde{B} & i\tilde{\alpha}k_x \\ 0 & \Delta & -i\tilde{\alpha}k_x & -\frac{k_x^2}{2m} + \mu - \tilde{B} \end{pmatrix} \tag{2.20}$$

In order to derive a criterion for topological superconductivity it is sufficient to look at the gap at $k_x = 0$. Here the eigenenergies are given by

$$E_i(k_x = 0) = \pm\sqrt{\tilde{B}^2 + \mu^2 + \Delta^2 \pm 2\sqrt{\tilde{B}^2\left(\mu^2 + \Delta^2\right)}} \tag{2.21}$$

Focussing on the positive solution and placing the chemical potential inside the spinless regime, $|\mu| < |\tilde{B}|$, one finds

$$E_-(0) = \tilde{B} - \sqrt{\mu^2 + \Delta^2} \tag{2.22}$$

Thus, the gap closes at $\tilde{B} = \sqrt{\mu^2 + \Delta^2}$. Note that a very large superconducting pairing Δ results in a topologically trivial phase. One can formulate the criterion for p-wave superconductivity in the nanowire geometry as

$$|\tilde{B}| > \sqrt{\Delta^2 + \mu^2}. \tag{2.23}$$

So far, this criterion only distinguishes between s- and p-wave superconductivity. The phase transition between the topological and topologically trivial superconducting states can only occur by closing the gap, [Leijnse, 2012]. This one can use to indeed link the above criterion to the emergence of Majorana modes. As discussed in [Alicea, 2011], one can choose the above Hamiltonian parameters to further simplify the model, but still fulfil Eq. (2.23). Thus, it is guaranteed for the system to be inside the p-wave phase. The specific limit is given by $\tilde{B} \gg E_{\text{so}}, \Delta$ and $\mu = 0$, where $E_{\text{so}} = m\tilde{\alpha}^2/2$ is the spin-orbit energy. In this case the spins nearly polarise and $\mathcal{H}_{\text{1D}}$ can be projected onto a simpler one-band problem, [Alicea, 2011]. The obtained effective Hamiltonian is given by

$$\mathcal{H}_{eff} = \int dx \left[\Psi_-^\dagger(x) \left(\frac{k_x^2}{2m} - \frac{1}{2}\tilde{B} \right) \Psi_-(x) + i\frac{\tilde{\alpha}}{\tilde{B}}\Delta\Psi_-(x)k_x\Psi_-(x) + \text{h.c.} \right], \tag{2.24}$$

where $\Psi_-^\dagger(x)$ describes the creation operator for electrons in the lower band of the wire. Here the effective strength of the superconducting pairing was reduced by a factor $\tilde{\alpha}/\tilde{B}$. Eq. (2.24) is equivalent to the continuum version of the Kitaev chain Hamiltonian, cf. Eq. (2.8). Therefore, the obtained phase will host Majorana modes and the above criterion is suited for topological superconductivity.

As discussed in Sec. 2.1.2, MZMs emerge at the boundary between topological and topologically trivial phases. In the Kitaev chain the trivial state was given by the vacuum. With the ability to tune the chemical potential, one can create regions of topological and non-topological superconductivity inside the wire. As indicated in Fig. 2.2 b), this can lead to the emergence of more than two MZMs in a single wire - provided that the length of the topological region is much larger than the Majorana coherence length.

Following the discussion in [Leijnse, 2012], a summary of the constituents in the here discussed system hints at possible materials to exhibit topological superconductivity. As Eq. (2.23) suggests and due to deviations of the chemical potential along the wire, the Zeeman field $\tilde{B}$ has to be large. Additionally, the applied magnetic field B should not destroy superconductivity, which results in materials with a large g-factor. Furthermore the spin-orbit coupling $\tilde{\alpha}$ should be large, because the Zeeman field would otherwise suppress the pairing mechanism, see Eq. (2.24). Thus, one requires strong spin-orbit coupling and a large g-factor. Suitable candidates are InAs and InSb, [Lutchyn, 2018].

2.2 Majorana charging island

In this subsection *Majorana charging islands*, also called *Majorana boxes*, are introduced. These mesoscopic structures are supposed to host a set of MBSs, where in addition to the ingredients discussed in Sec. 2.1.3 charging energy works as a protection mechanism. Therefore, in Sec. 2.2.1 these boxes are first introduced by their charge-conserving properties and consequences of those. One of the latter is how MZMs can be addressed by tunneling events. In Sec. 2.2.2 the charge conservation will be used to drastically simplify the representation of Majoranas in terms of Pauli operators. Thereby, the connection between a set of Majorana modes and a spin-1/2 particle will be established.

Most of the content in this subsection was first studied in [Fu, 2010], [Zazunov, 2011] and [Hützen, 2012].

2.2.1 Majorana box and charge conservation

In general, a Majorana box or Majorana charging island is given by a set of parallel 1D nanowires, as discussed in Sec. 2.1.3, which are all proximitised by the same s-wave superconductor. Consequently, all the nanowires essentially share the same electrons.

Assuming that the Majorana coherence length is much longer than the wire length, and neglecting all excitations above the superconducting gap, a Majorana box can be characterised by a set of charge-neutral Majoranas γ_j with $j = 1, \ldots, M$ and two bosonic variables N and φ. Here, N denotes the total number of charges on the box and φ is half the superconducting phase ϕ, i.e. $\varphi = \frac{\phi}{2}$. If the island is now connected to ground via a capacitor, i.e. the island is not grounded but floating, it undergoes charge conservation. This situation is depicted in Fig. 2.4, which is essentially the top view of the 1D nanowire proposal in Sec. 2.1.3. Due to a finite charging energy, the charge conservation leads to N and φ becoming well-defined quantum numbers. This charge quantisation is thereby described by the promotion of the two variables to operators obeying

$$\left[\hat{\varphi}, \hat{N}\right] = i, \qquad e^{i\hat{\varphi}}|N\rangle = |N+1\rangle. \tag{2.25}$$

As Eq. (2.25) indicates, the operator $e^{\pm i\hat{\varphi}}$ creates/annihilates one charge or alternatively half a Cooper pair. The difference between the operator $\hat{\varphi}$, $\hat{N}$ and its eigenvalue φ, N is explicitly shown in this subsection.

One may revisit the Kitaev chain in Sec. 2.1.2 in order to discuss the charge operators described above. The decomposition of electrons into MFs $c_k \sim e^{-i\varphi}\left(\gamma_{k,2} + i\gamma_{k,1}\right)$, cf. Eq. (2.6), included an exponential prefactor. In the case of charge conservation this exponential becomes $e^{-i\hat{\varphi}}$ guaranteeing that - even after one changed to the charge-neutral Majorana representation - the Hamiltonian in Eq. (2.8) remains charge-conserving. Another example for such charge operators is the pairing term in the Kitaev Hamiltonian, i.e. $\Delta e^{i\phi} c_k c_{k+1}$. For a charge-conserving system, $e^{i\hat{\phi}} = e^{2i\hat{\varphi}}$ accounts for the creation of two charges, because the respective term also annihilates two fermions. This pairing of two electrons corresponds to the formation of a Cooper pair. Thus, this reflects the ability of a BCS superconductor to exchange electron pairs (of charge two) between its bosonic Cooper pair condensate and the fermionic sector, [Bruus, 2016].

The Hamiltonian describing this charging effect is given by

$$\mathcal{H}_{\text{Box}} = E_C\left(\hat{N} - n_g\right)^2, \qquad E_C = \frac{e^2}{2C}. \tag{2.26}$$

The single-electron charging energy is given by E_C, reflecting that $\hat{N}$ indeed counts the number of charges in units of electron charge e. Furthermore, the charging energy is inversely proportional to the capacitance C of the island, [Fu, 2010]. Finally, $n_g \sim V_g$ is the backgate parameter, which defines the equilibrium charge of the floating box $\langle\hat{N}\rangle = n_g$. Thus, one can apply a gate voltage V_g (see Fig. 2.4) to pin the total charge of the island to a certain value. If n_g is close to an integer, the charging Hamiltonian implies that $N = n_g$ corresponds to the ground state and neighbouring charge states cost energy of order E_C. This is called *Coulomb valley condition.* The opposite situation is given if n_g is close to half-integer, where the charge of the box will oscillate between two values. This condition is usually referred to as Coulomb peak condition. Whereas the latter also leads to interesting effects, see for example [Herviou, 2016, Michaeli, 2017], the focus of this thesis lies on charge conservation due to Coulomb valley conditions.

So far, there are two relevant energy scales for the Majorana box. The first one is given by the topological gap Δ_{TS}, which is essentially the proximity gap reduced by the applied Zeeman field, cf. Sec. 2.1.3. The second one is given by the charging energy E_C. The capacitance of the island increases with its size. Therefore one usually works in the limit of $E_C < \Delta_{\text{TS}}$. Nevertheless, in the following none of the two energies should be reached.

As the Majorana box has both a bosonic and fermionic sector, corresponding to the

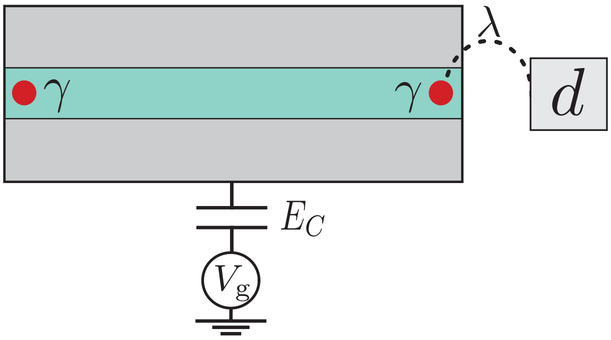

Figure 2.4: Schematic sketch showing a Majorana charging island with two MZMs (red dots). The box - composed of a 1D nanowire and an s-wave superconductor - is connected to ground via a capacitor leading to charge conservation on the island. Additionally, a quantum dot (blue) is coupled to the island. Since the box is operated such that no other fermionic excitations are available (see main text), the quantum dot can address the Majorana mode as indicated by the dashed line. λ is the corresponding complex tunnel-matrix element.

Cooper pair condensate and the Majorana modes respectively, there are also two different ways of accessing the island. The first is given by coupling it to a bulk superconductor with phase φ_0, which results in a Josephson coupling captured by

$$\mathcal{H}_{\mathrm{J}} = -E_J \cos\left(\hat{\varphi} - \varphi_0\right). \tag{2.27}$$

Here, E_J denotes the Josephson coupling between the mesoscopic island and the bulk superconductor. Since the latter is assumed to be large (compared to the Majorana box), charging effects are negligible and φ_0 is not an operator. Such a coupling is able to destroy the topological superconductivity on the island due to a field pinning $\varphi \simeq \varphi_0$ for $E_J \gg E_C$, cf. Eq. (2.27). In this case the mesoscopic island will end up in the topologically trivial superconducting phase, [Hyart, 2013].

The second and more interesting way of addressing the Majorana box is given by coupling to the Majorana modes. On the contrary to the charge $2e$ transport discussed above, coupling to the fermionic sector implies charge e transport. In Fig. 2.4 the Majorana box is addressed by tunneling from/into a quantum dot, as single-level quantum dots are used to probe Majorana excitations in transport experiments, [Albrecht, 2016, Deng, 2016] and [Deng, 2018]. Following the discussion in [Zazunov, 2011, Hützen, 2012], one can model the tunneling between a quantum dot or lead and a Majorana by

$$\mathcal{H}_{\mathrm{t}} = \lambda e^{i\hat{\varphi}} \gamma d + \mathrm{h.c.} = \lambda\left(e^{2i\hat{\varphi}} f + f^{\dagger}\right) d + \mathrm{h.c.}. \tag{2.28}$$

Here, λ is a complex tunnel-matrix element between the MZM (with operator γ) and the fermionic state of the lead or quantum dot (with annihilation operator d). In the case of a quantum dot, d corresponds to the annihilation of a certain mode. Whereas for a lead one assumes point-like tunneling, such that the annihilation operator is given by $d = \psi(0)$ with $\psi(x)$ being the lead-fermion operator. If Δ_{TS} is indeed the largest energy in the system and especially $\lambda \ll \Delta_{\mathrm{TS}}$, there are no other excitations available on the box and Eq. (2.28) captures all possible tunneling processes within the fermionic sector.

As discussed in [Fu, 2010] and [Zazunov, 2011], one way of understanding transport through a Majorana mode is given by writing the corresponding operator in terms of Dirac fermions f, i.e. $\gamma = e^{i\hat{\varphi}} f + e^{-i\hat{\varphi}} f^{\dagger}$, cf. Eq. (2.7). Thus, coupling to a Majorana

mode includes two different types of transport, see Eq. (2.28). The first one is given by annihilating a dot/lead electron and creating an electron on the island ($\sim f^\dagger d$). The second one is given by annihilating a dot/lead electron in combination with the annihilation of an electron on the island to form a Cooper pair ($\sim e^{2i\hat{\varphi}} f d$). Therefore, transport through a Majorana mode can be understood as an equal superposition of in- and out-tunneling due to a conventional fermionic state, where one of the two processes has to involve splitting/creating a Cooper pair.
As a topological superconductor with conserved charge has been introduced here, one can now look at the implications of fixed charge onto the Majorana sector. Thereby, the relevance of a floating (not grounded) topological superconductor is discussed.

2.2.2 Qubit encoding with Majorana fermions

In Sec. 2.1.2 and Sec. 2.1.3 one constantly changes between the Majorana representation and the Dirac fermion representation. Therefore, a system described by $2N$ MFs can be rewritten in terms of N complex fermions. As the Jordan-Wigner transformation allows for the mapping of complex fermions to Pauli operators [Altland, 2010], one can also rewrite Majorana operators by Pauli operators. Thus, one can form a *Majorana spin* or *Majorana qubit.* While it is always possible to change the representation, charge conservation will provide a nice working ground for the spin language.
As introduced in Sec. 2.1.2, Majorana operators γ_i obey the Clifford algebra. Comparing it to the algebra of Pauli operators $\sigma_{n,j}$, i.e.

$$\{\sigma_{m,i}, \sigma_{n,j}\} = 2\delta_{ij}\delta_{mn} I_2, \qquad \{\gamma_i, \gamma_j\} = 2\delta_{ij} I_2, \tag{2.29}$$

one observes that, in order to replace Majorana operators by Pauli operators, one has to manually implement the commutation of Pauli operators of different qubits ($m \neq n$). This can be achieved by the following mapping:
Majorana operators obey anti-commutation rules and square to one, $\gamma^2 = 1$, so do Pauli operators. Therefore, one may start with

$$\gamma_1 = \sigma_{1,x} \quad \text{and} \quad \gamma_2 = \sigma_{1,y}. \tag{2.30}$$

Because any additional Majorana operator has to anti-commute with γ_1 and γ_2, they have to be proportional to $\sigma_{1,z}$. This implies the following structure:

$$\gamma_3 = \sigma_{2,x}\sigma_{1,z}, \qquad \gamma_4 = \sigma_{2,y}\sigma_{1,z}. \tag{2.31}$$

Apparently, the above definitions lead to γ_j obeying the Clifford algebra and they still square to one. For the majority of this thesis, the above spin representation is sufficient, but one can use this iterative structure to formulate a general representation of $2N$ MFs in terms of Pauli operators corresponding to N spin-1/2s or qubits. This general representation is given by

$$\gamma_{2i-1} = \sigma_{i,x} \prod_{n<i} \sigma_{n,z}, \qquad \gamma_{2i} = \sigma_{i,y} \prod_{n<i} \sigma_{n,z}, \qquad \text{for} \quad i = 1, \ldots, N. \tag{2.32}$$

Even though the above transformation looks similar to the Jordan-Wigner transformation it is conceptually simpler, because the Jordan-Wigner string is replaced by the product of Pauli-z operators.
The basis discussed above can always be changed, which corresponds to identifying different spin objects with different MFs. Physically this corresponds to MFs being ideally

zero energy excitations of the same system. As an example, in Sec. 2.1.2 one could have chosen $\gamma_{1,1}$ as the real and not the imaginary part of the zero energy excitation f. In general the decomposition of Majorana operators in Pauli matrices leads to highly non-local objects, which is observed in Eq. (2.30) and Eq. (2.31), where two spins are spread over four MZMs.

Whereas the above representation is very general, one can use a conserved quantity to simplify it. In Sec. 2.1.2 the Majorana parity $i\gamma_{2i}\gamma_{2i-1} = 1 - 2c_i^\dagger c_i$ was introduced. Since this quantity corresponds to the occupation of an auxiliary complex fermionic mode, in a parity-conserving system it is essentially a fixed number - either plus or minus. Therefore, one can define the fermion parity of the Majorana subsector (spanned by $2N$ MFs) as

$$\mathcal{P}_{\mathrm{N}} = \prod_{j=1}^{N} \left(i\gamma_{2j}\gamma_{2j-1}\right) = \prod_{j=1}^{N} \sigma_{j,z} \tag{2.33}$$

Since the parity operator $\mathcal{P}_{\mathrm{N}}$ is the product of Majorana parities its eigenvalues are $\mathcal{P}_{\mathrm{N}} = \pm 1$. A system conserves fermion parity if its Hamiltonian commutes with $\mathcal{P}_{\mathrm{N}}$. Looking at the Kitaev Hamiltonian in Majorana representation, cf. Eq. (2.8), one observes that the Kitaev chain indeed conserved fermion parity. Therefore, the Hamiltonian is quadratic in Majorana operators leading to the promised simplification, because the products of Pauli-z operators in Eq. (2.32) square to unity after inserting them. However, in general such a system does not conserve the fermion number, because the BCS superconductor spontaneously emits and absorbs two electronic excitations, see Sec. 2.2.1. Thus, conservation of the fermion number outplays parity conservation.
The fermion parity in the Kitaev chain or in the topological superconductor - discussed in Sec. 2.1.3 - is no longer conserved if the system is not isolated. Tunneling events do not commute with $\mathcal{P}_{\mathrm{N}}$ as Eq. (2.28) reflects. So, in order to effectively use the above representation in terms of transport, one has to restore parity conservation. This can be achieved by a large charging energy E_C on the topologically superconducting island, see Sec. 2.2.1. Here, charging energy dictates tunneling events to always come in pairs, which results in *cotunneling*. This aspect will be intensively discussed in Sec. 2.3 and Chapter 3. Therefore, the fermion parity conservation can be restored and the above simplification used.

In the following, the two examples in Fig. 2.5 will be discussed, since both will be used continuously throughout the thesis. Starting with the case shown in Fig. 2.5 a), where two 1D nanowires are proximitised by the same s-wave superconductor, giving rise to four MZMs with operators $\gamma_{1,2,3,4}$. One can assume odd fermion parity, which corresponds to $\mathcal{P}_2 = i\gamma_2\gamma_1 i\gamma_4\gamma_3 = -1$. By using Eq. (2.30) and Eq. (2.31), one identifies $\sigma_{1,z} = i\gamma_2\gamma_1$ and $\sigma_{2,z} = i\gamma_4\gamma_3$. Therefore, the parity constraint implies $\sigma_{1,z} = -\sigma_{2,z}$. As this already indicates, the fermion parity constraint reduces the two Pauli-sets to a single new set of Pauli operators. The new Pauli operators are then given by

$$X := \sigma_{1,x}\sigma_{2,x} = -\sigma_{1,y}\sigma_{1,y}, \qquad Y := \sigma_{1,x}\sigma_{2,y} = \sigma_{1,y}\sigma_{2,x}, \qquad Z := \sigma_{1,z} = -\sigma_{2,z} \tag{2.34}$$

Furthermore, these new Pauli operators can be written in terms of Majorana bilinears, where the parity constraint implies two different Majorana combinations for each respective Pauli operator.

$$X = i\gamma_3\gamma_2 = i\gamma_4\gamma_1, \qquad Y = i\gamma_1\gamma_3 = i\gamma_4\gamma_2, \qquad Z = i\gamma_2\gamma_1 = i\gamma_4\gamma_3 \tag{2.35}$$

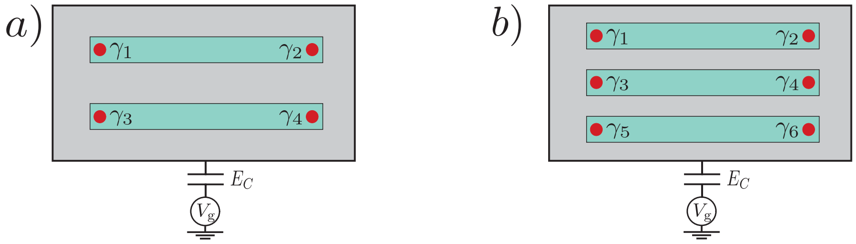

Figure 2.5: Schematic sketch showing two different Majorana charging islands. a) A s-wave superconductor proximitises two parallel 1D nanowires hosting four MZMs represented by $\gamma_{1,2,3,4}$ (red dots). b) Three parallel 1D wires are shunted by a superconductor. Therefore, the island is assumed to host six Majorana modes. The systems correspond to the tetron and hexon device discussed in [Karzig, 2017].

One can understand this effective reduction by looking at the corresponding Hilbert space and its dimension. Without the parity constraint, four Majorana operators or equivalently two qubits have a Hilbert space of dimension 4. The basis states can be chosen to be $|00\rangle$, $|01\rangle$, $|10\rangle$ and $|11\rangle$, which are defined by $\sigma_{1,z}\sigma_{2,z}|00/11\rangle = |00/11\rangle$ and $\sigma_{1,z}\sigma_{2,z}|01/10\rangle = -|01/10\rangle$. This reflects the eigenvalue of $\sigma_{1,z}\sigma_{2,z}$ being the joint-parity of the two qubits. $\mathcal{P}_2 = -1$ confines the system to the odd-parity subspace spanned by $|01\rangle$ and $|10\rangle$. Therefore, the eigenstates of the qubit, which is encoded in four Majorana operators with a parity constraint, is given by $|0\rangle = |01\rangle$ and $|1\rangle = |10\rangle$.

For the example in Fig. 2.5 b) the parity constraint is a bit different. Here, the fermion parity operator is given by an odd number of Majorana parities. Again, one can assume odd parity, i.e. $\mathcal{P}_3 = i\gamma_2\gamma_1 i\gamma_4\gamma_3 i\gamma_6\gamma_5 = -1$. As this parity constraint can be understood as $\sigma_{1,z}\sigma_{2,z}\sigma_{3,z} = -1$, one way of reducing the set of Pauli operators is given by distributing the 'inner' spin $\sigma_{2,z}$ over the outer spins $\sigma_{1,z}$ and $\sigma_{3,z}$. In this irreducible representation one can identify the new set of Pauli operators with

$$\begin{aligned} X_1 &:= \sigma_{1,x}\sigma_{2,x}, \qquad & Y_1 &:= \sigma_{1,y}\sigma_{2,x}, \qquad & Z_1 &:= \sigma_{1,z} \\ X_2 &:= \sigma_{3,x}\sigma_{2,x}, \qquad & Y_2 &:= \sigma_{3,y}\sigma_{2,x}, \qquad & Z_2 &:= \sigma_{3,z}. \end{aligned} \tag{2.36}$$

In the Majorana representation the Pauli operators corresponding to the two qubits, which define the low-energy sector of the hexon shown in Fig. 2.5, are given by

$$\begin{aligned} X_1 &= i\gamma_3\gamma_2, \qquad & Y_1 &= i\gamma_1\gamma_3, \qquad & Z_1 &= i\gamma_2\gamma_1 \\ X_2 &= i\gamma_5\gamma_4, \qquad & Y_2 &= i\gamma_6\gamma_4, \qquad & Z_2 &= i\gamma_6\gamma_5. \end{aligned} \tag{2.37}$$

For six Majorana operators the parity constraint does not only simplify the representation in terms of Pauli operators. Furthermore it allows the device in Fig. 2.5 b) to address products of Pauli operators in a very elegant way. Due to $\mathcal{P}_3 = -1$, the joint-parity operator Z_1Z_2 can be written in terms of a single Majorana bilinear, i.e. $Z_1Z_2 = i\gamma_3\gamma_4$. Thus, for the here shown device the implementation of single Pauli operations is of the same difficulty as for products of Paulis, [Karzig, 2017]. This reflects one of the key advantages of transport through Majorana modes, which will be highlighted throughout this thesis.

2.3 Quantum transport through a single Majorana box

Having introduced a charge-conserving, topologically superconducting island, dubbed Majorana box, and a way to address its fermionic sector, the next step is to discuss quantum transport in such boxes. In Sec. 2.3.1, the general setup is discussed. Here, the concept of a simple Majorana-lead junction is introduced, since this concept will be generalised in Chapter 3. As already mentioned in Sec. 2.2.2, the large charging energy of the island can result in cotunneling events. Sec. 2.3.2 is therefore dedicated to the derivation of a cotunneling Hamiltonian, for which the system introduced in Sec. 2.3.1 serves as an example. Afterwards, Sec. 2.3.3 gives a compact overview of renormalisation-group theory as it is often used to access the low-energy physics of coupled systems. Finally, in Sec. 2.3.4 the Majorana box coupled to a set of N leads is discussed at strong coupling. Here, the topological Kondo effect will emerge.

Quantum transport in a single Majorana box hosting at least four Majorana modes was first discussed in [Béri, 2012, Altland, 2013]. The work in [Zazunov, 2014] can be viewed as a more detailed reference for this section. Most of the techniques used here are discussed in the books by Gogolin, *et al.* [Gogolin, 2004], Altland and Simons [Altland, 2010] and Bruus and Flensberg [Bruus, 2016].

2.3.1 Setup and simple Majorana-lead junctions

The mesoscopic system of interest is given by a single Majorana box coupled to M non-interacting leads, see Fig. 2.6 a). Since each lead is assumed to couple to a different single MZM, the island has to host at least M MFs. Following the discussion in Sec. 2.1.3 N parallel 1D strong spin-orbit nanowires, which are proximitised by the same s-wave superconductor, give rise to $2N$ MZMs as long as the nanowire length is much larger than the Majorana coherence length. In general the number of MFs on the island has to obey $2N \geq M$.

The Majorana modes are assumed to have zero energy. Moreover the topological gap Δ_{TS} is sufficiently large to neglect unwanted quasiparticle excitations. Therefore, the Majorana box is well described by a charging Hamiltonian, cf. Eq. (2.26), with charging energy E_C and charge operator N.

The leads can be realised by using the same nanowires as for the topological superconductors, but not inducing superconductivity, see Fig. 2.6 a). In this case due to spin-orbit coupling and the applied Zeeman field, the leads can be modelled as non-interacting and effectively spinless. Since the leads are used to address the Majorana modes on the island, which lie at zero energy, it is sufficient to look at low energy scales. Therefore, the lead Hamiltonian can be obtained by linearising the Hamiltonian of non-interacting spinless electrons around the Fermi energy E_F, which is defined to be zero. Choosing the contact between leads and Majorana box to be at $x = 0$, the lead Hamiltonian is described by left- and right-moving fermions for $x > 0$:

$$\mathcal{H}_{\text{leads}} = -iv_F \sum_{j=1}^{M} \int_0^\infty dx \left(\psi^\dagger_{j,R} \partial_x \psi_{j,R} - \psi^\dagger_{j,L} \partial_x \psi_{j,L} \right). \tag{2.38}$$

Here, $\psi_{j,R/L}(x)$ is an 1D spinless fermion operator obeying the open boundary condition $\psi_{j,L}(0) = \psi_{j,R}(0)$ and all leads are assumed to have the same Fermi velocity v_F. A very convenient simplification is achieved by unfolding the semi-infinite leads, [Gogolin, 2004]. Thus, one can switch to chiral (right-moving) fermions, $\psi_j(x)$, with $\psi_j(x) = \psi_{j,R}(x)$ for $x > 0$ and $\psi_j(x) = \psi_j(-x)$ for $x < 0$. In this case the lead Hamiltonian reduces to

$$\mathcal{H}_{\text{leads}} = -iv_F \sum_{j=1}^{M} \int_{-\infty}^{\infty} dx \ \psi^\dagger_j \partial_x \psi_j. \tag{2.39}$$

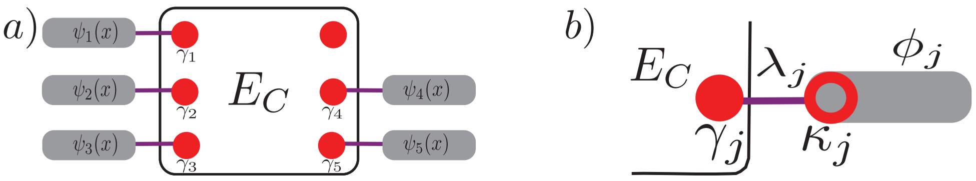

Figure 2.6: a) Schematic sketch of a Majorana box coupled to $M = 5$ leads. The island is assumed to host six MZMs (red dots). The depicted box is essentially the same as in Fig. 2.5 b). For simplicity, the proximitised nanowires are hidden and the island itself is transparent to highlight the most important effects. Metallic leads with fermion operators $\psi_j(x)$, cf. Eq. (2.39), are coupled to Majorana modes, which are labelled by the respective lead. b) The *simple Majorana-lead junction* is shown here [Gau, 2018]. After the bosonisation, lead-charge fluctuations are described by ϕ_j and the Klein factor κ_j (red circle) is coupled to Majorana operator γ_j with tunnel-matrix element λ_j (indicated by the purple link). γ_j and κ_j have a fixed parity leading to the simplification of the tunneling Hamiltonian, see main text.

Having established the two subsystems one can now introduce tunneling between the two. This tunneling will be of the form discussed in Sec. 2.2.1. With the chiral fermion operator at the boundary $\Psi_j := \psi_j(0)$ the tunneling Hamiltonian is given by

$$\mathcal{H}_\mathrm{t} = \lambda_{jk} \Psi_j^\dagger \gamma_k e^{-i\varphi} + \mathrm{h.c.}, \tag{2.40}$$

Here, λ_{jk} denotes the tunnel-matrix element between the MZM with operator γ_k and lead j. As discussed in Sec. 2.2.1, φ is the charge-conjugated operator of the island. The Hamiltonian describing the setup shown in Fig. 2.6 a) is thereby given as $\mathcal{H}_0 = \mathcal{H}_\mathrm{Box} + \mathcal{H}_\mathrm{leads} + \mathcal{H}_\mathrm{t}$.

So far, the Majorana box is described in terms of fermionic (Majoranas) and bosonic operators (charge/phase), whereas the leads are fully characterised by a fermionic description. In [Altland, 2013, Béri, 2013] it was shown that it is beneficial to bosonise the leads such that transport is effectively described by a purely bosonic theory. For this purpose the left- and right-moving fermions are bosonised according to [Gogolin, 2004], cf. Fig. 2.6 b),

$$\psi_{j,R/L}^\dagger(x) = \frac{\kappa_j}{\sqrt{\alpha}} e^{i[\phi_j(x) \pm \theta_j(x)]}, \tag{2.41}$$

where α is a short-distance cutoff. $\phi_j(x)$ and $\theta_j(x)$ are dual boson fields, which obey $[\phi_j(x'), \partial_x \theta_k(x)] = i\pi\delta(x - x')\,\delta_{jk}$, and κ_j is a Klein factor ensuring that different lead fermions still anti-commute. Therefore κ_j can be expressed as a MF, i.e. $\kappa_j^\dagger = \kappa_j$ and $\{\kappa_j, \kappa_k\} = 2\delta_{jk}$. In analogy to the phase operator on the island, $e^{\pm i\phi_j(x)}$ will in- or decrease the number of charges in lead j by one. Since θ_j is the conjugated variable, $\rho_j(x) \sim \partial_x \theta_j(x)$ describes the charge density in lead j up to position x.
The open boundary condition $\psi_{j,L}(0) = \psi_{j,R}(0)$ translates to $\theta_j(0) = 0$ and with the shorthand notation $\Phi_j = \phi_j(0)$ and $\Theta_j' = \partial_x \theta_j(0)$, the lead fermion operator in Eq. (2.40) takes the form

$$\Psi_j^\dagger = \alpha^{-1/2} \kappa_j e^{i\Phi_j}. \tag{2.42}$$

By inserting Eq. (2.41) one can rewrite the lead Hamiltonian and obtain the 1D Luttinger liquid Hamiltonian for the non-interacting case, see [Gogolin, 2004],

$$\mathcal{H}_\mathrm{leads} = \frac{v_F}{2\pi} \sum_{j=1}^{M} \int_{-\infty}^{0} dx \left[(\partial_x \phi_j)^2 + (\partial_x \theta_j)^2 \right]. \tag{2.43}$$

The lead Hamiltonian is now exclusively described by bosonic operators, because the corresponding Klein factors squared to unity.

For the tunneling Hamiltonian in Eq. (2.40) the situation is a different one. Here, the bosonisation of Eq. (2.41) results in

$$\mathcal{H}_{\mathrm{t}} = \lambda_{jk}\kappa_j\gamma_k e^{i(\Phi_j-\varphi)} + \text{h.c.}, \tag{2.44}$$

where λ_{jk} was renormalised by a factor of $\alpha^{-1/2}$. Now, the tunneling Hamiltonian reflects a separation of charge and fermionic variables. Since the complete system is still defined by $\mathcal{H}_0$, $i\kappa_j\gamma_k = \pm 1$ is a conserved quantity in the system. Thus, as long as each Majorana mode is only coupled to a single lead and each lead is only coupled to a single Majorana, cf. Fig. 2.6 b), one observes M local parity constraints in the system. Therefore, in Eq. (2.44) one can fix the fermion parity and obtain a purely bosonic tunneling Hamiltonian. In [Béri, 2013] the idea of fixing the parity in order to reduce the systems complexity was called *Majorana-Klein fusion.* To establish the connection to Chapter 3 the distinction of different coupling mechanisms - put forward in [Gau, 2018] - will be used here. Thus, tunnel junctions, which can be described by the purely bosonic Hamiltonian

$$\mathcal{H}_{\mathrm{t,simple}} = -i\lambda_{jk} e^{i(\Phi_j-\varphi)} + \text{h.c.} = \lambda_{jk}\sin\left(\Phi_j - \varphi\right), \tag{2.45}$$

are called *simple Majorana-lead junctions.* As Eq. (2.45) does not contain any information on the Majorana mode, which was addressed, the second index in the tunneling-matrix element is suppressed throughout this section. In the following we therefore denote the tunneling-matrix element only with respect to the lead, i.e. $\lambda_j \coloneqq \lambda_{jk}$.

2.3.2 Cotunneling Hamiltonian

Without the Majorana-lead coupling, the island is in its charge ground state with $\langle N\rangle = n_g$ defined by the backgate voltage. Since the island is operated under Coulomb valley conditions, where n_g is close to an integer, the charge is indeed conserved and accessing the nearest neighbouring charge states costs energy of order E_C. Thereby, a weak Majorana-lead coupling $\lambda_{jk} \ll E_C, \Delta_{\mathrm{TS}}$ will introduce virtual transitions between neighbouring charge states. This can be seen by considering $\mathcal{H}_{\mathrm{Box}}$ and $\mathcal{H}_{\mathrm{t,simple}}$ in terms of perturbation theory in the coupling λ_{jk}. In literature, this is often referred to as *Schrieffer-Wolff transformation.*

In general, a second-order Schrieffer-Wolff transformation with respect to a Hamiltonian H_0 with eigenstates $|\alpha\rangle$ and perturbation H_1 is given by

$$H_{\mathrm{eff}} = \sum_{\alpha} E_\alpha |\alpha\rangle\langle\alpha| + \sum_{\alpha,\alpha'} |\alpha\rangle\langle\alpha'| \sum_{\beta}\left(\frac{1}{E_\alpha - E_\beta} + \frac{1}{E_{\alpha'} - E_\beta}\right)\langle\alpha|H_1|\beta\rangle\langle\beta|H_1|\alpha'\rangle. \tag{2.46}$$

Here, $|\beta\rangle$ denotes the energetically neighbouring states to $|\alpha\rangle$ and E_j is the eigenenergy of state $|j\rangle$. Eq. (2.46) reflects that the Schrieffer-Wolff transformation is a projection of the system onto the ground states of H_0, where virtual excursions are penalised by the energy difference to the ground-state energy. This also defines a time scale of the obtained theory, since virtual excursions require time $\sim 1/\left(E_\alpha - E_\beta\right)$. Note that for the purpose of not mixing notations the general Hamiltonians here are not written in calligraphic letters.

In the case of the Majorana box, H_0 is given by $\mathcal{H}_{\mathrm{Box}}$ and the perturbation is the tunneling Hamiltonian $\mathcal{H}_{\mathrm{t,simple}}$. Moreover, the charge ground state is given by $|N\rangle$ and the energetically closest charge states are $|N \pm 1\rangle$. Due to the charge constraint on the box, the phase exponential operators $e^{\pm i\varphi}$ have to cancel out resulting in the effective second-order Hamiltonian

$$\mathcal{H}_{\text{eff}} = -\frac{1}{U_+}\sum_{j,k}\lambda_j\lambda_k e^{i(\Phi_j-\Phi_k)} - \frac{1}{U_-}\sum_{j,k}\lambda_j\lambda_k e^{-i(\Phi_j-\Phi_k)}, \tag{2.47}$$

where $U_\pm = \mathcal{H}_{\text{Box}}(N \pm 1) - \mathcal{H}_{\text{Box}}(N)$. The energy difference between neighbouring charge states is of the order E_C, cf. Sec. 2.2.1. Therefore, one can simplify the above effective Hamiltonian as

$$\mathcal{H}_{\text{eff}} = -\sum_{j,k} J_{jk}\cos(\Phi_j - \Phi_k)\,. \tag{2.48}$$

This Hamiltonian describes charge transport from lead k via the island into lead j. Thus, the charge state of the island does not change on time scales larger than $1/E_C$ and, as Eq. (2.47) reflects, this transport has two different realisations. The first is given by an electron tunneling from lead k onto the island and, as the charge state of the island is increased, it is immediately reduced by an out-tunneling event to lead j. The second realisation consist of first reducing the charge state on the box and thus, tunneling into lead j. Afterwards, the charge on the island is restored by an in-tunneling event from lead k. This corresponds to the access of both nearest neighbouring charge states, i.e. $|N \pm 1\rangle$. This cotunneling nature is included in the definition of the cotunneling energy $J_{jk} \simeq \frac{\lambda_j\lambda_k}{E_C}$. Note that $\mathcal{H}_{\text{eff}}$ in principle contains an energy off-set due to the projection, cf. Eq. (2.46). Nevertheless, this irrelevant renormalisation energy was dropped.

Finally, the low-energy Hamiltonian of the Majorana box coupled to M leads is given by the effective Hamiltonian

$$\mathcal{H}_{\text{weak}} = \mathcal{H}_{\text{leads}} + \mathcal{H}_{eff} = \mathcal{H}_{\text{leads}} - \sum_{j,k=1}^{M} J_{jk}\cos(\Phi_j - \Phi_k)\,. \tag{2.49}$$

The effective Hamiltonian in Eq. (2.48) is derived in the case of weak lead-island coupling. In this limit tunneling only weakly effects the states of the leads and box, which are well described by distribution functions due to temperature or applied voltages, [Bruus, 2016]. Therefore, the cotunneling Hamiltonian corresponds to the *weak-coupling regime*. At very low energies, however, the correlations between leads and box, which are induced by tunneling, become more dominant. Consequently, one is usually interested in the opposite regime of *strong-coupling*. Here, the dominant degrees of freedom are typically fewer than in the weak-coupling regime. Thus, the main challenge of a weak-coupling theory is to identify the relevant mechanisms, which will survive in the limit of very low energies.

2.3.3 Renormalisation-group theory

In Sec. 2.3.2 the system was simplified by discarding charge fluctuations on the island. In the same way, this section is dedicated to the low-energy sector of the leads. Unfortunately, the leads are given by normal conductors (metals). Therefore, there density of states is assumed to be almost constant over a large energy range [Bruus, 2016]. This makes it impossible to distinguish the low- from the high-energy sector, since there is no separation by a gap. Thus, the conventional perturbative approach, see Sec. 2.3.2 does not work.

Renormalisation-group theory (RG) is based on variation or *renormalisation* of scales (e.g. energies, fields, space) to identify repeating structures. If, for example, the same effect is observed at large and small scales of a problem, the 'smaller' version of it can be discarded, because it is more likely to be overseen in observables. [Altland, 2010] provides a nice introduction to the field of RG. Since the RG will be used to identify the low-energy

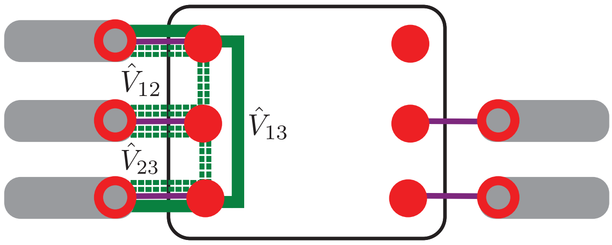

Figure 2.7: Schematic sketch showing one example of an operator-product expansion. Two cotunneling processes $\hat{V}_{12} = e^{i(\Phi_1 - \Phi_2)}$ and $\hat{V}_{23} = e^{i(\Phi_2 - \Phi_3)}$ (green dashed lines) are contracted to generate $\hat{V}_{13}$ (thick green line). Since $\hat{V}_{12}$ describes electron transport from lead 2 to lead 1 and $\hat{V}_{23}$ is the cotunneling even starting in lead 3 and ending in lead 2, the enforced process $\hat{V}_{13}$ reflects charge transport from lead 3 into lead 1.

sector of the leads, the here discussed method is a *time-* or *frequency-shell RG*. Therefore, the renormalised quantity will be an energy.

The starting point of the RG is to define a high-energy cutoff D for the leads. States with energy above this cutoff are considered to belong to the high-energy sector and thus, can be integrated out. In Sec. 2.3.2 charge fluctuations on the island were discarded, which implies that lead states of energy E_C are already overruled. The initial lead bandwidth is given by $D(\ell = 0) < E_C$. Accordingly, the idea is to renormalise this cutoff

$$D(\ell) = D(0)e^{-\ell} \tag{2.50}$$

with renormalisation flow parameter ℓ, and study how the cotunneling amplitudes J_{jk} are effected as only lower and lower lead energies contribute to the system. Conceptually, as the flow parameter increases, the lead bandwidth is decreased and lead-fermion states with energies $\omega > D(\ell)$ are integrated out. Since, with increasing flow, the relevant energies are exponentially reduced, the flow is towards the strong-coupling regime. Due to the derivation of the RG equations in the weak-coupling regime, the perturbation will eventually break down. This implies that the weak-coupling RG - discussed here - can indicate, but not prove, the relevant low-energy physics.

The equations describing the change of physical quantities under renormalisation are called *RG equations*. In this section, the field-theoretical method of operator-product expansion (OPE) in combination with Wicks theorem, cf. [Altland, 2010], is used. Here, this procedure is briefly sketched. In Sec. 2.3.2 the system is described by cotunneling operators $\hat{V}_{jk} := e^{i(\Phi_j - \Phi_k)}$. The OPE contracts two arbitrary cotunneling operators $\hat{V}_{jk}(\tau)$ and $\hat{V}_{j'k'}(\tau')$ acting almost at the same (imaginary) time τ and τ'. The result of this contraction has to be equivalent to another cotunneling process in the system at time $(\tau + \tau')/2$. The expansion coefficients then determine the RG equations. While the field-theoretical background is abstract, the contraction itself can be understood by simple explanations. In Fig. 2.7, the above mentioned contraction is shown. Here, two different cotunneling processes $\hat{V}_{12} = e^{i(\Phi_1 - \Phi_2)}$ and $\hat{V}_{31} = e^{i(\Phi_3 - \Phi_1)}$ are contracted in favour of the third process $\hat{V}_{32}$. Thus, as long as the cotunneling events are purely bosonic, one can understand the OPE as the combination of two cotunneling processes in order to obtain a third process. In Chapter 3, this will slightly change, since a remaining fermionic sector implies certain anti-commutation and commutation constraints, cf. [Gau, 2018].

The obtained RG equations for the system - shown in Fig. 2.7 for $M = 5$ leads - are given by

$$\frac{dJ_{jk}}{d\ell} = \sum_{m\neq j,k} J_{jm}J_{mk}, \tag{2.51}$$

where J_{jk} describes cotunneling between two distinct leads, i.e. $j \neq k$. In comparison to the Schrieffer-Wolff transformation, the two cotunneling processes first excite an intermediate state in lead n, which is immediately deexcited, contributing to the process between leads j and k. Furthermore, Eq. (2.51) implies that all cotunneling amplitudes flow towards strong-coupling and, since they are all enforcing each other, they will flow towards isotropy, $J_{jk}(\ell) \to (1-\delta_{jk})\, J(\ell)$, [Altland, 2013]. The RG equation for the isotropic coupling then reads $dJ/d\ell = (M-2)J^2$. Here, M is the number of attached leads. Note that for $M < 3$ there is no RG equation, because the reinforcing mechanism discussed above cannot work. Here, one obtains either resonant charge transport for Coulomb peak conditions, [Fu, 2010], or a Coulomb-blockaded island for n_g close to an integer, [Hützen, 2012]. Thus, at least three leads are required for the cotunneling processes to enter the strong-coupling theory.

Having the set of RG equations one can define the energy scale, where the perturbation theory applied in the derivation breaks down. Since the starting point of the RG was the cotunneling Hamiltonian in Eq. (2.44), the above RG equations are not valid any longer when the J_{jk} reach order ~ 1. Because RG techniques are often used to discuss spin impurity scattering and because the object on the island is effectively a non-local spin, cf. Sec. 2.2.2, the crossover energy scale is called *Kondo temperature*. In the here discussed system the Kondo temperature is estimated to be [Gau, 2018]

$$T_K \simeq D(0)e^{-1/[(M-2)J]}. \tag{2.52}$$

Thereby ,the strong-coupling regime is well-defined by energies $\omega < T_K$. Moreover, all cotunneling processes will enter the strong-coupling theory with equal strength J. Finally, another feature of the present RG analysis is that it does not generate additional processes, which were absent in the beginning. In Chapter 3 a system is discussed, where additional interference effects create spin-density fluctuations in the leads. Whereas the fluctuations are negligible at weak-coupling, they become more important as the lead bandwidth is decreased. This implies that a RG analysis is capable of highlighting relevant physical processes, even if the model initially did not include those.

2.3.4 Topological Kondo effect

As the weak-coupling RG analysis showed, the different cotunneling amplitudes flow towards isotropy. This defines a *fixed-point* in the weak-coupling RG. The aim of a strong-coupling theory is therefore to test whether the fixed-point is indeed a stable solution of the system. If the fixed-point turns out to be stable, the initially discussed effective system describes the most relevant parts of the low-energy physics. When a fixed-point turns out to be unstable, the effective description either overlooked important effects or the strong-coupling regime is dominated by completely different mechanisms. Luckily, in the case of the system here discussed the obtained fixed-point turns out to be stable.

Considering energy scales below the Kondo temperature T_K, the Hamiltonian $\mathcal{H}_{\text{weak}}$, see Eq. (2.49), is not valid any longer. Therefore, one starts by formulating the strong-coupling Hamiltonian, which corresponds to the fixed-point of the weak-coupling RG. In the case of a single Majorana box coupled to M leads, the Hamiltonian is given by

$$\mathcal{H}_{\text{strong}} = -J \sum_{j \neq k = 1}^{M} \cos\left(\Phi_j - \Phi_k\right). \tag{2.53}$$

In [Yi, 1998, Yi, 2002], an equivalence between multi-channel Kondo problems and quantum brownian motion in periodic potentials was established. The idea is that in the strong-coupling regime $\mathcal{H}_{\text{strong}}$ will effectively pin the lead phase-fields to a certain configuration $\{\Phi_j\}$, which minimises the energy. In this limit of pined phase-field differences multiple configurations minimising the energy exist. Interpreting the variables Φ_j as coordinates of a particle, leads to quantum brownian motion between different configurations that minimise $\mathcal{H}_{\text{strong}}$. This discussion can be used to show that the obtained fixed-point is stable against anisotropies in the cotunneling amplitudes. Note that a perturbation, which breaks the ground-state degeneracy on the box, e.g. a direct coupling of Majorana operators, is relevant and will therefore destroy the here discussed fixed-point.

One way to approach the system at strong coupling is given by a transformation of the lead phase-fields, as was done by Béri in [Béri, 2017]. In [Gau, 2018], it was argued that, due to the field pinning at strong coupling, the phase-differences $\Phi_j - \Phi_k$ are frozen out and the only relevant degree of freedom is given by the center-of-mass phase

$$\phi_0(x) = g_0 \sum_{j=1}^{M} \phi_j(x), \quad g_0 = \frac{1}{\sqrt{M}}, \tag{2.54}$$

where the boundary center-of-mass field is given by $\Phi_0 = \phi_0(x = 0)$. Note that Eq. (2.53) is invariant under a shift of the center-of-mass field, since the fields Φ_j and Φ_k will be shifted by an equal amount. This justifies switching to a new basis, which for the boundary fields reads $\tilde{\Phi}_j := \Phi_j - g_0\Phi_0$ with the constraint $\sum_j \tilde{\Phi}_j = 0$, see [Gau, 2018]. The strong-coupling Hamiltonian is then given by

$$\mathcal{H}_{\text{strong}} = -J \sum_{j \neq k = 1}^{M} \cos(\tilde{\Phi}_j - \tilde{\Phi}_k). \tag{2.55}$$

Interestingly, Eq. (2.55) does not include Φ_0, which implies that Φ_0 can be changed without energy cost. In analogy to [Yi, 1998], this corresponds to free motion of the particle along the Φ_0-direction. Therefore, the center-of-mass field Φ_0 will dominate the low-energy physics of the system.

As the individual lead phase-fields are pinned, charges will heavily fluctuate between the leads. The remaining degree of freedom is then given by Φ_0, which describes collective transport between all M attached leads. This can be visualised by looking at a single process contained in the strong-coupling model, e.g. $e^{i\tilde{\Phi}_j} \sim e^{i(\Phi_j - g_0\Phi_0)}$. As $g_0 = 1/\sqrt{M}$, such a process corresponds to the absorption of a charge in lead j, where the charge was democratically collected from all leads. The physical process corresponding to this observation is the absorption of a Cooper pair in lead j, due to resonant Andreev reflection, and this charge is then democratically distributed over all attached leads. Thus, effectively each lead absorbs charge $2e/M$. Since the conductance is given by the product of the conductance quantum (e/h) and the net transferred charge, one obtains the zero-temperature and zero-bias conductance of the system, [Altland, 2013, Zazunov, 2014],

$$G_{jk} = \frac{2e^2}{h} \left(\delta_{jk} - \frac{1}{M} \right). \tag{2.56}$$

This effect of democratically dividing the charge over the attached leads is called *topological Kondo effect* (TKE). It is not only an effect of strong-correlations, but arises due to the topology of the problem. The non-local spin on the box is key for thos, since it allows for an unique coupling of all attached leads. Therefore, the observation of the TKE is believed to be a clear indicator for the existence of MZMs on the island. In various publications [Béri, 2012, Altland, 2013, Béri, 2013, Zazunov, 2014, Plugge, 2016a, Béri, 2017], corrections to the here discussed fixed-point were discussed. Some of these corrections arise from bias voltage, temperature or interacting leads. Therefore, a single Majorana box is well understood and a large set of predictions exist, which have yet to be verified in experiments.

In [Gau, 2018], the here presented discussion was generalised to a network composed of multiple Majorana boxes. In such networks, Majorana-lead junctions can differ from the simple coupling, and lead to Eq. (2.45), which results in new effects. Nevertheless, the simple Majorana-lead junctions will always be present in networks of Majorana islands, which can result in TKEs on individual boxes inside a larger network. In Chapter 3, the notation of [Gau, 2018] will be used, in which a collection of leads - monogamously coupling to a single Majorana mode - form a bosonic subsector. For very low energies such bosonic subsectors exhibit the TKE.

2.4 Topological quantum computation

In this section the focus will be laid on the importance of MBSs for quantum computation. As discussed in Sec. 2.2.2, one can always define a qubit in terms of MZMs. Because of the nonlocality of the Majoranas, this qubit is topologically protected against local decoherence mechanisms, [Kitaev, 2001]. Thus, the proposal to use Majoranas for quantum information purposes is as old as the first Majorana-related publications in condensed matter physics, see [Beenakker, 2013]. In order to understand Majorana-based qubits and the impact of Chapter 4 in the context of quantum information and quantum computation, this section starts with a short introduction to quantum gates. In Sec. 2.4.2 the *Majorana box qubit* [Plugge, 2017], or alternatively the *tetron* in [Karzig, 2017], is introduced. As this qubit is essentially the already discussed Majorana charging island, the main goal is to establish convenient ways to access the information stored on the island, i.e. the implementation of read-out schemes. Afterwards, Sec. 2.4.3 contains the realisation of quantum gates in the tetron architecture, where the discussion of single-qubit gates are extended to simple two-qubit operations.

The first part of this section is based on the excellent book by Nielsen and Chuang [Nielsen, 2010]. The tetron was introduced in [Plugge, 2017] and [Karzig, 2017]. For a discussion of networks of Majorana qubits, which form e.g. surface or color codes, see [Landau, 2016, Plugge, 2016b, Litinski, 2017].

2.4.1 Quantum gates for universal quantum computation

For quantum computation two main directions exist. The first one is adiabatic quantum computation, where quantum information contained in the Hilbert space of a Hamiltonian $H[\xi(t)]$, which depends on a set of parameters $\xi(t)$, is manipulated by the gradual change of the Hamiltonian parameters. One simple example for adiabatic quantum computation is given by the equivalence of a qubit and a spin-1/2 particle. Supposing that this spin is oriented in a random direction, a strong magnetic field, which is switched on at $t = 0$ will align the spin in its orientation. Thus, the qubit can be initialised in any state by choosing

the direction of the magnetic field. Changing the direction of the magnetic field - corresponding to a change of the parameter set $\xi(t)$ - will drag the spin along, since its energy is minimised when being aligned with the field. Therefore, if the change of parameters is slow enough for the spin to follow its variation, the qubit state will change gradually. This way of performing quantum computation is system-dependent and important aspects are for example the validity of the adiabatic manipulation. In order to guarantee that, one has to compare the manipulation scheme to various competing mechanisms (present in the respective system) leading to dephasing and determine a criterion for adiabaticity. In Chapter 4, the idea of adiabatic quantum computation is briefly discussed for a Majorana system.
The second and here discussed direction for quantum computation is digital, which relies on the circuit model for quantum computation. The idea behind it is that in analogy to classical computations, a fixed set of operations is sufficient for all possible operations. This implies that any quantum computation can be decomposed in elementary quantum operations, which define the *universal* set. Therefore, the main advantage of pursuing this direction is the need for implementing a universal set of quantum gates, which then represent the building block or unit cell of a quantum computer for the studied system. Once the gates are realised quantum error correcting codes can be used for computational purposes. As most of the quantum gates turn out to be implemented in a simple fashion, there exist always at least one operation, which turns out to be very difficult. For Majorana platforms this is the T-gate [Litinski, 2017], which will be discussed later.

Once again, operators are explicitely indicated, e.g. $\hat{Z}$, and there eigenvalues are given by neglecting the 'hat', e.g. Z. Furthermore, the shown matrices are in the basis of $\hat{Z}$-eigenstates, i.e. $|0\rangle$ and $|1\rangle$, where $\hat{Z}\,|0\rangle = |0\rangle$ and $\hat{Z}\,|1\rangle = -\,|1\rangle$. In this basis, a single qubit is given by $|\psi\rangle = a\,|0\rangle + b\,|1\rangle$, which is parameterised by two complex numbers a and b, which have to obey $|a|^2 + |b|^2 = 1$. As the norm reduces the number of degrees of freedom to two, one convenient way to discuss a single qubit is the Bloch representation. Here, the pure state $|\psi\rangle$ is visualised by a point (ϑ, φ) on the surface of the unit sphere [Nielsen, 2010]. In general, mixed states $\rho = \sum_j |\psi_j\rangle\,\langle\psi_j|$ are then given by points inside the unit sphere. During operations, the above norm has to be preserved, which is why single-qubit quantum gates can be described in terms of 2×2 unitary matrices. One might start with the simplest and yet most important single-qubit gates, which are described by Pauli matrices

$$\hat{X} = \begin{pmatrix} 0 & 1 \\ 1 & 0 \end{pmatrix}, \qquad \hat{Y} = \begin{pmatrix} 0 & -i \\ i & 0 \end{pmatrix}, \qquad \hat{Z} = \begin{pmatrix} 1 & 0 \\ 0 & -1 \end{pmatrix}. \tag{2.57}$$

The corresponding eigenstates are then given by $|0/1\rangle$ for $\hat{Z}$, $|\pm\rangle = \frac{1}{\sqrt{2}}\left(|0\rangle \pm |1\rangle\right)$ for $\hat{X}$ (with $X = \pm 1$) and $|\phi^{\pm}\rangle = \frac{1}{\sqrt{2}}\left(|0\rangle \pm i\,|1\rangle\right)$ for $\hat{Y}$ (with $Y = \pm 1$). Because of their action on eigenstates of anti-commuting Paulis, the operations mentioned above are called Pauli flips. If, for example, the qubit is prepared in $|0\rangle$, a Pauli-X flip will lead to $\hat{X}\,|0\rangle = |1\rangle$. In the Bloch representation this operation is thereby given by a π-rotation around the X-axis, resulting in a flip of the state. Analogously $\hat{Z}$ flips $|+\rangle$ to $|-\rangle$.
Observing that a Pauli operation leads to a rotation of the qubit, one can look at a general rotation given by

$$e^{-i\vartheta\hat{Z}} = \cos\vartheta I_2 - i\sin\vartheta\hat{Z} = \begin{pmatrix} e^{-i\vartheta} & 0 \\ 0 & e^{i\vartheta} \end{pmatrix} = e^{-i\vartheta}\begin{pmatrix} 1 & 0 \\ 0 & e^{2i\vartheta} \end{pmatrix}. \tag{2.58}$$

In Eq. (2.58) one finds a global phase of $e^{-i\vartheta}$, which is why $e^{-i\vartheta\hat{Z}}$ will cause a 2ϑ-rotation around the Z-axis. Following [Nielsen, 2010], conventional phase gates or S-gates of the form

$$S_z = e^{-i\frac{\pi}{4}\hat{Z}} \simeq \begin{pmatrix} 1 & 0 \\ 0 & i \end{pmatrix}, \qquad S_x = e^{-i\frac{\pi}{4}\hat{X}} = \frac{1}{\sqrt{2}} \begin{pmatrix} 1 & -i \\ -i & 1 \end{pmatrix}. \tag{2.59}$$

Here, '$\simeq$' denotes 'up to the previously discussed global phase' and both quantum gates implement $\pi/2$-rotations around the Z- and X-axis respectively. An often used additional gate is given by the symmetric superposition of $\hat{X}$ and $\hat{Z}$ and is called the *Hadamard* gate

$$\hat{H} = \frac{1}{\sqrt{2}} \left(\hat{X} + \hat{Z}\right) = \frac{1}{\sqrt{2}} \begin{pmatrix} 1 & 1 \\ 1 & -1 \end{pmatrix}. \tag{2.60}$$

The effect of the Hadamard gate $\hat{H}$ is the exchange of X- and Z-eigenstates, which is why it can be viewed as a basis change. In literature, these quantum gates are referred to as *Clifford gates*. Note that there is a redundancy in the above quantum gates. If, for example, one is able to perform $\pi/2$-rotations around a given axis, then one can also rotate about π. Thus, the set $\{\hat{X}, \hat{Y}, \hat{Z}, \hat{S}_z, \hat{S}_x, \hat{H}\}$ is overcomplete in the sense that $\hat{X} = \hat{S}_x^2$, $\hat{Z} = \hat{S}_z^2$ and $\hat{Y} = i\hat{X}\hat{Z}$. Moreover, one can show that $\hat{H} \simeq \hat{S}_z\hat{S}_x\hat{S}_z$. Therefore, the single-qubit Clifford group is spanned by $\hat{S}_x$ and $\hat{S}_z$.
The above set of quantum gates is not universal. This implies that there are single-qubit operations that cannot be accomplished by only using Clifford gates. In order to achieve single-qubit universality, one has to add a non-Clifford gate. One conventional choice is the T-gate,

$$\hat{T} = \begin{pmatrix} 1 & 0 \\ 0 & e^{i\pi/4} \end{pmatrix} \simeq e^{-i\frac{\pi}{8}\hat{Z}}. \tag{2.61}$$

As Eq. (2.61) indicates, the T-gate implements a $\pi/4$-rotation of the qubit state around the Z-axis. Due to the mentioned irrelevant global phase this gate is also known as $\pi/8$-gate, but it is better to just call it T-gate [Nielsen, 2010]. The convenience of choosing the T-gate as an additional gate can be seen by $\hat{T}^2 = \hat{S}_z$. Finally, the single-qubit Clifford group in combination with the T-gate is a universal set of single-qubit gates.

Having introduced one universal set of single-qubit gates, one needs an additional operation to couple, and moreover entangle different qubits, to reach quantum-computational universality. Following [Nielsen, 2010], a convenient gate for that purpose is the controlled-NOT gate (CNOT), which is a two-qubit gate with a predefined control qubit (C) and target qubit (T). The CNOT is given by

$$\mathrm{CNOT} = \begin{pmatrix} 1 & 0 & 0 & 0 \\ 0 & 1 & 0 & 0 \\ 0 & 0 & 0 & 1 \\ 0 & 0 & 1 & 0 \end{pmatrix} = \frac{1}{2}\left(1 + \hat{Z}\right)_{\mathrm{C}} \otimes (I_2)_{\mathrm{T}} + \frac{1}{2}\left(1 - \hat{Z}\right)_{\mathrm{C}} \otimes \left(\hat{X}\right)_{\mathrm{T}}. \tag{2.62}$$

The action of CNOT depends on the control qubit's state $|\psi\rangle_{\mathrm{C}}$. If $|\psi\rangle_{\mathrm{C}} = |0\rangle_{\mathrm{C}}$, the second addend in Eq. (2.62) will be suppressed and the target qubit's state will remain unchanged. If the control qubit is in the $Z = -1$-eigenstate, the target qubit is flipped, i.e. $\hat{X}\,|\psi'\rangle_{\mathrm{T}}$. Therefore, the CNOT is also sometimes called controlled-X gate, i.e. $\hat{C}_x \coloneqq \mathrm{CNOT}$.
Following the above logic, one can implement any controlled single-qubit operation. For an arbitrary single-qubit unitary operation $\hat{U}$, the controlled-U gate is given by

$$C_U = \frac{1}{2}\left(1 + \hat{Z}\right)_{\mathrm{C}} \otimes (I_2)_{\mathrm{T}} + \frac{1}{2}\left(1 - \hat{Z}\right)_{\mathrm{C}} \otimes \left(\hat{U}\right)_{\mathrm{T}}. \tag{2.63}$$

Finally, one universal set for quantum computational purposes is given by $\{\hat{S}_x, \hat{S}_z, \hat{T}, \hat{C}_x\}$. Even though this set is still overcomplete, because of $\hat{T}^2 = \hat{S}_z$, in any platform one tends to implement an overcomplete set. The reason for this lies in the required fine-tuning or complexity in realising the respective gates. As a Pauli flip is usually much easier to implement as the T-gate, some operations will be better protected against errors than others. This observation will be met in the following sections.

2.4.2 Majorana box qubit

In 2000, David DiVincenzo formulated five requirements for the implementation of a quantum computer [DiVincenzo, 2000], which are also known as the DiVincenzo criteria. 1) The physical system requires well characterised qubits and it should be scalable. 2) The ability to initialise the state of the qubits is necessary. 3) Decoherence times have to be much longer than times related to gate operations. 4) One has to implement a universal set of quantum gates. 5) Qubit-specific read-out has to be realised. Even though all of the five requirements are self-explaining, it is useful to further analyse them in order to study a specific system for its application in quantum computation.
This section is dedicated to the Majorana box qubit (MBQ), as it allows for partially protected, topological quantum computation. As there are different proposals for the tetron architecture to, for example, implement the read-out, only one of the possible realisations will be discussed here. For a detailed discussion see [Plugge, 2017] and [Karzig, 2017].
Starting with the qubit itself, the system of interest is given by two parallel strong spin-orbit nanowires, which are proximitised by the same superconductor and exposed to a magnetic field. Moreover, the system is floating and therefore exhibiting charging effects. Thus, the qubit itself is the already discussed charging island, cf. Sec. 2.2.1. In Fig. 2.8 a), the superconductor is indicated by the backbone, but the island itself is the same as in the previous sections. Thereby, the Hamiltonian of the box is given by $\mathcal{H}_{\text{Box}}$, cf. Eq. (2.26). As long as the wire length L_W exceeds the Majorana localisation length ξ, cf. Sec. 2.1.2, the MBSs on the two topological superconductors lie at zero energy. Thus, the system will host four MZMs. The typical wire length is several micrometers [Albrecht, 2016]. Assuming that no other quasiparticles are accessible due to the protection by both the topological gap Δ_{TS} and E_C, the island itself is well-described by $\mathcal{H}_{\text{Box}}$. One can then tune the backgate of the tetron in order to reach Coulomb valley conditions, which results in the following qubit encoding, cf. Sec. 2.2.2,

$$X = i\gamma_1\gamma_2 = \pm i\gamma_4\gamma_3, \qquad Y = i\gamma_2\gamma_3 = \pm i\gamma_4\gamma_1, \qquad Z = i\gamma_1\gamma_3 = \pm i\gamma_2\gamma_4. \tag{2.64}$$

Here, the parity constraint is given by $\mathcal{P}_2 = \gamma_1\gamma_2\gamma_3\gamma_4 = \pm 1$. In the following $\mathcal{P}_2 = +1$ will be used. In Fig. 2.8 a) different Pauli operations correspond to non-locally addressing the tetron. Thereby, different qubit operations correspond to spatially distinct processes. For example a Pauli-X operation corresponds to the addressing of two MZMs, which are on the same nanowire and therefore located at opposite ends of the tetron. Therefore, the nonlocality of the Majoranas implies that any Pauli-X operation has to be non-local in the horizontal direction in Fig. 2.8 a). Analogously any Pauli-Z operation has to involve two Majoranas on different wires but the same end. Thereby, the access hardware for Pauli-Z is divided in the vertical direction in Fig. 2.8 a). These spatially distributed qubit operations result in a protection mechanism, which is of topological nature.
As Fig. 2.8 a) suggests, the qubit is well-defined by the two topological superconductors. Moreover, as Sec. 2.1.3 pointed out, one topological nanowire can be tuned to host more than two MZMs. In combination with the ability to use different wires, proximitised by different superconductors, but all exposed to the same magnetic field, this leads to scalability. Thus, criterion 1) of the above mentioned requirements is fulfilled in this

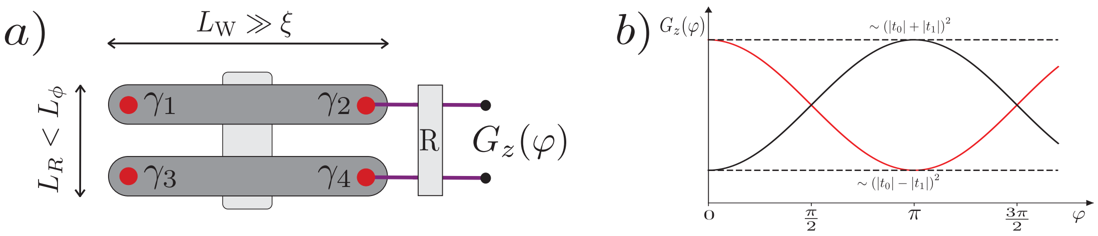

Figure 2.8: a) Schematic sketch of the Majorana box qubit (or tetron). Two topological superconductors (dark grey) with four MZMs $\gamma_{1,2,3,4}$ (red dots) are shunted by an s-wave superconductor. The wire length L_W is assumed to be much larger than the Majorana localisation length ξ in order to neglect Majorana hybridisation effects. The leads (purple) are coupled to Majorana operators γ_2 and γ_4 to probe the conductance $G_z(\varphi)$, which will depend both on the eigenvalue of $Z = i\gamma_4\gamma_2$ and the geometric phase φ. The latter arises due to interference effects, because of the reference arm R, which also connects the two leads. b) Conductance $G_z(\varphi)$ plotted against loop phase φ. The red curve belongs to $G_{z=+1}(\varphi)$ and the black curve belongs to $G_{z=-1}(\varphi)$. One point of maximal resolution is given at $\varphi = \pi$. Based on [Plugge, 2017].

proposal. In [Karzig, 2017], the scalability is addressed and shown explicitly in multiple figures.

As initialisation, decoherence times and the implementation of quantum gates correspond to the ability of manipulating quantum information stored on the island, requirements 2) to 4) of the DiVincenzo criteria are discussed in Sec. 2.4.3. Here, the read-out will first be implemented, because it relies on quantum transport through the box and is therefore easily accessible after the discussion in Sec. 2.3. In addition to the L_W constraint, read-out in the tetron architecture requires reference arms, which are short enough to allow for phase-coherent tunneling events, i.e. $L_R < L_\phi$. Here, L_R is the length of the reference arm R and L_ϕ is the length over which phase-coherent electron transport is possible. In [Gazibegovic, 2017], it was demonstrated that low-density semiconductors can be used as reference arms.

In Fig. 2.8 a) two leads are shown, which couple to γ_2 and γ_4. As the reference arm also connects the two leads, two different transport paths are accessible for an electron going from lead one into lead two. Since the box exhibits strong charging effects, one can write down the cotunneling Hamiltonian, cf. Sec. 2.3.2, corresponding to this charge transport

$$\mathcal{H}_{\mathrm{z,leads}} = \Psi_2^\dagger \left(t_0 + t_1 Z\right) \Psi_1 + \mathrm{h.c.}. \tag{2.65}$$

Following the notation in Sec. 2.3, Ψ_j is the lead-fermion operator at the boundary with the tetron. The two different paths result in a direct lead-lead connection ($\sim t_0$) and a lead-box-lead connection ($\sim t_1 \propto 1/E_C$). As $t_0, t_1 \in \mathbb{C}$, their phase difference is gauge-invariant and interference effects can be observed. Here $\varphi = arg(t_1/t_0)$ corresponds to the geometric phase of the closed tunnel loop. Since the first interference effects of that type were discussed by Ahoronov and Bohm [Aharonov, 1959], such a phase φ is sometimes referred to as Aharonov-Bohm phase.
In [Plugge, 2017], the interferometric conductance was computed as

$$G_z\left(\varphi\right) = \frac{e^2}{h}\nu_1\nu_2|t_z|^2 \qquad \text{with} \quad t_z = t_0 + t_1 z, \tag{2.66}$$

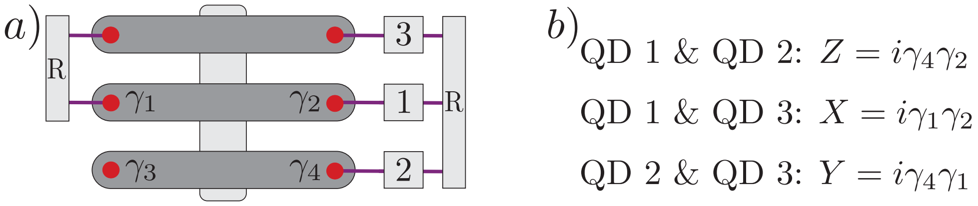

Figure 2.9: a) Schematic sketch of a Majorana box qubit (tetron) allowing for dot-based measurements of all Pauli operators. By tuning gate voltages and thereby (de-)connecting quantum dots and reference arms in combination with sweeping the occupation energy of two dots from one configuration towards the inverted configuration, topologically protected Pauli flips can be implemented. b) The quantum dots undergoing the energy sweeping are indicated along with the corresponding Pauli operation. Based on [Plugge, 2017].

where ν_j is the density of states in lead j and z is the eigenvalue of Z. Therefore, the measured conductance will strongly depend on Z. As the geometric phase φ can be changed by a magnetic field, such a conductance measurement can reveal the state of the qubit, see Fig. 2.8 b). This typically requires the phase to be tuned to a point of good resolution between the two graphs. Here electrons tunneling through both γ_2 and γ_4 experience a relative π phase-shift, which depends on the Z-eigenvalue $i\gamma_2\gamma_4 = \pm 1$. This measurement is projective and thereby collapses the state of the qubit onto either $|0\rangle$ or $|1\rangle$, cf. [Plugge, 2017]. Consequently, one way of initialising the Majorana qubit is given by performing a conductance measurement.

An alternative measurement setup is given by coupling a pair of quantum dots to the tetron. Due to the presence of Zeeman field and charging effects on the dot, they can be described by an effectively spinless single fermion level, cf. [Karzig, 2017]. In the cotunneling regime with respect to the box the measurement Hamiltonian reads

$$\mathcal{H}_{\mathrm{z,QDs}} = \frac{\epsilon}{2}\left(d_1^\dagger d_1 - d_2^\dagger d_2\right) + d_2^\dagger \left(t_0 + t_1 Z\right) d_1 + \mathrm{h.c.}. \tag{2.67}$$

Here, d_j describes the fermionic annihilation operator of quantum dot j, t_0 again corresponds to a reference arm and t_1 is the cotunneling path over the tetron. Furthermore, both quantum dots can be assumed to share a single electron. This situation is depicted in Fig. 2.9 a), where additional wires and quantum dots allow for addressing all qubit-components. Depending on the quantum dot energy ϵ, different situations can arise. For $\epsilon \gg |t_z|$, quantum dot 2 will be occupied and quantum dot 1 will be empty. If the quantum dots are tuned on resonance with the island, the electron will freely oscillate between the two quantum dots, i.e. Rabi oscillations with frequency $\omega_z = \sqrt{\epsilon^2 + |t_0 + z t_1|^2}$ occur [Plugge, 2017]. If the occupancy of one of the two quantum dots is measured, one can infer the qubit state due to these Rabi oscillations. Different measurements of the quantum dots are discussed in [Plugge, 2017]. Since the quantum dot is now measured, this provides a less invasive measurement of the MBQ. Moreover the quantum dots allow for various manipulation options, which will be discussed in the following section.

2.4.3 Majorana qubit manipulation protocols

As discussed in Sec. 2.4.2, the nonlocality of the Majoranas results in spatially distinct qubit access points. Since a Pauli-X operation has to address Majoranas on different ends of the tetron, phase-coherent transport has to be implemented in such devices. Fig. 2.9

a) represents one possible solution to that problem. Here, three quantum dots and two reference arms are sufficient to address all Pauli operators of the qubit. One of the advantages of the system is that the access hardware is essentially located at one end of the tetron. Thereby, quantum dot measurements can be implemented locally, but the topological protection of the box qubit remains.
Quantum gates can be implemented by controlled single-electron pumping events. Here, the quantum dots in Fig. 2.9 a) are used to allow for only one cotunneling event through the box. This event is then proportional to a Pauli operation, which implies that once the charge is transferred, the Pauli operation was applied. Starting with the Pauli-Z operation, one observes that quantum dot 3 should be tuned to a regime, which blocks transport over the upper topological superconducting wire. Therefore, the backgate of quantum dot 3 is tuned such that quantum dot 3 remains empty throughout the charge transfer. Moreover, the reference arm is decoupled, i.e. $t_0 \to 0$ in Eq. (2.67). If quantum dot 2 is initially occupied and quantum dot 1 is initially empty, tuning the respective backgates to a regime, where the occupation of quantum dot 1 is favoured, results in a cotunneling event. Therefore, sweeping of $\epsilon \to -\epsilon$ in Eq. (2.67) leads to a Pauli-Z flip. Afterwards, one can also measure the occupation of quantum dot 1 in order to guarantee that a qubit operation was applied.
For a Pauli-X operation one can analogously tune quantum dot 2 to be non-addressable. In this case, transferring an electron from quantum dot 1 to quantum dot 3 results in a Pauli-X operation. Note, that here, the reference arm R on the left side of Fig. 2.9 a) has to be present. Finally, a Pauli-Y operation can be applied by transferring a charge between quantum dots 2 and 3.
The implementation of Pauli flips relies only on single-electron charge pumping, where the quantum dot energies are sweeped to trigger the wanted event. This does not require fine-tuning, which, in combination with the tolerance of local errors, leads to topologically protected Pauli operations.

By also allowing for transport through the reference arm a phase gate can be implemented. In [Plugge, 2017], it was shown that one can perform different qubit rotations by changing the magnetic flux in the respective cotunneling loop. For the transport Hamiltonian in Eq. (2.67), one can tune the tunneling links to a point, where $\varphi = \mathrm{Re}(t_1/t_0) = 0$. In this case a phase gate $\hat{P}\left(\vartheta\right) = e^{-i\vartheta Z}$ with $\vartheta = -\arctan\left[\mathrm{Im}(t_1/t_0)\right]$ can be implemented. Thereby, arbitrary qubit rotations around the Z-axis are realised by fine-tuning the tunnel strengths and the magnetic flux piercing through the loop. Thus, such a phase gate heavily relies on fine-tuning and even though the Majoranas provide a natural protection mechanism, $\hat{P}(\vartheta)$ is not topologically protected. Nevertheless, it is possible to implement Clifford gates in a topologically protected manner by increasing the number of qubits.

The implementation of topologically protected Clifford gates relies on two-qubit measurements. Therefore, the concepts introduced in Sec. 2.4.2 have to be generalised in order to allow for measurements of more than a single qubit. In Eq. (2.67), two tunneling paths are shown so that the measurement outcome depends on the eigenvalue of Z. For m different tunneling paths, where each path corresponds to a single distinct Pauli flip, such a measurement can reveal a m-qubit measurement. In Fig. 2.10, this idea was used to measure the joint-parity $\langle Z_1 Z_2\rangle$, where $Z_1 = i\gamma_1\gamma_3$ and $Z_2 = i\gamma_8\gamma_4$ are the Pauli-Z operators of the two MBQs. The two different tunneling paths between quantum dot 5 and quantum dot 4 both involve a Pauli operator. Therefore, one can write down the

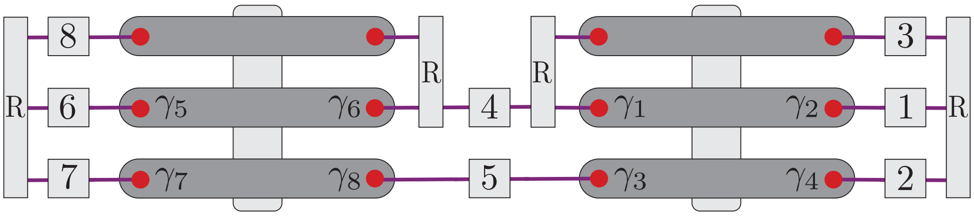

Figure 2.10: Schematic sketch of two Majorana box qubits (tetrons). By tuning the quantum dots and reference arms to facilitate certain cotunneling events, single- and two-qubit measurements can be implemented. Here, the dot occupation will depend on the chosen Pauli operators of the respective qubit (see main text). Moreover, topologically protected Pauli flips can be implemented by single-electron charge pumping events. Two tetrons allow for the implementation of measurement-based topologically protected Clifford gates. Based on [Plugge, 2017].

corresponding cotunneling Hamiltonian as

$$\mathcal{H}_{z_1 z_2,\mathrm{QDs}} = \frac{\epsilon}{2}\left(d_4^\dagger d_4 - d_5^\dagger d_5\right) + d_4^\dagger \left(t_1 Z_1 + t_2 Z_2\right) d_5 + \mathrm{h.c.}. \tag{2.68}$$

In analogy to the discussion in Sec. 2.4.2, bringing the quantum dot energies on resonance will lead to Rabi oscillations with frequency $\omega_{z_1 z_2} = \sqrt{\epsilon^2 + |t_1 Z_1 + t_2 Z_2|^2}$. Therefore, the Rabi frequency of the oscillating electron (shared by the two quantum dots) depends on the join-parity $\langle Z_1 Z_2 \rangle$. The same idea can be applied to implement other two-qubit measurements, but due to the geometry of the system the joint-parity measurement is the easiest to realise.

With one auxiliary qubit (ancilla), it is possible to realise quantum circuits, which are equivalent to $\hat{S}_x$ and $\hat{S}_z$. Such an implementation is called *measurement-based quantum gate*, because it is based on multiple measurements of the two qubits and conditioned on the measurement outcome, Pauli flips are applied. Thus, the two-tetron setup in Fig. 2.10 allows for the realisation of topologically protected Clifford gates. $\hat{S}_z$ can be implemented by first measuring the joint-parity $\langle Z_1 Z_2 \rangle \rightarrow a_1$ of the Majorana qubits 1 and the ancilla 2. Afterwards, the Pauli-X operator of the ancilla is measured, i.e. $\langle X_2 \rangle \rightarrow a_2$. Finally, conditioned on both measurements, a Pauli-Z flip is applied to qubit 1, i.e. $Z_1^{(a_1 a_2)}$. Here, Z_1 is only applied if either the joint-parity was odd ($a_1 = -1$) or the ancilla was in an X-eigenstate with negative eigenvalue (a_2), i.e. only if $a_1 a_2 = -1$. Also, an analogous implementation of $\hat{S}_x$ exist.

With the use of measurement-based quantum circuits, one can also implement a CNOT in a topologically protected way, since it will only rely on measurements and Pauli operations. Such a two-qubit quantum gate requires an additional ancilla. Therefore, two-qubit measurements and Pauli operations on three Majorana qubits are required to implement an entangling gate. For details see [Plugge, 2017].

In the case of the MBQ, it is possible to implement topologically protected Clifford gates and a protected entangling gate with the drawback of larger system sizes and the need of measurement-based protocols. Therefore, the requirements 2) and 4) of the DiVincenzo criteria are theoretically fulfilled. The problem with criterion 4) is that universality requires the implementation of the T-gate, which in the tetron architecture is given by a highly fine-tuned point of a large set of Hamiltonian parameters. As this is not experimentally feasible, a T-gate should be implemented in a different way.

A possible solution is given by a state injection algorithm. An equivalence exists between the T-gate and a CNOT, where the control is an ancilla prepared in the magic state $|m\rangle$, followed by a measurement and a conditioned $\hat{S}_z$ [Litinski, 2017]. Since all the required operations can be implemented in a protected way, the T-gate realisation is equivalent to the preparation of a qubit in the magic state

$$|m\rangle = \hat{T}\,|+\rangle = \frac{1}{\sqrt{2}}\left(|0\rangle + e^{i\frac{\pi}{4}}\,|1\rangle\right). \tag{2.69}$$

Thus, the magic state $|m\rangle$ is given by the Pauli-X eigenstate $|+\rangle$, which is rotated by $\pi/4$ around the Z-axis. Note that any Pauli eigenstate, which was rotated by $\pi/4$ around one of the other axes, can be considered a magic state. The preparation of such a state is very difficult, since it requires fine-tuning to obtain the $\pi/4$-phase.

Finally, the implementation of a quantum computer requires decoherence times to be much longer than times, which are related to gate operations. Therefore, it is important to look at the main decoherence mechanisms of the tetron. The Majorana qubit is encoded in one of the two fermion-parity manifolds of the charging island. Thus, there are two different processes, leading to decoherence. The first is given by electron tunneling. Here, the island is protected by charging energy E_C. The second mechanism comes from quasiparticles within the device. The creation of a single quasiparticle on the island changes the fermion-parity and thereby leads to decoherence. The MBQ is protected against such quasiparticles due to the gap Δ_{TS}. This implies that at temperature T the error rate Γ is exponentially suppressed by the gap, i.e. $\Gamma \sim e^{-\Delta_{\mathrm{TS}}/T}$ [Bonderson, 2013]. According to [Landau, 2016], the above discussed single-electron pumping events work beyond the adiabatic regime. Therefore, requirement 3) of the DiVincenzo criteria should be fulfilled and one can understand the MBQ or tetron architecture as an example for the elementary building block of a measurement-based topologically protected Clifford computer.

2.5 Lindblad master equations

Until now, all setups and models of interest were given by closed quantum systems. In Sec. 2.1.2, the Kitaev chain was discussed and considering an additional object, e.g. a single quantum dot, would have changed the fermion parity in the topological superconducting phase due to tunneling. By including charging effects in Sec. 2.2.1, the system of interest from Sec. 2.3 onwards included multiple topological superconductors and quantum dots or leads. Even though the system of interest consisted of coupled devices, it did not include any unwanted effects caused by an additional constituent. In experiments such a foe is always present in terms of electromagnetic fields, charge fluctuations, phonons, etc., and it is key to tune any device in a way that it is well described by a theory of a closed quantum system.

In this section the opposite will be discussed, where the model already includes unwanted degrees of freedom, which might interfere with the physics of interest. For this purpose, the following section is dedicated to Lindblad master equations. In Sec. 2.5.1, the microscopic derivation of a Lindblad master equation is discussed in a general way. Afterwards, Sec. 2.5.2 establishes the connection between the master equation and a superoperator acting inside a larger dimensional Hilbert space. This turns out to be very useful in order to discuss important information contained in the Lindblad master equation. Even though Sec. 2.5.2 provides enough tools to fully study such master equations, in Sec. 2.5.3

a different approach is discussed. This allows for a symmetry-based analysis of a Lindblad master equation.

It is worth mentioning that there is an open quantum system analogue of the Kitaev chain, [Diehl, 2011]. By carefully engineering the drive and dissipation in an cold-atomic chain, one can obtain a Lindblad master equation, where the jump operators reflect the pairing mechanism in the topological phase of the Kitaev chain, [Diehl, 2011, Bardyn, 2013, Goldman, 2016]. Thus, one obtains MBSs at the end of the driven dissipative chain.

For most of this section, the excellent books by Weiss [Weiss, 2007] and by Breuer and Petruccione [Breuer, 2006] were used. For a detailed discussion and derivation of the concepts in Sec. 2.5.3, see [Albert, 2014, Albert, 2016].

2.5.1 Microscopic derivation

In this section, the evolution of an open quantum system is described in terms of the Lindblad master equation, which is a Markov master equation. Here, tensor products are shown explicitly and all Hamiltonians do not have calligraphic symbols due to their universal nature.

In general, one might consider a system of interest S weakly coupled to a bath B with the interaction between S and B described by H_{SB}. In the following, the system of interest S coupled to a bath B will be denoted as coupled system. Thus, the Hamiltonian of the coupled system is given by

$$H\left(t\right) = H_S + H_B + H_{SB}\left(t\right), \tag{2.70}$$

where H_S, H_B describe the system, bath Hamiltonian, respectively. Note that the time dependence of this open quantum system is contained in the interaction Hamiltonian.

The starting point of the derivation is the evolution of the density matrix ρ_{SB}, which corresponds to the Hilbert space of both S and B. Switching to the interaction picture of $H_S + H_B$, the von Neumann equation is given by

$$\frac{d}{dt}\rho\left(t\right) = -i\left[H_I\left(t\right), \rho\left(t\right)\right]. \tag{2.71}$$

Here, the Hamiltonian of the coupled system is formulated in the interaction picture, i.e. $H_I\left(t\right) = UH_{SB}\left(t\right)U^\dagger$. The density matrix in the interaction picture is given by $\rho\left(t\right) = U\rho_{SB}U^\dagger$, where $U = e^{i(H_S+H_B)t}$.

Integrating Eq. (2.71), one obtains an expression for $\rho(t)$, which afterwards can be reinserted into the von Neumann equation. By tracing over the bath degrees of freedom one finds

$$\frac{d}{dt}\rho_S\left(t\right) = tr_B\left[H_I\left(t\right), \rho\left(0\right)\right] - \int_0^t d\tau\; tr_B\left[H_I\left(t\right), \left[H_I\left(\tau\right), \rho\left(\tau\right)\right]\right], \tag{2.72}$$

where the reduced density matrix, describing only the system, is denoted by $\rho_S = tr_B\rho$. Eq. (2.72) describes the evolution of $\rho_S(t)$ at arbitrary times t. Even though the state of the system might depend on its initial condition $\rho(0)$, the evolution itself should be independent of the starting point. Therefore, one can assume the first addend on the right-hand side of Eq. (2.72) to vanish, i.e. one chooses H_I such that

$$tr_B\left[H_I\left(t\right), \rho\left(0\right)\right] = 0. \tag{2.73}$$

In the later discussion one finds that the assumption in Eq. (2.73) is equivalent to the requirement of the bath to be in equilibrium.

The next step is called *Born approximation* in literature. Assuming the interaction between S and B is turned on at time $t = 0$, the initial density matrix is in a product state, i.e. $\rho(0) = \rho_S(0) \otimes \rho_B(0)$. Given that the bath is in equilibrium and the interaction between S and B is small, the influence of the system on the bath is negligible. Thus, one can treat the bath as approximately constant [Breuer, 2006] and obtains

$$\rho(t) \approx \rho_S(t) \otimes \rho_B. \tag{2.74}$$

Applying the weak coupling between S and B, one obtains the master equation in Born approximation

$$\frac{d}{dt}\rho_S(t) = -\int_0^t d\tau \; tr_B\left[H_I(t), \left[H_I(\tau), \rho_S(\tau) \otimes \rho_B\right]\right]. \tag{2.75}$$

The following steps can be summarised by the term *Markov approximation* and essentially require the bath to have delta correlation functions. This implies that any correlation between the bath and system is lost quickly. Modelling the bath as a collection of harmonic oscillators with an ohmic spectrum fulfils this requirement. Note that a bath with a sub- or super-ohmic spectrum does not necessarily behave markovian, cf. [Weiss, 2007].
One way to formulate the above condition is a comparison of τ_B, which represents the time scale over which the bath correlation function decays, and τ_R, which denotes the relaxation time of the system S, i.e. the time scale over which the state of S varies appreciably. Using the above definitions, the Markov approximation holds for $\tau_R \gg \tau_B$.
The Markov approximation consists of two steps. The first step is to derive a time-local master equation for $\rho_S(t)$. Due to the fast decay of the bath correlation function, ρ_S only depends on its current value and not on its past. One can interpret the influence on S due to correlations between S and B as a memory effect of the system. Thus, one can view a markovian bath as having no memory effects. Therefore, one can effectively replace $\rho_S(\tau)$ in Eq.(2.75) by $\rho_S(t)$.
The second step is to replace the upper bound of Eq. (2.75) by infinity. One first substitutes $\tau = t - \tau'$ and obtains $tr_B\left[H_I(t), \left[H_I(t-\tau'), \rho_S(t) \otimes \rho_B\right]\right]$ as the integrand. The new integration variable τ' indicates how far one has to go back in time to account for memory effects. Since these memory effects are short-living within the Markov approximation, the relevant contributions come from small τ'. Therefore, the upper bound can be replaced by infinity and the master equation reads

$$\frac{d}{dt}\rho_S(t) = -\int_0^\infty d\tau \; tr_B\left[H_I(t), \left[H_I(t-\tau), \rho_S(t) \otimes \rho_B\right]\right]. \tag{2.76}$$

The above equation is called *Markov master equation* in literature, cf. [Weiss, 2007, Breuer, 2006]. Since the derivation involves the Born-Markov approximation, the evolution of any system, obeying the two required assumptions (weak system-bath coupling and a Markovian bath), can be described in terms of the Markov master equation.

The Markov master equation of a system can be brought into Lindblad form by performing an additional rotating wave approximation. In order to perform the required approximation, while keeping the derivation general, it is convenient to write H_I in terms of eigenoperators A_α of the system S and bath operators B_α acting on the Hilbert space of B. The bath operators are assumed to be hermitian, i.e. $B_\alpha = B_\alpha^\dagger$, but the A_α do not have to. Thus, one can write H_I in the interaction picture with respect to H_S and H_B as

$$H_I(t) = \sum_\alpha e^{-i\omega_\alpha t} A_\alpha \otimes B_\alpha(t) + \text{h.c.} \tag{2.77}$$

Here, ω_α denotes the eigenenergy corresponding to A_α and the time-dependent bath operators are given by

$$B_\alpha\left(t\right) = e^{iH_Bt}B_\alpha e^{-iH_Bt}. \tag{2.78}$$

After writing down the interaction Hamiltonian explicitly, one can revisit Eq. (2.73), where H_I was chosen such that the Markov master equation was obtained. By defining the bath expectation value to be $\langle B_\alpha\left(t\right)\rangle = tr_B\{B_\alpha\left(t\right)\rho_B\}$, one can rewrite Eq. (2.73) as

$$0 = tr_B\left[H_I\left(t\right), \rho\left(0\right)\right] = \sum_\alpha e^{-i\omega_\alpha t}\left[A_\alpha, \rho_S\left(0\right)\right] tr_B\{B_\alpha\left(t\right)\rho_B\} + \text{h.c.}, \tag{2.79}$$

where the invariance of the partial trace under cyclic permutations was used. Thus, Eq. (2.73) can be reformulated as

$$\langle B_\alpha\left(t\right)\rangle = tr_B\{B_\alpha\left(t\right)\rho_B\} = 0, \tag{2.80}$$

which implies that reservoir averages over the bath operators vanish. In [Gau, 2020b], a situation is met, where this is achieved by normal-ordering the interaction Hamiltonian.

Continuing with the Markov equation, one can now insert Eq. (2.77) into Eq. (2.76) and thereby obtains

$$\begin{aligned}
\frac{d}{dt}\rho_S\left(t\right) &= \int_0^\infty d\tau\ tr_B\left(H_I\left(t-\tau\right)\rho_S\left(t\right)\rho_B H_I\left(t\right) - H_I\left(t\right)H_I\left(t-\tau\right)\rho_S\left(t\right)\rho_B\right) + \text{h.c.} \\
&= \sum_{\alpha,\beta} e^{i\left(\omega_\alpha-\omega_\beta\right)t}\Gamma_{\alpha\beta}\left(\omega_\beta\right)\left[A_\beta\rho_S\left(t\right)A_\alpha^\dagger - A_\alpha^\dagger A_\beta\rho_S\left(t\right)\right] + \text{h.c.} \\
&+ \sum_{\alpha,\beta} e^{\mp i\left(\omega_\alpha+\omega_\beta\right)t}\Gamma_{\alpha\beta}^{(*)}\left(\omega_\beta\right)\left[A_\beta^{(\dagger)}\rho_S(t)A_\alpha^{(\dagger)} - A_\alpha^{(\dagger)}A_\beta^{(\dagger)}\rho_S(t)\right] + \text{h.c.} \\
&+ \sum_{\alpha,\beta} e^{-i\left(\omega_\alpha-\omega_\beta\right)t}\Gamma_{\alpha\beta}^*\left[A_\beta^\dagger\rho_S\left(t\right)A_\alpha - A_\alpha A_\beta^\dagger\rho_S\left(t\right)\right] + \text{h.c.}
\end{aligned} \tag{2.81}$$

where one defined the one-sided Fourier transform $\Gamma_{\alpha\beta}$

$$\Gamma_{\alpha\beta}\left(\omega_\beta\right) = \int_0^\infty d\tau\ e^{i\omega_\beta\tau}\left\langle B_\alpha^\dagger\left(t\right)B_\beta\left(t-\tau\right)\right\rangle. \tag{2.82}$$

Recalling that the influence of the system on the bath was assumed to be weak, one simplified $\rho_B\left(t\right) \approx \rho_B$ within the Born approximation. Therefore, ρ_B is a stationary state of the bath, i.e. $\left[H_B, \rho_B\right] = 0$. The reservoir correlation functions are then homogeneous in time and one can use time-translation invariance to write

$$\left\langle B_\alpha^\dagger\left(t\right)B_\beta\left(t-\tau\right)\right\rangle = tr_B\{B_\alpha^\dagger\left(t\right)B_\beta\left(t-\tau\right)\rho_B\} = \left\langle B_\alpha^\dagger\left(\tau\right)B_\beta\left(0\right)\right\rangle$$

and see that the bath contribution to the master equation, namely $\Gamma_{\alpha\beta}\left(\omega_\beta\right)$, does not depend on time.

So far, the Markov master equation was simply rewritten in terms of a general interaction Hamiltonian H_I. In order to perform the rotating wave approximation, first one needs to define a third time scale of the open quantum system: τ_S, which is the typical time scale of the intrinsic evolution of the system S, i.e. $\tau_S \sim \left|\omega_\beta - \omega_\alpha\right|^{-1}$.
If the relaxation time of the system is much larger than the evolution due to the S-B interaction, i.e. $\tau_R \gg \tau_S$, then one can neglect fast oscillating terms within the evolution.

This effectively leads to neglecting all contributions in Eq.(2.81), for which $\omega_\beta \neq \omega_\alpha$. Moreover the fast oscillating terms $\propto e^{\pm 2i\omega_\alpha t}$ are neglected as well. Thus, one obtains the Markov master equation decomposed in eigenoperators of H_S and within the rotating wave approximation:

$$\frac{d}{dt}\rho_S\left(t\right) = \sum_\alpha \Gamma_{\alpha\alpha}\left(\omega_\alpha\right)\left[A_\alpha \rho_S\left(t\right) A_\alpha^\dagger - A_\alpha^\dagger A_\alpha \rho_S\left(t\right)\right] + h.c.. \tag{2.83}$$

Here, the index α, describing the different system operators, was enlarged to allow for a simpler description. It is convenient to decompose the one-sided Fourier transform as follows

$$\Gamma_{\alpha\beta}\left(\omega\right) = \frac{1}{2}\gamma_{\alpha\beta}\left(\omega\right) + iS_{\alpha\beta}\left(\omega\right), \tag{2.84}$$

where for fixed ω the hermitian matrix reads

$$S_{\alpha\beta}\left(\omega\right) = \frac{1}{2i}\left(\Gamma_{\alpha\beta}\left(\omega\right) - \Gamma_{\beta\alpha}^*\left(\omega\right)\right) \tag{2.85}$$

and the positive matrix is of the form

$$\gamma_{\alpha\beta} = \Gamma_{\alpha\beta}\left(\omega\right) + \Gamma_{\beta\alpha}^*\left(\omega\right) = \int_{-\infty}^{\infty} d\tau e^{i\omega\tau}\left\langle B_\alpha^\dagger\left(\tau\right) B_\beta\left(0\right)\right\rangle. \tag{2.86}$$

Using Eq.(2.84) and $\Gamma_{ab}^\dagger = \Gamma_{ba}^* = \frac{1}{2}\gamma_{ab} - iS_{ab}$ one can rewrite Eq.(2.83). Since the above master equation is already diagonal in terms of system operators A_α, the *Lindblad master equation* is obtained, [Lindblad, 1976, Lindblad, 1983],

$$\frac{d}{dt}\rho_S\left(t\right) = -i\left[H_{LS}, \rho_S\left(t\right)\right] + \sum_\alpha \gamma_\alpha\left(\omega_\alpha\right)\left(A_\alpha \rho_S\left(t\right) A_\alpha^\dagger - \frac{1}{2}\{A_\alpha^\dagger A_\alpha, \rho_S\left(t\right)\}\right). \tag{2.87}$$

The new operator

$$H_{LS} = \sum_\alpha S_{\alpha\alpha}\left(\omega_\alpha\right) A_\alpha^\dagger A_\alpha \tag{2.88}$$

provides a Hamiltonian contribution to the dynamics of the system. This Hamiltonian is often called *Lamb shift* Hamiltonian, since it leads to a renormalisation of the unperturbed energy levels similar to the Lamb shift.

The non-Hamiltonian contribution in Eq.(2.87) is called the *dissipator* of the master equation. In the above equation, the operators A_α are referred to as *jump operators* with transition rates γ_α. Since the dissipator is non-hermitian, it leads to a directed evolution, which is non-invertible. This corresponds to dissipation caused by the bath and experienced by the system. Therefore, the density matrix ρ_S will always approach a steady-state solution, i.e. $\rho_{ss} = \rho_S(t \to \infty)$. Since a steady-state solution corresponds to $\frac{d}{dt}\rho_{ss} = 0$, it is blind to the system-bath dynamics.

Lindblad master equations are often used in quantum optics systems, where the bath is given by a cavity and the system of interest are atoms or qubits, cf. [Leghtas, 2013, Liu, 2016, Touzard, 2018]. In this case the engineered dynamics leads to the atom relaxing to a state, in which it no longer interacts with the bath. For historical reasons, steady-state solutions of a Lindblad master equation are therefore also called *dark states*, [Diehl, 2008].

2.5.2 Spectrum of a Lindbladian

Throughout this thesis the Lindblad master equation is referred to as *Lindbladian*. Therefore, a Lindbladian contains a coherent part and the dissipative part. The latter is called *Lindblad dissipator*. Moreover, the right-hand side of the Lindbladian is sometimes referred to as Liouvillian, because of the derivation from the von Neumann equation. In analogy to the Liouville operator one can formulate a general Lindbladian, cf. Eq. (2.87), as

$$\frac{d}{dt}\rho(t) = \hat{\mathcal{L}}\left[\rho(t)\right] = -i\left[\hat{H},\rho(t)\right] + \sum_{\mu}\Gamma_{\mu}\mathcal{D}[\hat{J}_{\mu}]\rho(t). \tag{2.89}$$

Here, the Liouvillian is given by $\hat{\mathcal{L}}$ acting on the density matrix $\rho(t)$. Moreover, the previously discussed transition rates are now given by Γ_{μ} with corresponding jump operators $\hat{J}_{\mu}$. The Lindblad dissipator, cf. Eq. (2.87), is then defined by

$$\mathcal{D}[\hat{O}]\rho = \hat{O}\rho\hat{O}^{\dagger} - \frac{1}{2}\{\hat{O}^{\dagger}\hat{O},\rho\}. \tag{2.90}$$

In order to distinguish operators acting on the N-dimensional Hilbert space from later on introduced superoperators, the 'hats' are shown explicitly in this section.
Having derived a Lindbladian governing the dynamics of a system, it is useful to access and study its spectrum. The spectrum contains information on the steady-state, the time of approach towards that dark state and on whether that steady-state solution is unique. In general, it is possible for a system to dissipate towards a certain configuration, in which the state keeps evolving, but not due to the dissipative dynamics. A possible example is given by an atom, which has two dark states, and is placed inside a cavity. For long times the atom's state will end up in one of the two dark states, but oscillations due to the dark state degeneracy are still possibly, cf. [Touzard, 2018]. Such a feature is also accessible by studying the spectrum of a Lindbladian.

In this section, the *Choi isomorphism*, which is an elegant way to study the spectrum of a general Linbladian, will be discussed. The idea is to map the $N \times N$ density matrix $\rho(t)$ to an $N^2 \times 1$ vector $|\rho(t)\rangle$. Thereby, the action of the Liouvillian $\hat{\mathcal{L}}$ on the density matrix $\rho(t)$ can be understood as the action of an superoperator on the state $|\rho(t)\rangle$. Thus, the isomorphism maps the Liouvillian $\hat{\mathcal{L}}$ to an $N^2 \times N^2$ superoperator $\mathbf{L}$ and one can rewrite the Lindbladian as

$$\frac{d}{dt}|\rho(t)\rangle = \mathbf{L}|\rho(t)\rangle. \tag{2.91}$$

Here, the superoperator $\mathbf{L}$ acts inside a larger dimensional Hilbert space, i.e. of dimension N^2. One way of mapping the Liouvillian onto the above superoperator is given by writing the density matrix $\rho(t)$ as a vector, where the entries of $|\rho(t)\rangle$ are ordered by either columns or rows. Afterwards, one can write down the Liouvillian explicitely in its matrix form and separate entries with respect to the new vector entries. A more elegant way is to observe the correspondence $\hat{J}\rho\hat{J}^{\dagger} \leftrightarrow \left(\hat{J}\otimes\hat{J}^{*}\right)|\rho\rangle$. Thereby, the superoperator in Eq. (2.91) can be written as, cf. [Albert, 2014],

$$\mathbf{L} = -i\left(\hat{H}\otimes\mathbb{I} - \mathbb{I}\otimes\hat{H}^{*}\right) + \sum_{\mu}\Gamma_{\mu}\left(\hat{J}_{\mu}\otimes\hat{J}_{\mu}^{*} - \frac{1}{2}\mathbb{I}\otimes\left(\hat{J}_{\mu}^{\dagger}\hat{J}_{\mu}\right)^{*} - \frac{1}{2}\hat{J}_{\mu}^{\dagger}\hat{J}_{\mu}\otimes\mathbb{I}\right), \tag{2.92}$$

where $\mathbb{I} = I_N$ denotes the N-dimensional identity matrix. Note that by implementing the Choi isomorphism in accordance with Eq. (2.92), the density matrix is mapped onto a vector with respect to its rows. For a 2-dimensional system density matrix the corresponding mapping is given as

$$\rho(t) = \begin{pmatrix} a(t) & b(t) \\ c(t) & d(t) \end{pmatrix} \quad \rightarrow \quad |\rho(t)\rangle\!\rangle = (a(t), b(t), c(t), d(t))^{\mathrm{T}}\,. \tag{2.93}$$

So far, the Choi isomorphism allows to describe the Lindblad master equation as a set of coupled differential equations by increasing the effective size of the problem. Due to the simple structure of Eq. (2.91), the superoperator can be used to 'target' specific dark states, since a steady-state solution has to obey

$$\mathbf{L}|\rho_{ss}\rangle\!\rangle = 0|\rho_{ss}\rangle\!\rangle. \tag{2.94}$$

Therefore, if the system of interest is given ($\mathbf{L}$ is fixed), the problem of determining the dark state is essentially to find the eigenvector with an eigenvalue of zero. Analogously, if the system of interest can be tuned, e.g. by magnetic fields, gate voltages, etc., then $\mathbf{L}$ can be systematically changed to find conditions under which a specific (fixed) dark state $|\rho_{ss}\rangle\!\rangle$ is stabilised. The latter will be crucial in Chapter 4.

Using the Choi isomorphism, one can establish a connection between the steady-state solution of a Lindbladian and the zero eigenvalues of $\mathbf{L}$. This also relates the number of zero eigenvalues to the number of dark states. If a system has multiple dark states, also superpositions of these dark states will be invariant under the Lindblad dynamics. Therefore, it is convenient to consider any obtained steady-state solution as part of an subspace of the original Hilbert space, which is blind to the dissipation. Such subspaces are called *decoherence-free subspaces* and, since they contain multiple dark states, they are also referred to as *dark spaces*. Consequently, a Lindbladian with an unique dark state has dark space dimension $D = 1$. In particular, the number of zero eigenvalues of $\mathbf{L}$ defines the dark space dimension D.

Moreover, Eq. (2.91) implies that the solution of the Lindblad master equation is given by $|\rho(t)\rangle\!\rangle = e^{\mathbf{L}t}|\rho(0)\rangle\!\rangle$, where $|\rho(0)\rangle\!\rangle$ describes the initial density matrix - that is prior to the system-bath coupling. This indicates that one can not only study the dark space of a Lindbladian, but also the evolution of a system by diagonalising the respective superoperator $\mathbf{L}$ and thereby obtain the spectrum of the Lindbladian. The effects of different eigenvalues of the superoperator are nicely discussed in [Albert, 2014]. Here, negative eigenvalues correspond to decay and imaginary eigenvalues correspond to oscillations of the state components.

The most important information contained in the spectrum of a Lindbladian is therefore given by the smallest real part of the non-zero eigenvalues, which is called the *dissipative gap* Δ. The dissipative or spectral gap Δ reflects the characteristic time of approach towards the dark state. Thereby, one can estimate stabilisation times by Δ^{-1}. In addition, purely imaginary eigenvalues correspond to the decoherence-free subspace, and reflect oscillations. In the previous example of an atom with two dark states, one might think of Rabi oscillations between the two states. If such a system undergoes Rabi oscillations between the two dark states, it corresponds to purely imaginary eigenvalues of $\mathbf{L}$ and thereby can be predicted using the tools of this section.

2.5.3 Conserved quantities in Lindblad master equations

This section provides an alternative approach of studying the dark space of any Lindbladian. Here, the terminology and parts of Sec. 2.5.2 will be used as well. Only the results are shown in this section, since they will be used extensively in Chapter 4. For a more detailed derivation and discussion see [Albert, 2014].

The motivation for a symmetry-based analysis of the dynamics in an open quantum system is given by its equivalent in closed systems. Closed quantum systems undergo unitary evolution, which is governed by the von Neumann equation. If a closed system has any conservation law, the corresponding observable $\hat{C} = \hat{C}^\dagger$ is conserved, i.e. $\frac{d}{dt}\hat{J} = 0$, if and only if it commutes with the Hamiltonian, i.e. $[\hat{H}, \hat{C}] = 0$. Based on such a conserved quantity, one can then formulate a symmetry of the closed system, i.e. $\hat{U} = \exp(i\phi\hat{C})$, which leaves the Hamiltonian invariant. For a system undergoing unitary evolution commutation, conservation and the corresponding symmetry are equivalent. Thereby, one obtains information about a system by studying its conserved quantities.

In open quantum systems the situation is different. As an example, a conserved quantity $\hat{C}$, i.e. $\hat{\mathcal{L}}^\dagger[\hat{C}] = 0$, has not to commute with the Hamiltonian $\hat{H}$ and the jump operators $\hat{J}_\mu$, cf. Eq. (2.89), individually. It could also 'commute' with them as a whole. Luckily, the other direction still holds. Therefore, one can define a conserved quantity by the individual commutation: If $[\hat{C}, \hat{H}] = [\hat{C}, \hat{J}_\mu] = 0$, $\hat{C}$ is a conserved quantity of the open quantum system, see [Albert, 2014]. By mapping the operators onto the larger Hilbert space, cf. Sec. 2.5.2, one can construct a symmetry with corresponding superoperator $\mathbf{U} = \exp(i\phi\mathbf{C})$ with $\mathbf{C} = \mathbf{C}^\dagger$ being the superoperator analogue of $\hat{C}$. Thus, a symmetry of an open quantum system is defined by $\mathbf{U}^\dagger\mathbf{L}\mathbf{U} = \mathbf{L}$.

Such conserved quantities or 'constants of motion' can be used to discuss the steady-state subspace of a Lindbladian, since they have to be preserved throughout the evolution and thereby define properties of the dark space. For a Lindbladian with D conserved quantities $\hat{C}_{\nu=1,\ldots,D}$, one finds the commutation relations

$$\left[\hat{H}, \hat{C}_\nu\right] = \left[\hat{J}_\mu, \hat{C}_\nu\right] = 0. \tag{2.95}$$

Using an orthonormal basis, $\{\hat{M}_\mu\}_{\mu=1}^{D}$, to span the resulting D-dimensional dark space, the steady state can be written as

$$\rho_{ss} = \lim_{t\to\infty} e^{\hat{\mathcal{L}}t}\rho(0) = \sum_{\mu=1}^{D} c_\mu \hat{M}_\mu, \tag{2.96}$$

where $\rho(0)$ is the initial density matrix and the $c_\mu = \mathrm{tr}[\hat{C}_\mu^\dagger \rho(0)]$ are coefficients determining in which of the degenerate steady states the system ends up. Therefore, the operators $\hat{M}_\mu$ can be seen as basis states of the larger Hilbert space, where density matrices are described by states. Moreover, Eq. (2.96) implies that the conserved quantities are linked to the basis states. Thus, one can use conserved quantities of a Lindbladian to determine the steady state solution. Here, D is the dimension of the dark space in the larger Hilbert space. Note that this corresponds to the physical dimension $\sqrt{D}$.

One can also connect the conserved quantities of a Lindbladian to the eigenvalues of $\mathbf{L}$, discussed in Sec. 2.5.2. A unique dark state ($D = 1$) corresponds to a single zero eigenvalue. In this case the conserved quantity is given by $\hat{C}_1 = \mathbb{I}$, which means that the Lindbladian is trace-preserving. In the case of a qubit space ($D = 4$) four quantities have to be conserved and therefore, $\mathbf{L}$ has precisely four zero eigenvalues.

To summarise this section, a minimal Lindbladian will be discussed in terms of the Choi isomorphism and the symmetry-based method. Supposing a systems evolution is described by the following Lindbladian

$$\frac{d}{dt}\hat{\rho}(t) = -i\left[A\hat{\sigma}_z, \hat{\rho}(t)\right] + \Gamma\mathcal{D}\left[\hat{\sigma}_+\right]\hat{\rho}(t). \tag{2.97}$$

In this case, any conserved quantity has to commute with both $\hat{\sigma}_z$ and $\hat{\sigma}_+ \simeq (\hat{\sigma}_x + i\hat{\sigma}_y)$, where $\hat{\sigma}_{x,y,z}$ are Pauli matrices. The only commuting operator is given by $\hat{C}_1 = \mathbb{I}$ and $D = 1$. Therefore, the dark state is unique and it can be determined by the action of both the Hamiltonian and the Lindblad dissipator. For the dark space basis state $\hat{M}_1$, the commutation with the Hamiltonian, i.e. $[\hat{\sigma}_z, \hat{M}_1] = 0$, implies that $\hat{M}_1 = p\,|0\rangle\langle 0| + (1-p)\,|1\rangle\langle 1|$. By checking $\mathcal{D}[\hat{\sigma}_+]\hat{M}_1 = 0$, one obtains $p = 1$ and therefore the dark state is given by $\hat{\rho}_{ss} = \hat{M}_1 = |0\rangle\langle 0|$. The above Lindbladian describes the stabilisation of a qubit in its Pauli-Z eigenstate with eigenvalue +1.

The alternative approach is given by the Choi isomorphism. Here the mapping described in Eq. (2.92) implies that the above Liouvillian can be written as the superoperator

$$\mathbf{L} = \begin{pmatrix} 0 & 0 & 0 & \Gamma \\ 0 & -\frac{\Gamma}{2} - 2iA & 0 & 0 \\ 0 & 0 & -\frac{\Gamma}{2} + 2iA & 0 \\ 0 & 0 & 0 & -\Gamma \end{pmatrix}. \tag{2.98}$$

As the above superoperator already indicates, $\hat{\rho}_{ss} = |0\rangle\langle 0|$ is the dark state. In order to check for additional dark states, one can calculate the eigenvalues of $\mathbf{L}$ and thereby obtains the following four eigenvalues:

$$\lambda_1 = 0, \qquad \lambda_{2,3} = -\frac{\Gamma}{2} \pm i2A, \qquad \lambda_4 = -\Gamma. \tag{2.99}$$

Thus, the above Lindbladian has indeed only one dark state and the dissipative gap is given by $\Delta = \Gamma/2$. As mentioned in Sec. 2.5.2, negative eigenvalues correspond to decay and imaginary eigenvalues correspond to oscillations. As this example is a precursor to Chapter 4, eigenvalues $\lambda_{2,3}$ correspond to the damped oscillations, which are present in the stabilisation of a Majorana qubit. For this reason, not only the tools established in this section, but also this example will be met in Chapter 4.

Chapter 3

Quantum transport in coupled Majorana box systems

In this chapter, a theoretical analysis of low-energy quantum transport in coupled Majorana box devices is presented. A single Majorana box is a Coulomb-blockaded mesoscopic charging island, as was discussed in Sec. 2.2, with at least four MZMs. Setups with several Majorana boxes, where MZMs on different boxes are tunnel-coupled via short nanowire segments, are the key ingredients to recent Majorana qubit and code network proposals. Therefore, transport experiments in such setups can test the nonlocality of Majorana-based systems and the integrity of the underlying Majorana qubits.

In order to address transport and Kondo physics in coupled Majorana box devices in a comprehensive way, Sec. 3.1 starts by describing a theoretical framework suitable for tackling such problems. In particular, Abelian bosonisation in combination with the Klein-Majorana fusion allows for a highly versatile formulation of the theory. In Sec. 3.2, a detailed study of the weak-coupling regime by means of a one-loop renormalisation group (RG) analysis is presented. The system generally flows towards strong coupling, where in marked contrast to the single-impurity TKE, see Sec. 2.3.4, an effectively bosonic description no longer applies. In general, one has to take additional non-conserved local fermion parities into account, which can be represented by sets of Pauli operators. Such spin-like variables are shown to play a crucial role for an understanding of transport in basically all coupled Majorana box devices. Sec. 3.2 also contains an explicit RG analysis for two device examples of current experimental interest, including the 'loop qubit' device proposed in [Karzig, 2017]. Next, in Sec. 3.3, the strong-coupling regime, approached at very low energy scales, is addressed. By focusing on the most relevant degrees of freedom, which can be identified from the weak-coupling RG flow and by employing quantum Brownian motion arguments, cf. Sec. 2.3.4, the effective low-energy theory corresponding to this regime is derived and discussed. Employing also Emery-Kivelson-type transformations [Emery, 1992, Gogolin, 2004], Sec. 3.3 provides a non-perturbative strong-coupling analysis for both examples studied in Sec. 3.2 from the weak-coupling perspective. Finally, Sec. 3.4 contains the exact solution for quantum transport in a simple two-box device at a Toulouse point, which exhibits two-channel Kondo physics. In Sec. 3.5, the results are summarised.

This chapter is based on the included publication [Gau, 2018]. Due to the pedagogical nature of this publication, much of its content was reproduced here.

3.1 Model and effective low-energy theory

The central goal of this chapter is to understand the low-energy physics of multi-terminal junctions defined by a set of non-interacting normal-conducting leads with point-like tunnel contacts to a general coupled Majorana box network. A concrete example for such a setup is shown in Fig. 3.1. Starting in Sec. 3.1.1 with the description of the basic model for Majorana box networks and the physical assumptions behind it, Abelian bosonisation provides a powerful tool for separating the statistical (fermionic) and charge/phase (bosonic) degrees of freedom in such networks. Tunneling processes are then analysed in Sec. 3.1.2, where the distinction between simple Majorana-lead contacts, cf. Sec. 2.3.1, and non-simple junctions is treated. Finally, in Sec. 3.1.3, Coulomb valley conditions are assumed to describe the effective low-energy theory, obtained by a projection onto the charge ground state of each Majorana box in the system.

3.1.1 Setup

The primary ingredient of the here discussed networks is a single Majorana box, which for the moment is assumed decoupled from all other boxes and from all leads. For concrete layout proposals, see [Plugge, 2017, Karzig, 2017]. Following the discussion in [Béri, 2012, Altland, 2013], on energy scales well below the proximity-induced topological superconducting gap Δ_{TS}, one can neglect above-gap quasiparticle excitations. In addition, all MBSs on a given box are assumed to be located far away from each other and therefore can be viewed as MZMs. For a discussion of hybridisation effects between MBSs on a given box, see [Altland, 2014]. Thus, only Cooper pairs and MZMs have to be taken into account.

Under those conditions, the Hamiltonian of an isolated box is solely due to Coulomb charging,

$$\mathcal{H}_{\text{box}} = E_C \left(\hat{N} - n_g\right)^2 . \tag{3.1}$$

For a discussion see Sec. 2.2.1. The box charging energy E_C is approximately $E_C \approx 1$ meV for typical experimental realisations [Albrecht, 2016]. This energy scale plays a central role for all coupled box devices studied below, cf. Sec. 2.3. In particular, it facilitates phase-coherent electron transport, which in turn generates non-trivial correlations between different boxes and/or leads.

It is most convenient to adopt a gauge, where the Majorana operators do not carry charge but instead are accompanied by $e^{\pm i\varphi}$ operators whenever the box charge changes by one unit, $N \to N \pm 1$, cf. Sec. 2.2.1. By this choice, φ denotes the phase operator conjugate to $\hat{N}$, i.e. $[\varphi, \hat{N}] = i$. For each Majorana box, the charge dynamics is therefore captured by a dual pair of local bosonic fields. For illustrative purposes, the boxes are considered to harbour four MZMs. The generalisation of the discussed approach to an arbitrary even number of MZMs for a given box is straightforward.

Next, one can include the effects of a single MZM-MZM tunnel link connecting two Majorana boxes a/b, cf. Fig. 3.1, via the tunneling Hamiltonian

$$\mathcal{H}_{\text{t}} = t_{j_a k_b} \gamma_{j_a} \gamma_{k_b} e^{i(\varphi_a - \varphi_b)} + \text{h.c.} \tag{3.2}$$

with the MZM operators γ_{j_a} and γ_{k_b}. The index j_a (k_b) here means that the MZMs belong to box a (b), cf. Fig. 3.1, and the $e^{\pm i\varphi_{a,b}}$ operators describe the transfer of charge in a tunneling event. Physically, the $e^{i(\varphi_a - \varphi_b)}$ factor in Eq. (3.2) amounts to the formation of a charge dipole between both boxes. Finally, $t_{j_a k_b}$ is a microscopic tunnel amplitude

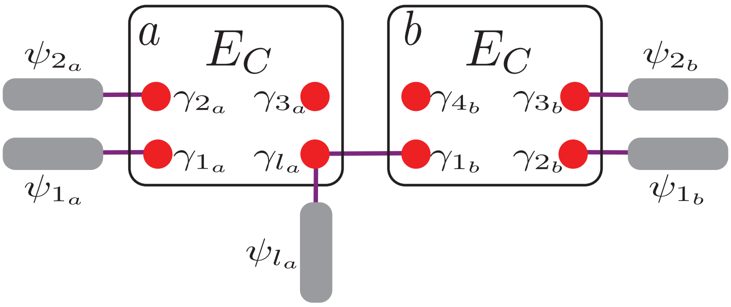

Figure 3.1: Example for a device with two Majorana boxes (a, b) connected by a single tunnel bridge (violet). Each box is subject to a charging energy E_C and hosts four MZMs with corresponding Majorana operators $\gamma_{j_{a/b}}$ (filled red circles). Both boxes are connected to several normal leads, with corresponding fermion operators $\psi_{j_{a/b}}(x)$ (indicated in grey), via lead-MZM tunnel links (violet). For box a/b, one has $M_{a/b}$ simple lead-MZM tunnel contacts. Simple contacts are characterised by an only pairwise coupling between a lead fermion operator $\Psi_{j_a} = \psi_{j_a}(0)$ and a MZM operator γ_{k_a}, see Eq. (3.3), without couplings to other leads or MZMs. For the shown case with $M_a = M_b = 2$, the only non-simple contact corresponds to lead fermion ψ_{l_a}. [Gau, 2018]

connecting the respective MZMs, e.g. through an intermediate non-topological nanowire segment.

For point-like lead-MZM tunnel contacts, one can describe each non-interacting lead by a 1D spinless fermion operator $\psi_{j_a,R/L}(x)$, see Sec. 2.3.1, where the index j_a indicates that the lead is tunnel-coupled to box a. Choosing $x = 0$ as the tunnel-contact point, right- and left-moving (R/L) fermions are defined for $x < 0$, with the open boundary conditions $\psi_{j_a,L}(0) = \psi_{j_a,R}(0)$. By a standard unfolding transformation [Gogolin, 2004], one may switch to chiral (right-moving) fermions, $\psi_{j_a}(x)$, by writing $\psi_{j_a}(x) = \psi_{j_a,R}(x)$ for $x < 0$ and $\psi_{j_a}(x) = \psi_{j_a,L}(-x)$ for $x > 0$, cf. Sec. 2.3.1. The lead-MZM contact is then described by the tunneling Hamiltonian

$$\mathcal{H}_\lambda = \lambda_{j_a k_a} \Psi^\dagger_{j_a} \gamma_{k_a} e^{-i\varphi_a} + \text{h.c.}, \tag{3.3}$$

where $\lambda_{j_a k_a}$ again is a microscopic tunneling amplitude and one employs the shorthand notation $\Psi_{j_a} = \psi_{j_a}(0)$.

All tunnel couplings will be assumed so weak that they can neither create above-gap quasiparticle excitations nor destroy the integrity of MBSs. Thus, one demands that the energy scales associated with the amplitudes $t_{j_a k_b}$ and $\lambda_{j_a k_a}$ are small compared to both Δ_{TS} and E_C. Moreover, physical tunnel contacts extend only over short distances within the coupled box device. The only exception to this rule are long-ranged pairwise cotunneling events generated via charging effects, see Sec. 3.1.3 below.

Finally, the Hamiltonian of decoupled lead no. j, cf. Eq. (2.39), is given by

$$\mathcal{H}_{\text{leads}} = -iv_F \int_{-\infty}^{\infty} dx\ \psi^\dagger_j \partial_x \psi_j, \tag{3.4}$$

where one assumes the same Fermi velocity v_F for all leads and writes $j = j_a$ for notational simplicity. Differences in Fermi velocities are negligible and can be taken into account by renormalising the above tunneling amplitudes.

So far, a fermionic description of the leads was considered. In analogy to the case of a single Majorana box, see Sec. 2.3, it is useful to switch to a bosonised description for the leads. As for the Majorana box above, fermionic (statistical) and bosonic (charge/phase) lead variables are thereby explicitly separated. While the lead Hamiltonian (3.4) admits a purely bosonic description, see Eq. (3.5) below, fermionic aspects do appear in tunneling operators connecting the respective lead to MZMs or to other leads. Performing Abelian bosonisation in terms of right- and left-movers, as was discussed in Sec. 2.3.1, one introduces dual boson fields ϕ_j and θ_j obeying the algebra $[\phi_j(x'), \partial_x\theta_k(x)] = i\pi\delta\,(x-x')\,\delta_{jk}$, and Klein factors κ_j in Majorana representation. Thereby, the lead Hamiltonian (3.4) reads [Gogolin, 2004]

$$\mathcal{H}_{\text{leads}} = \frac{v_F}{2\pi}\int_{-\infty}^{0} dx\,\left[(\partial_x\phi_j)^2 + (\partial_x\theta_j)^2\right]. \tag{3.5}$$

For a description of tunneling processes, however, Klein factors play a crucial role. Using bosonised expressions, each tunneling event is factorised into a charge-neutral fermion-bilinear part encoding the fermionic statistics and a part describing the bosonic charge (or phase) dynamics. Explicitly, for the lead-MZM tunneling Hamiltonian in Eq. (3.3), one obtains

$$\mathcal{H}_\lambda = \lambda_{j_a k_a}\kappa_{j_a}\gamma_{k_a}e^{i(\Phi_{j_a}-\varphi_a)} + \text{h.c.}, \tag{3.6}$$

where a factor $1/\sqrt{\alpha}$ has been absorbed in $\lambda_{j_a k_a}$. Here, the shorthand notation of Sec. 2.3.1, i.e. $\Phi_{j_a} = \phi_{j_a}(0)$ and $\Theta'_{j_a} = \partial_x\theta_{j_a}(0)$, was used. Note that Eq. (3.6) contains a local fermion parity operator $i\kappa_{j_a}\gamma_{k_a}$ with eigenvalues ± 1 corresponding to the occupation number of the fermion mode built from κ_{j_a} and γ_{k_a}.

3.1.2 Non-simple Majorana-lead junctions

It is convenient for the subsequent discussion to revisit the *simple* lead-MZM contact of Sec. 2.3.1. For a simple contact, see Fig. 3.2(a), the tunnel-coupled Majorana (γ_{k_a}) and lead (Ψ_{j_a}) fermions are required to have no additional tunnel couplings to other (Majorana or lead) fermions. For systems with only simple contacts, one can proceed in a straightforward manner by employing the Klein-Majorana fusion approach put forward in [Altland, 2013, Béri, 2013]. Thus, one observes that in such systems, each local fermion parity built from a Klein-Majorana operator κ_{j_a} and a MZM operator γ_{k_a} forming the respective tunnel contact, cf. Fig. 3.2(a), will be separately conserved, $i\kappa_{j_a}\gamma_{k_a} = \pm 1$. Similarly, all local parities associated with simple MZM-MZM tunnel links are conserved, $i\gamma_{j_a}\gamma_{k_b} = \pm 1$. The above observations imply that the fermionic sector of the theory is trivially solvable as long as all local fermion parities remain conserved. A coupled Majorana box system with only simple contacts can thus be reduced to a purely bosonic theory, which is generally much simpler to analyse than the original fermionic version.

All lead-MZM junctions beyond the pairwise tunnel contact in Fig. 3.2(a) are referred to as *non-simple*. Two examples of such non-simple lead-MZM contacts are shown in Figs. 3.2(b) and (c). A non-simple junction also occurs when a lead-contacted MZM is in addition tunnel-coupled to another MZM on an adjacent box, see Fig. 3.1. Similarly, one may refer to non-simple MZM-MZM junctions if several MZMs on distinct boxes are coupled to each other.

In this chapter the situation is addressed, where some of the above local fermion parities are not conserved anymore. This may happen if unintentional parity-breaking mechanisms are present, e.g. when a conventional mid-gap Andreev state is accidentally centered near a lead-contacted MBS and thereby activates quasi-particle poisoning mechanisms [Plugge, 2016a]. Nevertheless, the focus of this chapter lies on intentional parity-breaking

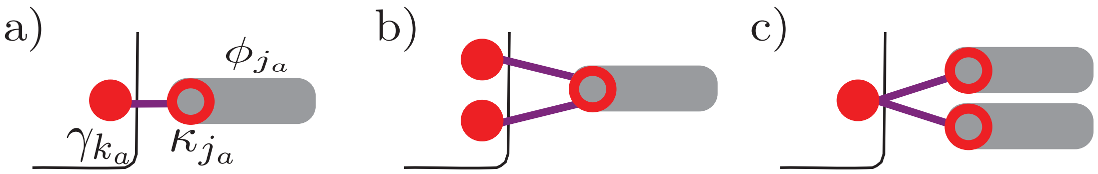

Figure 3.2: Simple vs non-simple lead-MZM tunnel junctions. Filled red circles correspond to MZMs γ_{k_a} and open red circles to Klein-Majorana operators κ_{j_a} within a bosonised description of lead fermions, see Eq. (2.41). (a) Simple contact, cf. Eq. (2.45). (b) Non-simple contact between two MZMs and one lead, cf. Eq. (3.7). (c) Non-simple contact between one MZM and two leads, cf. Eq. (3.8). [Gau, 2018]

effects due to non-simple tunnel contacts. Such cases pertain to many Majorana box transport setups and quantum-information processing applications. In fact, local parity conservation implies that for systems with only simple contacts, MZMs cannot reveal their underlying fermionic statistics, since different measurement bases are not accessible. With the above motivation, one can now inspect several generic scenarios with at least one non-simple contact, where in- or out-tunneling of charge from the box can take place either via different MZMs on the box [Fig. 3.2(b)] or through different leads [Fig. 3.2(c)]. The presence of such contacts has important consequences on low-energy quantum transport in coupled Majorana box junctions since the corresponding local fermion parities defined above are not conserved anymore. In particular, after a sequence of tunneling events, some of these parities may have been flipped along with a charge transfer between different leads. Similar processes have been discussed in [Kashuba, 2015, Plugge, 2016a] and are known to affect transport properties.

It is useful to identify subsets of (MZM and Klein factor) Majorana operators with conserved overall parity. Such a subset must contain an even number m of Majorana operators, where the corresponding Majorana bilinears generate a spin operator with symmetry group SO(m) [Béri, 2012, Altland, 2013, Béri, 2013, Altland, 2014]. For both cases in Figs. 3.2(b,c), three Majorana operators are coupled together at the junction. Taking into account a dummy Majorana mode not shown in Fig. 3.2, the parity associated with these Majorana states is conserved. As a consequence, the Majorana bilinears resulting from this subset can equivalently be described by Pauli operators $\sigma_{x,y,z}$, cf. Sec. 2.2.2, as will be discussed next.

As a first example, one might consider the situation in Fig. 3.2(b), where two Majorana operators (γ_x, γ_y) on the same box are tunnel-coupled with amplitudes $\lambda_{x,y}$ to a single lead. The latter is described by the fermion operator $\Psi^\dagger \sim \kappa e^{i\Phi}$. Including also a finite overlap integral between the MBSs (h_z), the corresponding tunneling Hamiltonian (3.3) takes the form

$$\mathcal{H}_{2,1} = (\lambda_x \sigma_x + \lambda_y \sigma_y) e^{i(\Phi - \varphi)} + \text{h.c.} + h_z \sigma_z, \qquad \text{with} \quad \sigma_{x,y} = i\kappa\gamma_{x,y}, \quad \sigma_z = i\gamma_y\gamma_x. \quad (3.7)$$

For a specific phase relation between λ_x and λ_y, the same model describes quasiparticle poisoning effects for the single-impurity TKE. As shown in [Plugge, 2016a], in the presence of additional leads, the RG flow will generate an additional hybridisation term $\sim \sigma_z \Theta'$ between a Pauli operator and the boundary fermion density. In Sec. 3.2.3, the generalisation of this to arbitrary complex $\lambda_{x,y}$ will be discussed.

Next, an alternative setup shown in Fig. 3.2(c), where one MZM (γ) is tunnel-coupled to two leads with amplitudes $\lambda_{x,y}$, is treated. The respective lead fermions are now written

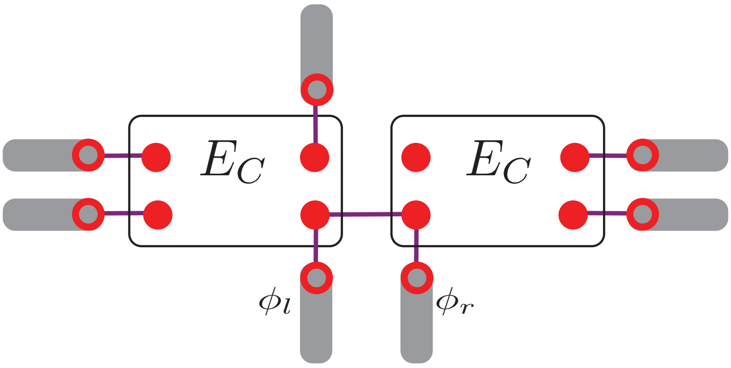

Figure 3.3: Two-box setup with a single tunnel bridge connecting the two boxes. Two central leads with boson fields $\Phi_{l,r} = \phi_{l,r}(0)$ are tunnel-coupled to the respective MZMs, see Eq. (3.9). Because of the presence of the MZM-MZM link, those lead-MZM contacts are non-simple. In addition, $M_{L/R}$ leads are attached to the left/right box via simple contacts, where the shown example is for $M_L = 3$ and $M_R = 2$. [Gau, 2018]

as $\Psi^\dagger_{x,y} \sim \kappa_{x,y} e^{i\Phi_{x,y}}$. From Eq. (3.3), the tunneling Hamiltonian is then given by

$$\mathcal{H}_{1,2} = \left(\lambda_x \sigma_x e^{i\Phi_x} + \lambda_y \sigma_y e^{i\Phi_y}\right) e^{-i\varphi} + \text{h.c.}, \qquad \text{with} \quad \sigma_{x,y} = i\gamma\kappa_{x,y} \tag{3.8}$$

Note that there is no $h_z\sigma_z$ contribution with $\sigma_z = i\kappa_y\kappa_x$. Direct lead-lead tunneling processes (if present) would produce different terms.

One also observes that, as long as an arbitrary coupled box system does not admit tunneling paths forming closed loops, all relative phases between tunneling amplitudes can be absorbed by suitable shifts of lead boson fields and thus do not affect the physics. Here, closed loop configurations in Hilbert space may arise from ring exchange processes involving several boxes, for instance, a plaquette operator in Majorana code networks [Landau, 2016]. A closed loop is also found for a lead coupled to several MZMs on the same box, see Fig. 3.2(b). While the relative phase between λ_x and λ_y can be gauged away for the case shown in Fig. 3.2(c), this is no longer possible for the setup in Fig. 3.2(b).

A more complicated example for a system with non-simple contacts can be analysed by considering the two-box setup in Fig. 3.3. Similar setups arise in basic Majorana qubit and multi-box measurements [Plugge, 2017, Karzig, 2017] and in the context of stabiliser codes [Landau, 2016, Plugge, 2016b]. Here the left/right ($a = L/R$) box is connected to an arbitrary number $M_{L/R}$ of normal leads via simple lead-MZM contacts. Figure 3.3 shows the case of $M_L = 3$ and $M_R = 2$. In addition, two central leads with the respective fermion operator $\Psi^\dagger_{l/r} \sim \kappa_{l/r} e^{i\Phi_{l/r}}$ are connected to the left/right box through non-simple contacts to the respective MZM operator $\gamma_{l/r}$ (with tunneling amplitude $\lambda_{l/r}$). The contacts are non-simple because γ_l and γ_r are tunnel-coupled by an amplitude t_{LR}. With the box phase operators $\varphi_{L/R}$, the corresponding central part of the coupled device is described by the Hamiltonian

$$\mathcal{H}_\text{c} = t_{LR}\sigma_z e^{i(\varphi_L - \varphi_R)} + \lambda_l \sigma_x e^{i(\varphi_L - \Phi_l)} + \lambda_r \sigma_x e^{i(\varphi_R - \Phi_r)} + \text{h.c.}, \tag{3.9}$$

where one defines $\sigma_z = i\gamma_l\gamma_r$ and $\sigma_x = i\gamma_l\kappa_l$. Note that one can also write $\sigma_x \sim i\gamma_r\kappa_r$ since the central junction parity $\gamma_l\gamma_r\kappa_l\kappa_r = \pm 1$ is conserved. The appearance of different Pauli operators in Eq. (3.9) suggests that for $\lambda_{l/r} \neq 0$, the two-box setup in Fig. 3.3 is more difficult to analyse than a purely bosonic counterpart with only simple contacts, e.g. without the central leads in Fig. 3.3.

3.1.3 Cotunneling regime

The subsequent discussion will focus on systems where all Majorana boxes are operated at near-integer n_g, i.e. the charge on each box has a quantised ground-state value. While near-degenerate box charge states (with n_g close to half-integer values) can change details of the TKE [Herviou, 2016, Michaeli, 2017], they do not involve additional non-conserved fermion parity degrees of freedom (here represented by Pauli operators). For weak tunneling amplitudes and nearly integer n_g on all boxes, the system is described by cotunneling amplitudes connecting in principle any pair of leads in the system via phase-coherent second- or higher-order charge tunneling processes. To obtain the corresponding cotunneling amplitudes in a systematic way, one employs a Schrieffer-Wolff transformation to project the full theory to the quantised charge ground-state sector of all boxes, see Sec. 2.3.2.

The projected cotunneling Hamiltonian will now contain qualitatively different terms. First, there are *purely bosonic* cotunneling contributions. Such processes do not involve Pauli operators representing non-conserved fermion parities and have the schematic form

$$\mathcal{H}_{\mathrm{bos}} = J_{j_a k_b} e^{i(\Phi_{j_a} - \Phi_{k_b})} + \mathrm{h.c.} \qquad \text{with} \quad J_{j_a k_b} \simeq \frac{\lambda_{j_a j'_a} \lambda^*_{k_b k'_b}}{E_C} \prod_{\langle l,l' \rangle} \frac{t_{ll'}}{E_C}. \tag{3.10}$$

The cotunneling amplitude $J_{j_a k_b}$ contains the initial and final lead-MZM couplings $\lambda_{j_a j'_a}$ and $\lambda^*_{k_b k'_b}$ for charge tunneling to/from lead j_a/k_b via box a/b, see Eqs. (3.3) and (3.6). (Here, $a = b$ is possible.) As a result of the projection to the charge ground-state sector, the $e^{\pm i\varphi_{a/b}}$ terms are no longer present in Eq. (3.10) and become effectively replaced by $1/E_C$ factors in the cotunneling amplitude, see Sec. 2.3.2. In order to obtain a contribution for lead pairs attached to different boxes ($a \neq b$), a sequence of intermediate MZM-MZM tunneling events with respective amplitudes $t_{ll'}$, cf. Eq. (3.2), is necessary. For them to contribute to Eq. (3.10), however, such MZM-MZM links must have conserved local parities. Note that since for each additional tunneling event, the contribution to $J_{j_a k_b}$ gets suppressed by a factor $|t_{ll'}|/E_C \ll 1$, the shortest tunneling path(s) between a chosen pair of leads will dominate.

In contrast to the purely bosonic case in Eq. (3.10), one now considers the consequences of the tunneling path connecting leads j_a and k_b involving a string of Pauli operators $\sigma^m = \sigma^m_{x,y,z}$. Here, σ^m describes the non-conserved local fermion parity at the mth non-simple link along the path. For a string of $n \geq 1$ Pauli operators ($m = 1, \ldots, n$), the projected Hamiltonian has the schematic form

$$\mathcal{H}_{\mathrm{nbos}} = J^{(\sigma^1,\ldots,\sigma^n)}_{j_a k_b} \sigma^1 \cdots \sigma^n e^{i(\Phi_{j_a} - \Phi_{k_b})} + \mathrm{h.c.}, \tag{3.11}$$

where $J^{(\{\sigma\})}_{j_a k_b}$ is a cotunneling amplitude as in Eq. (3.10) and the superscript denotes that this amplitude applies to a specific tunneling path involving the corresponding Pauli operator string. Concrete examples for this notation will be given in Sec. 3.2. Note that with the conventions $J^{(\{\sigma\})}_{j_a k_b} \to J_{j_a k_b}$ and $\sigma^1 \cdots \sigma^n \to 1$ for $n = 0$, i.e. in absence of non-simple links, Eq. (3.10) constitutes just a special case of Eq. (3.11).

There exist additional complexities in tunneling at a non-simple junction which comprises multiple Pauli operators of the same set $\sigma_{x,y,z}$. For example, at non-simple contacts in Fig. 3.2(b,c), elemental tunneling events may involve anticommuting Pauli operators σ_x and σ_y. The corresponding path contribution now exhibits an extra suppression factor $\sim |\Delta n_g|$, where Δn_g is the detuning of the backgate parameter n_g away from integer values. This suppression arises from the destructive interference between tunneling events with different time ordering [Landau, 2016, Plugge, 2016b]. In particular, if the box is tuned precisely to a Coulomb valley center, $\Delta n_g = 0$, such paths give no contribution at all. For finite Δn_g, both Pauli operators effectively combine to the third Pauli operator, e.g. $\sigma_x \sigma_y = i\sigma_z$. With this change and including the $|\Delta n_g|$ factor, the cotunneling contribution is then again given by Eq. (3.11).

Furthermore, in coupled box devices allowing for closed loops, see Sec. 3.1.2, elemental tunneling events, which connect to distinct MZMs, may lead to the same charge transfer. Therefore, several distinct paths with different Pauli operator content can contribute to a given cotunneling term $\sim e^{i(\Phi_{j_a} - \Phi_{k_b})}$. Such effects have been exploited, for instance, for MBQ readout and manipulation schemes, cf. Sec. 2.4. Below, cases with interfering paths are not considered, or if present, as for the loop qubit device in Sec. 3.2.3 and 3.3.4, they are explicitly separated.

3.2 Renormalisation-group analysis

Applying the composition rules for cotunneling Hamiltonians in Sec. 3.1.3, the derivation and analysis of the one-loop RG equations, cf. Sec. 2.3.3, is discussed. General coupled Majorana box devices under Coulomb valley conditions are studied, where non-conserved local fermion parities are described by Pauli operators $\sigma^m = \sigma^m_{x,y,z}$ at the mth link. In Sec. 3.2.1, construction principles for RG equations for systems of this type are introduced based on the OPE technique. Subsequently, two device examples will be discussed in order to illustrate typical effects caused by non-conserved local fermion parities.

3.2.1 General derivation of RG equations

In order to obtain RG equations via the OPE approach, one considers arbitrary pairs of cotunneling operators contributing to $\mathcal{H}$ in Eq. (3.11). For two operators acting at almost coinciding (imaginary) times τ and τ', the result of such a contraction must be equivalent to a linear combination of all possible operators at time $(\tau + \tau')/2$, where the respective expansion coefficients directly determine the one-loop RG equations, see Sec. 2.3.3. Thus, one has to analyse contractions of cotunneling operator pairs. Denoting the corresponding amplitudes by $J^{(\{\sigma\})}_{jm}$ and $J^{(\{\sigma'\})}_{mk}$, their contraction renormalises the tunneling amplitude $J^{(\{\sigma''\})}_{jk}$, where the Pauli string $\{\sigma''\}$ results from multiplication of both operator strings. This composite tunneling amplitude thus connects leads j and k by a tunneling path touching lead m and back. The RG equations now depend on whether the Pauli strings $\sigma^1 \cdots \sigma^n$ and $\sigma^{1'} \cdots \sigma^{n'}$ commute or anticommute.

For commuting Pauli strings, the OPE approach yields the general RG equations

$$\frac{dJ^{(\{\sigma''\})}_{jk}}{d\ell} = \sum_{m \neq (j,k)} J^{(\{\sigma\})}_{jm} J^{(\sigma')}_{mk}. \tag{3.12}$$

This result is simple to understand if both Pauli strings do not share overlapping Pauli operators at all, cf. Sec. 2.3.3. The composite tunneling path is then obtained by stitching together both paths, and the Pauli string $\{\sigma''\}$ corresponds to the product of the strings $\{\sigma\}$ and $\{\sigma'\}$. Moreover, if identical Pauli operators appear in both strings, say, σ^m_x and $\sigma^{m'=m}_x$, they effectively square to unity and thus drop out in the string $\{\sigma''\}$. In the following, Eq. (3.12) is discussed in more detail and for different cases of interest.

To that end, it is convenient to introduce the concept of *bosonic subsectors* (or simply subsectors). A bosonic subsector $\mathcal{B}$ refers to a group of M leads (with index $j \in \mathcal{B}$) which are coupled to each other through purely bosonic cotunneling processes, and hence undergo purely bosonic interactions within the subsector, cf. Eq. (3.10). For example, this happens for simply-coupled leads that are attached to the same box. If two leads cannot be connected via purely bosonic cotunneling processes, i.e. if a Pauli string is involved, they must belong to distinct subsectors. In particular, a lead with a non-simple lead-MZM contact generally defines its own subsector with $M = |\mathcal{B}| = 1$. According to this definition, all leads in a general Majorana network uniquely belong to one of its corresponding subsectors.

First, one can revisit the system discussed in Sec. 2.3. Here M leads are attached to a given box via simple lead-MZM contacts, thus forming a subsector $\mathcal{B}$. In the simplest case, the Hamiltonian describing purely bosonic cotunneling processes within this subsector follows from Eq. (3.10) by summing over all tunneling paths connecting lead $j \neq k$ (with $j, k \in \mathcal{B}$). Such processes have amplitude J_{jk} and couple different leads only via the lead boson fields Φ_j and Φ_k. Adapting Eq. (3.12) to this purely bosonic problem, one can reproduce the RG equations for the single-impurity TKE, cf. Eq. (2.51),

$$\frac{dJ_{jk}}{d\ell} = \sum_{m\in\mathcal{B}, m\neq(j,k)} J_{jm}J_{mk}. \tag{3.13}$$

For a discussion see Sec. 2.3.3 and Sec. 2.3.4.

Apart from the purely bosonic processes behind Eq. (3.13), cotunneling events also can kick the system out of a bosonic subsector $\mathcal{B}_1$ into a distinct subsector $\mathcal{B}_2$, which may belong to the same or to another box. By definition, such processes involve a string $\sigma^1 \cdots \sigma^n$ of $n \geq 1$ Pauli operators. The corresponding Hamiltonian reads, cf. Eq. (3.11),

$$\mathcal{H}_{\text{nbos}} = \sum_{j\in\mathcal{B}_1}\sum_{k\in\mathcal{B}_2} J_{jk}^{(\{\sigma\})}\sigma^1\cdots\sigma^n e^{i(\Phi_j-\Phi_k)} + \text{h.c.} \tag{3.14}$$

Thus, one can study the way in which the RG equations in Eq. (3.13) for purely bosonic couplings J_{jk} with $j \neq k \in \mathcal{B}$ are modified by the inter-subsector cotunneling processes in Eq. (3.14). In general, such an excursion from lead $j \in \mathcal{B}$ to some other subsector $\mathcal{B}_2$ must involve a Pauli string $\sigma^1 \cdots \sigma^n$ with $n \geq 1$. In order to contribute to the RG flow of the purely bosonic coupling J_{jk}, however, the tunneling path must now return to lead $k \in \mathcal{B}$ via the *same* Pauli operator string. As a result, for coupled-box networks, the RG equations for the TKE in Eq. (3.13) receive an additional contribution,

$$\frac{dJ_{jk}}{d\ell} = \sum_{m\in\mathcal{B}, m\neq(j,k)} J_{jm}J_{mk} + \sum_{m\notin\mathcal{B}} J_{jm}^{(\{\sigma\})}J_{mk}^{(\{\sigma\})}. \tag{3.15}$$

Fig. 3.4 illustrates one example for a tunneling process contributing to Eq. (3.14) in a rather advanced device with four boxes. The different examples in Fig. 3.4 also serve to show the general applicability and versatility of the here discussed formalism for arbitrary coupled box devices.

From the general equations (3.12), one obtains the RG equations for the cotunneling amplitudes $J_{jk}^{(\{\sigma\})}$, with leads $j \in \mathcal{B}_1$ and $k \in \mathcal{B}_2$ belonging to different subsectors

$$\frac{dJ_{jk}^{(\{\sigma\})}}{d\ell} = \sum_{m\in\mathcal{B}_2, m\neq k} J_{jm}^{(\{\sigma\})}J_{mk} + \sum_{m\in\mathcal{B}_1, m\neq j} J_{jm}J_{mk}^{(\{\sigma\})}. \tag{3.16}$$

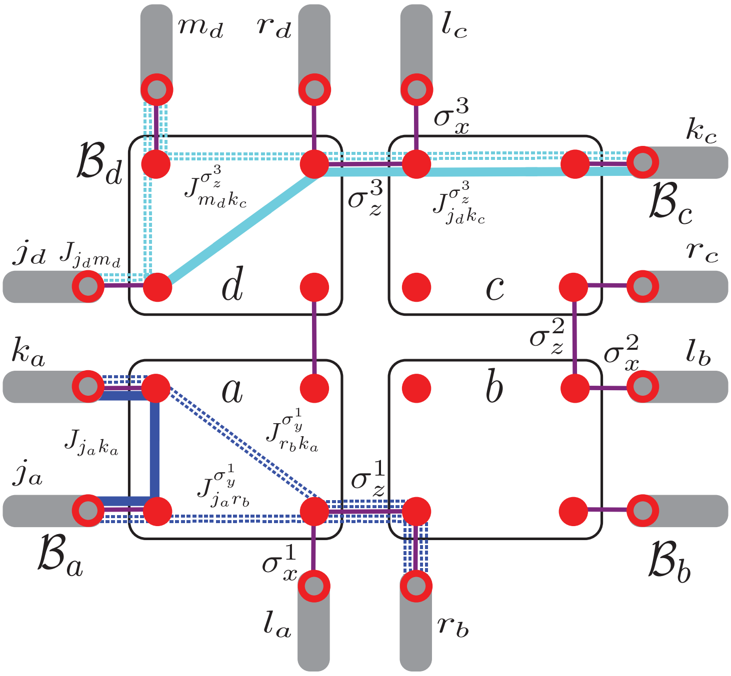

Figure 3.4: Example for a coupled Majorana box device with four boxes (a, b, c, d). The bosonic subsectors $\mathcal{B}_{a,b,c,d}$ contain $M_a = M_d = 2$ and $M_b = M_c = 1$ leads with simple lead-MZM contacts to the respective box. The device has four MZM-MZM tunnel bridges and three pairs of central leads $[(l_a, r_b)$, (l_b, r_c), and $(l_c, r_d)]$ with non-simple lead-MZM contacts. Each central lead also forms its own subsector. Non-conserved local fermion parities are encoded by Pauli operators $\sigma_{x,y,z}^{m=1,2,3}$. It also illustrates how RG terms arise from contractions of cotunneling operators: (i) For $j_a \neq k_a \in \mathcal{B}_a$, the second term in Eq. (3.15) is due to contraction of $J^{(\sigma_y^1)}_{j_a r_b}$ and $J^{(\sigma_y^1)}_{r_b k_a}$ (dashed dark blue line) which renormalises $J_{j_a k_a}$ (solid dark blue). (ii) For lead indices $j_d \neq m_d \in \mathcal{B}_d$, the contraction of $J_{j_d m_d}$ and $J^{(\sigma_z^3)}_{m_d k_c}$ (dashed cyan) renormalises the amplitude $J^{(\sigma_z^3)}_{j_d k_c}$ (solid cyan), cf. Eq. (3.16). [Gau, 2018]

The first (second) term comprises an inter-sector transition followed by a intra-sector tunneling in $\mathcal{B}_2$ ($\mathcal{B}_1$). Note that on top of the terms in Eq. (3.16), higher-order tunneling excursions via distinct subsectors $\mathcal{B}' \neq \mathcal{B}_{1,2}$ may generate additional contributions. For the applications below, however, such complications are absent.

Next, the case of anticommuting Pauli strings $\{\sigma\}$ and $\{\sigma'\}$ is discussed. Using the relation $\mathcal{T}_\tau \sigma_x(\tau)\sigma_y(\tau') = i\sigma_z(\tau)\mathrm{sgn}(\tau - \tau')$ for $\tau \to \tau'$ (and cyclic permutations thereof), with the time-ordering operator $\mathcal{T}_\tau$, one first observes that contributions with different time ordering will interfere destructively. As a consequence, there will be no additional contributions to the RG equations (3.15) and (3.16) from such tunneling events.
However, other types of RG terms can be generated in systems allowing for closed loops, where subsectors can be connected through distinct tunneling paths with different Pauli strings. To this end, one can pick a tunneling path which starts at lead $j \in \mathcal{B}$, makes an excursion to a lead in some other subsector, $l \notin \mathcal{B}$, and phase-coherently returns back to lead j. To illustrate this principle, here one focuses on the simplest scenario, where the Pauli strings $\{\sigma'\}$ and $\{\sigma\}$ for back- and forth-tunneling, respectively, are identical except at one link (m). At this link, one has anticommuting Pauli operators, e.g. σ_x^m and σ_y^m.

Contracting both cotunneling operators schematically yields

$$J_{jl}^{(\ldots\sigma_x^m\ldots)}(\cdots\sigma_x^m\cdots)_\tau J_{lj}^{\left(\ldots\sigma_y^m\ldots\right)}(\cdots\sigma_y^m\cdots)_{\tau'} \sim J_{jl}^{(\ldots\sigma_x^m\ldots)}J_{lj}^{\left(\ldots\sigma_y^m\ldots\right)}\; i\sigma_z^m(\tau)\mathrm{sgn}(\tau-\tau'), \tag{3.17}$$

where all other Pauli operators apart from $\sigma_{x,y}^m$ square out. Expanding also the $e^{\pm i\Phi_j}$ factors, which appear in all cotunneling operators to lowest order in $\tau-\tau'$, one encounters another $\mathrm{sgn}(\tau-\tau')$ factor and therefore a finite contribution to the RG equations. Using the lead densities near the respective contacts, $\Theta_j'(\tau)=\partial_x\theta_j(x=0,\tau)=-i\partial_\tau\phi_j(x=0,\tau)$, one then obtains a new contribution generated by such contractions,

$$\mathcal{H}_{\mathrm{hyb}}=\sum_j\Lambda_j\sigma_z^m\Theta_j', \tag{3.18}$$

describing a hybridisation between σ_z^m and the lead fermion densities Θ_j'. Depending on the application, the coupling in Eq. (3.18) may involve other or even multiple Pauli operators.

From Eq. (3.17), the RG flow of the coupling constants in Eq. (3.18) is then governed by

$$\frac{d\Lambda_j}{d\ell}\sim\sum_{l\notin\mathcal{B}}J_{jl}^{(\ldots\sigma_x^m\ldots)}J_{lj}^{\left(\ldots\sigma_y^m\ldots\right)}+\mathrm{h.c.} \tag{3.19}$$

Thus, hybridisation couplings will be dynamically created during the RG flow even for vanishing bare coupling, i.e. for $\Lambda_j(\ell=0)=0$. The Λ_j are real-valued couplings which are effectively controlled by the sine or cosine of the loop phase

$$\varphi_j^{\mathrm{loop}}=\arg\left(\sum_{l\notin\mathcal{B}}J_{jl}^{(\ldots\sigma_x^m\ldots)}J_{lj}^{\left(\ldots\sigma_y^m\ldots\right)}\right). \tag{3.20}$$

Importantly, the hybridisations in turn feed back into the RG equations (3.16) for cotunneling amplitudes. In fact, one finds that Eq. (3.16) receives the additional contributions

$$\frac{dJ_{jl}^{\left(\ldots\sigma_{x/y}^m\ldots\right)}}{d\ell}\sim\left(\Lambda_l-\Lambda_j\right)J_{jl}^{\left(\ldots\sigma_{y/x}^m\ldots\right)}. \tag{3.21}$$

For the loop qubit example studied below, see Secs. 3.2.3, such RG feedback effects turn out to be crucial.

The above rules show that RG equations for a general coupled Majorana box system can be determined by contracting pairs of tunneling operators. Commuting tunneling operators generate new composite tunneling operators and/or renormalise existing couplings, see Eqs. (3.15) and (3.16). Contractions of non-commuting operators, on the contrary, do not contribute to the latter RG equations. However, in systems with tunneling paths forming closed loops, hybridisation terms between Pauli operators and lead fermion densities will be generated. Such terms will in turn feed back into the RG equations for the cotunneling amplitudes.

Next, two examples of practical interest are discussed in terms of the above RG analysis.

3.2.2 Two tetron device

As a first example, a two-box device as shown in Fig. 3.3 is studied. One observes that such a system does not admit tunneling paths forming closed loops, and thus the

RG equations do not involve the hybridisations in Eq. (3.18). Using $\mathcal{H}_{\text{leads}}$ in Eq. (3.5) and taking into account the central junction described by Eq. (3.9), the Hamiltonian $\mathcal{H} = \mathcal{H}_{\text{leads}} + \mathcal{H}_L + \mathcal{H}_R + \mathcal{H}_{LR}$ is obtained by a Schrieffer-Wolff transformation to the ground-state charge sector of both boxes, see Sec. 3.1.3. In particular, cotunneling processes involving only boson fields connected to the left/right (L/R) box are contained in

$$\mathcal{H}_{L/R} = -\sum_{j,k\in\mathcal{B}_{L/R},j\neq k} (J_{L/R})_{jk}\cos\left(\Phi_j - \Phi_k\right) - \sum_{j\in\mathcal{B}_{L/R}} (J_X)_{l/r,j}\sigma_x \cos\left(\Phi_{l/r} - \Phi_j\right), \quad (3.22)$$

where $\mathcal{B}_{L/R}$ denotes bosonic subsectors with $M_{L/R}$ leads connected to the respective box via simple lead-MZM contacts. (For the example in Fig. 3.3, $M_L = 3$ and $M_R = 2$.) The central leads in Fig. 3.3, with boson fields $\Phi_{l/r}$, are coupled to the L/R box via non-simple contacts, where non-conserved local fermion parities are encoded by the Pauli operators $\sigma_{x,y,z}$, see Eq. (3.9). Inter-box cotunneling processes are described by

$$\begin{aligned} \mathcal{H}_{LR} &= -\sum_{j\in\mathcal{B}_L} (J_Y)_{rj}\ \sigma_y \cos\left(\Phi_r - \Phi_j\right) - \sum_{k\in\mathcal{B}_R} (J_Y)_{lk}\ \sigma_y \cos\left(\Phi_l - \Phi_k\right) \qquad (3.23) \\ &+ \sum_{j\in\mathcal{B}_L,k\in\mathcal{B}_R} (J_Z)_{jk}\ \sigma_z \sin\left(\Phi_j - \Phi_k\right). \end{aligned}$$

The $J_{L/R}$ amplitudes in Eq. (3.22) are purely bosonic intra-sector couplings as in Sec. 3.2.1. The J_X (resp., J_Y) cotunneling amplitudes connect leads within bosonic subsector $\mathcal{B}_{L/R}$ to the central lead on the same (resp., other) box, involving the Pauli string σ_x (resp., σ_y). Finally, the J_Z amplitudes link the bosonic subsectors $\mathcal{B}_L$ and $\mathcal{B}_R$ by inter-box tunneling via the Pauli string σ_z.

In total, there are seven coupling families: $J_{L/R}, J_{X,l/r}, J_{Y,r/l}$, and J_Z. The respective coupling matrix elements depend on microscopic lead-MZM (λ_j) and MZM-MZM (t_{LR}) tunneling amplitudes, cf. Eq. (3.9). Schematically, $(J_{L/R/X})_{jk} \sim \lambda_j\lambda_k^*/E_C$ and $(J_{Y/Z})_{jk} \sim \lambda_j\lambda_k^* t_{LR}/E_C^2$. Since one can gauge away complex phases of tunneling amplitudes for systems without closed loops, all these cotunneling amplitudes can be chosen real and positive. Within each coupling family, one thus arrives at a real symmetric matrix.

The RG equations then follow from Eqs. (3.15) and (3.16). For $j,k \in \mathcal{B}_L$, one finds

$$\frac{d(J_L)_{jk}}{d\ell} = \sum_{\substack{m\in\mathcal{B}_L \\ m\neq(j,k)}} (J_L)_{jm}(J_L)_{mk} + (J_X)_{lj}(J_X)_{lk} + (J_Y)_{rj}(J_Y)_{rk} + \sum_{m\in\mathcal{B}_R} (J_Z)_{jm}(J_Z)_{mk}. \quad (3.24)$$

Furthermore, with $j \in \mathcal{B}_L$, one obtains

$$\frac{d(J_{X/Y})_{l/r,j}}{d\ell} = \sum_{\substack{m\in\mathcal{B}_L \\ m\neq j}} (J_{X/Y})_{l/r,m}(J_L)_{mj}, \quad (3.25)$$

while for $j \in \mathcal{B}_L$ and $k \in \mathcal{B}_R$,

$$\frac{d(J_Z)_{jk}}{d\ell} = \sum_{\substack{m\in\mathcal{B}_L \\ m\neq j}} (J_L)_{jm}(J_Z)_{mk} + \sum_{\substack{m\in\mathcal{B}_R \\ m\neq k}} (J_Z)_{jm}(J_R)_{mk}. \quad (3.26)$$

The corresponding RG equations for the J_R, $J_{X,r}$ and $J_{Y,l}$ couplings follow by exchanging left/right labels.

The above RG equations can be simplified considerably by observing that different coupling families effectively become isotropic at low energy scales. For small-to-moderate bare anisotropies of the respective coupling matrices, such an isotropisation can already be established within the weak-coupling regime accessible to the RG approach. As shown [Gau, 2018] by a numerical solution of the full RG equations (3.24)–(3.26), the isotropisation mechanism also applies for the two-box device in Fig. 3.3 (with $M_R = 2$). This finding can be rationalised by noting that for any $M \geq 2$, couplings to leads in this sector feed back into the RG flow of each other if they belong to the same family. As a consequence, different coupling families are effectively described by specifying only their mean (average) values, $(J_L)_{jk} \to J_L$ and so on, i.e.

$$J_L = \frac{1}{M_L(M_L-1)} \sum_{j\neq k\in\mathcal{B}_L} (J_L)_{jk}, \qquad J_{X,l} = \frac{1}{M_L} \sum_{k\in\mathcal{B}_L} (J_X)_{lk}$$
$$J_{Y,r} = \frac{1}{M_L} \sum_{k\in\mathcal{B}_L} (J_Y)_{rk}, \qquad J_Z = \frac{1}{M_L M_R} \sum_{j\in\mathcal{B}_L, k\in\mathcal{B}_R} (J_Z)_{jk}. \tag{3.27}$$

Anisotropies within a given coupling family are RG irrelevant and can thus be neglected at low energies. In fact, one expects the above conclusions to apply for general coupled Majorana box systems.

The two-box problem in Fig. 3.3 is then described by seven running couplings, where Eqs. (3.24)–(3.26) yield the isotropised RG equations

$$\begin{aligned} \frac{dJ_L}{d\ell} &= (M_L-2)J_L^2 + M_R J_Z^2 + J_{X,l}^2 + J_{Y,r}^2, \\ \frac{dJ_{X,l}}{d\ell} &= (M_L-1)J_{X,l}J_L, \\ \frac{dJ_{Y,r}}{d\ell} &= (M_R-1)J_{Y,r}J_L, \\ \frac{dJ_Z}{d\ell} &= \left[(M_L-1)J_L + (M_R-1)J_R\right] J_Z, \end{aligned} \tag{3.28}$$

and related equations for J_R, $J_{X,r}$, and $J_{Y,l}$. One can briefly check Eq. (3.28) for two limiting cases:

For vanishing MZM-MZM coupling, $t_{LR} \to 0$, both boxes are decoupled. Thus, one obtains $J_Z = J_{Y,r/l} = 0$, and $\sigma_x = \pm 1$ is conserved. The above equations then reduce to a decoupled pair of single-impurity TKE systems, cf. Eq. (3.13), where $M_L + 1$ and $M_R + 1$ leads are attached to the left/right box: for $t_{LR} = 0$, the central leads l and r in Fig. 3.3 join the respective bosonic subsector $\mathcal{B}_{L/R}$.

In the absence of both central leads, one finds $J_{X,l/r} = J_{Y,r/l} = 0$ and $\sigma_z = \pm$ is conserved. In this case, the RG equations for the single-impurity TKE are again recovered. However, since both boxes are now connected by $t_{LR} \neq 0$, one encounters the equations for a *single* Kondo impurity with $M_L + M_R$ attached leads. At low energies, both boxes are thus fused together by the MZM-MZM link and thereby form a single enlarged Majorana box subsequently exhibiting a global TKE with symmetry group $\mathrm{SO}_2(M_L + M_R)$.

For generic initial values of the isotropised cotunneling amplitudes, the RG equations (3.28) were solved numerically. The analysis shows that the system will flow towards strong coupling with competing separate (intra-box) and global (inter-box) TKEs. This scenario is reminiscent of the classic two-impurity Kondo problem [Jayaprakash, 1981, Jones, 1988, Affleck, 1995] and indicates, that a strong-coupling analysis is needed in order to determine the ground state, see Sec. 3.3.3.

3.2.3 Loop qubit device

As a final example for the RG analysis, the loop qubit device shown in Fig. 3.5 is considered. This device has a single Majorana box containing $M = 2$ leads with simple contacts, and a non-simple contact coupling two MZMs to a central lead (with boson field Φ_c), see Sec. 3.1.2, in particular Eq. (3.7) and Fig. 3.2(b). Importantly, such a device provides the simplest possibility for tunneling paths forming closed loops. It has been suggested as a Majorana qubit realisation [Karzig, 2017], where the relative phase φ_0 between the tunneling amplitudes connecting the central lead with the respective MZM can be changed by a magnetic flux. Note that φ_0 corresponds to the loop phase between different tunneling paths in Eq. (3.20). By contacting the box with leads as shown in Fig. 3.5, non-trivial interferometric conductance measurements can be performed. In particular, a measurement of the linear conductance between the central lead and one of the outer leads ($\Phi_{1,2}$ in Fig. 3.5) could determine the eigenvalue of the Pauli operator σ_z related to the non-conserved fermion parity of the junction [Plugge, 2017, Karzig, 2017].

The non-simple junction is described by $\mathcal{H}_{2,1}$ in Eq. (3.7) with $\Phi \to \Phi_c$ and $h_z \to 0$. A direct MZM-MZM coupling is not included, but MZMs instead hybridise with the fermion density at the central contact, see below. With $\sigma_\pm = (\sigma_x \pm i\sigma_y)/2$, one thus obtains

$$\mathcal{H}_{2,1} = (\lambda_+\sigma_+ + \lambda_-\sigma_-)e^{i(\varphi-\Phi_c)} + \text{h.c.}, \qquad \text{with} \quad \lambda_\pm = \lambda_x \mp i\lambda_y e^{i\varphi_0}, \tag{3.29}$$

where a gauge was used, where φ_0 appears at the σ_y link in Fig. 3.5 and the tunneling amplitudes $\lambda_{x,y}$ are real-valued. Interestingly, for $\varphi_0 = \pi/2$, the same model describes quasi-particle poisoning effects for the TKE [Plugge, 2016a].

As next step, one implements the projection to the ground-state charge of the box, see Sec. 3.1.3. Thus, the Hamiltonian reads $\mathcal{H} = \mathcal{H}_{\text{leads}} + \mathcal{H}_b$. For M leads (labeled by $j \in \mathcal{B}$) with simple contacts to the box, where $M = 2$ in Fig. 3.5, $\mathcal{H}_b$ is given by

$$\begin{aligned}\mathcal{H}_b &= -J \sum_{j,k\in\mathcal{B},j\neq k} \cos(\Phi_j - \Phi_k) - \sum_{j\in\mathcal{B}} \tilde{\Lambda}\sigma_z\Theta'_j - \Lambda_c\sigma_z\Theta'_c \\ &- \frac{1}{\sqrt{2}}\sum_{j\in\mathcal{B}} \left[(L_+\sigma_+ + L_-\sigma_-)e^{i(\Phi_j-\Phi_c)} + \text{h.c.}\right],\end{aligned} \tag{3.30}$$

where isotropic couplings were assumed. With a tunnel coupling $\tilde{\lambda}$ for the simple lead-MZM contacts, the complex-valued cotunneling amplitudes between the central and the outer leads are contained in $L_\pm = \sqrt{2}\tilde{\lambda}\lambda_\pm/E_C$, see Eq. (3.29). In contrast to those, the TKE-like coupling J describes cotunneling between leads within subsector $\mathcal{B}$. Due to the existence of tunneling paths forming closed loops, Eq. (3.30) also contains hybridisation terms of the form in Eq. (3.18). The bare (initial) values for these couplings are $\tilde{\Lambda} = 0$ and $\Lambda_c \simeq (\lambda_x\lambda_y/E_C)\sin\varphi_0$. During the RG flow, both $\tilde{\Lambda}$ and Λ_c grow and approach strong coupling.

Next, one can exploit current conservation, $\langle\Theta'_c\rangle + \sum_j \langle\Theta'_j\rangle = 0$, which follows from gauge invariance under a simultaneous shift of all boson fields $\Phi_{j,c}$. This relation allows to further reduce the number of parameters by trading off hybridisations at the outer leads versus an enhanced hybridisation between the central lead and σ_z. With $\Lambda = 2(\Lambda_c - \tilde{\Lambda})$, one then obtains the RG equations, cf. [Plugge, 2016a],

$$\begin{aligned}\frac{dJ}{d\ell} &= (M-2)J^2 + |L_+|^2 + |L_-|^2, \\ \frac{dL_\pm}{d\ell} &= \left[(M-1)J \pm \Lambda\right] L_\pm,\end{aligned} \tag{3.31}$$

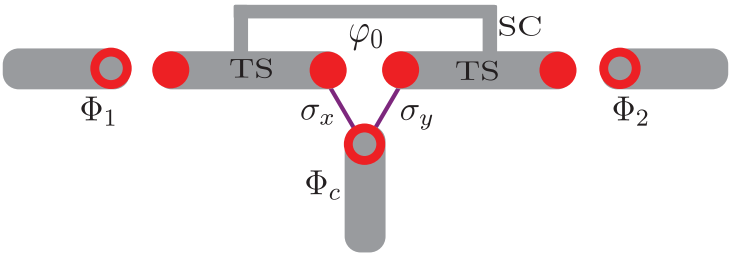

Figure 3.5: Loop qubit device contacted by normal leads. This device has been suggested in [Karzig, 2017] for interferometric Majorana qubit measurements and manipulations. Two long topological superconductor (TS) wires with a superconducting (SC) bridge define a Majorana box with four MZMs, where the loop phase φ_0 can be controlled by a magnetic flux. The normal leads attached to the box correspond to boson fields $\Phi_{1,2,c}$. The central lead (Φ_c) couples to two MZMs as in Fig. 3.3(b), where the non-conserved fermion parity is encoded by Pauli operators $\sigma_{x,y,z}$. [Gau, 2018]

$$\frac{d\Lambda}{d\ell} = (M+1)\left(|L_+|^2 - |L_-|^2\right).$$

The most interesting prediction of these equations is the onset of *helicity* [Plugge, 2016a], i.e. a non-trivial flow of the couplings $L_\pm$. To this end, it is instructive to relate the RG flow of the above couplings with that of the loop phase φ_0. First, one observes that with $\lambda_\pm$ in Eq. (3.29),

$$\begin{aligned} |L_+(\ell)|^2 + |L_-(\ell)|^2 &\sim \lambda_x^2 + \lambda_y^2, \\ |L_+(\ell)|^2 - |L_-(\ell)|^2 &\sim \lambda_x\lambda_y \sin\varphi_0. \end{aligned} \tag{3.32}$$

This implies that while the TKE-like coupling J grows and stays independent of φ_0, the hybridisation Λ, with initial value $\Lambda(\ell = 0) \sim \sin\varphi_0$, keeps the same dependence on φ_0 throughout the RG flow. Moreover, the complex phases of the couplings $L_\pm$ are invariant during the RG flow, since the prefactor for their self-renormalisation in Eq. (3.31) is real. Using $L_\pm \sim \lambda_\pm$, the running loop phase is then defined by

$$\varphi_0(\ell) = \arg\left[i(L_+ - L_-)/(L_+ + L_-)\right]_\ell. \tag{3.33}$$

Note that in general $\varphi_0(\ell)$ will change during the RG flow, because it depends on both the complex phases and the absolute values of $L_\pm$. In particular, for bare loop phases with $\varphi_0(0) \in (0, \pi)$, one finds $|L_+(0)| > |L_-(0)|$. While for $\varphi_0(0) \in (-\pi, 0)$, one instead obtains $|L_-(0)| > |L_+(0)|$. The RG equations (3.31) thus predict a flow of the larger coupling $L_\pm$ to strong coupling, along with growing J and Λ, while the opposite coupling $L_\mp$ is dynamically suppressed.

In [Gau, 2018], typical results for the RG flow of φ_0 obtained by numerical integration of a fully anisotropic version of Eq. (3.31) were shown. The numerical results perfectly recover the qualitative behaviour discussed above. In physical terms, the limiting cases of the RG flow correspond to phase pinning at low energies, with the stable asymptotic value $\varphi_\pm = \pm\pi/2$ as $L_\pm$ outgrows $L_\mp$, cf. Eq. (3.33). These two values correspond to the helical fixed points found in [Plugge, 2016a].

For $\varphi_0 = 0$ or $\varphi_0 = \pi$ the RG flow of the hybridisation, $\Lambda(\ell) \sim \sin\varphi_0(\ell) = 0$, is fully blocked. Here a fundamentally different problem of a single MZM coupled to two leads occurs. For a discussion see [Gau, 2018].

In Sec. 3.3, the strong-coupling limit is discussed. Here the loop qubit will again serve as an example.

3.3 Strong-coupling regime

In Sec. 3.2, it was shown that the systems studied in this chapter will approach the strong-coupling regime. At very low energies, in particular for an understanding of the ground state, one therefore has to go beyond the RG approach. In this section, concepts developed for a strong-coupling solution of the TKE via Abelian bosonisation, cf. Sec. 2.3.4, are extended to the more general setting of Majorana box networks. Such strategies can lead to additional insights, and even allow for analytical solutions in not too complicated setups.

The arguments in Sec. 3.2 imply that for low energies, one needs to keep only isotropic cotunneling amplitudes within and in between subsectors. In fact, if a subsector contains more than one lead, the center-of-mass field will be the only linear combination that is not pinned in the ground state. To access the ground state, one has to study the combined dynamics of these center-of-mass fields and the Pauli operator strings in the system. In this way, the complexity of the problem can be drastically reduced and the physics becomes more transparent, see Sec. 3.3.1. A second key ingredient of the strong-coupling approach is tied to the possibility of decoupling certain linear combinations of boson fields via unitary transformations, see Sec. 3.3.2. This strategy is then illustrated in Sec. 3.3.3 and Sec. 3.3.4 for the two examples discussed from the RG viewpoint in Sec. 3.2.2 and Sec. 3.2.3.

3.3.1 Reduction of bosonic subsectors

The first step in the construction of the strong-coupling theory is the reduction of every bosonic subsector $\mathcal{B}$ to the corresponding center-of-mass field,

$$\phi_0(x,\tau) = g_0 \sum_{j\in\mathcal{B}} \phi_j(x,\tau), \quad g_0 = \frac{1}{\sqrt{M}}, \tag{3.34}$$

where $\Phi_0 = \phi_0(x=0)$. For $M=1$, the field Φ_0 then coincides with the single boson field in the respective subsector (with $g_0 = 1$), but Eq. (3.34) implies a reduction of complexity for $M = |\mathcal{B}| \geq 2$. The usefulness of Eq. (3.34) follows from previous Abelian bosonisation studies of the strong-coupling TKE [Béri, 2017] and the arguments explained in Sec. 3.2. In fact, for $M \geq 2$, couplings within $\mathcal{B}$ grow strong, and for $M \geq 3$ also become isotropic. In detail, one can introduce reduced boson fields, $\tilde{\Phi}_{j\in\mathcal{B}} = \Phi_j - g_0\Phi_0$, with the constraint $\sum_j \tilde{\Phi}_j = 0$. For a discussion of the low-energy physics within a single bosonic subsector $\mathcal{B}$ see Sec. 2.3.4, where the analogy to the quantum Brownian motion of a particle with coordinates $\tilde{\Phi}_j$ in the $(M-1)$-dimensional lattice defined by the potential $\mathcal{H}_{\mathcal{B}}$, cf. Eq. (2.55), was established.

In networks, the main interest does not lie in effects caused by intra-subsector operations, but instead, the question of interest is how different center-of-mass boson fields in a coupled box device interact among themselves and with Pauli string operators. Thus, one can assume that all reduced fields in bosonic subsectors are pinned to their static quasi-classical minima $\tilde{\varphi}_j$, and then express the dynamics of Φ_j in terms of the center-of-mass motion,

$$\Phi_{j\in\mathcal{B}}(\tau) = \tilde{\varphi}_j + g_0\Phi_0(\tau). \tag{3.35}$$

Inserting Eq. (3.35) into Eq. (3.14), for transitions between subsectors $\mathcal{B}_1$ and $\mathcal{B}_2$, one obtains

$$\mathcal{H}_{\mathcal{B}_1,\mathcal{B}_2} = \sum_{j\in\mathcal{B}_1}\sum_{k\in\mathcal{B}_2} J_{jk}^{(\{\sigma\})}\sigma^1\cdots\sigma^n e^{i(\tilde{\varphi}_j-\tilde{\varphi}_k)} e^{i(g_1\Phi_1-g_2\Phi_2)}, \tag{3.36}$$

where $\Phi_{1,2}$ denote the center-of-mass fields for subsectors $\mathcal{B}_{1,2}$, respectively, with $g_{1,2}$ in Eq. (3.34).
Since the relative tunnel phases between leads in each subsector were gauged away, the $J_{jk}^{(\{\sigma\})}$ in Eq. (3.36) are real and positive up to a global inter-sector phase $\varphi_{\mathcal{B}_1\mathcal{B}_2}^{(\{\sigma\})}$. Defining an effective tunneling amplitude between sectors $\mathcal{B}_1$ and $\mathcal{B}_2$ with the corresponding Pauli string $\{\sigma\}$,

$$J_{\mathcal{B}_1\mathcal{B}_2}^{(\{\sigma\})} = e^{i\varphi_{\mathcal{B}_1\mathcal{B}_2}^{(\{\sigma\})}} \sum_{j\in\mathcal{B}_1} \sum_{k\in\mathcal{B}_2} J_{jk}^{(\{\sigma\})} e^{i(\tilde{\varphi}_j - \tilde{\varphi}_k)}, \tag{3.37}$$

the inter-sector cotunneling Hamiltonian is given by

$$\mathcal{H}_{\mathcal{B}_1\mathcal{B}_2} = J_{\mathcal{B}_1\mathcal{B}_2}^{(\{\sigma\})} \sigma^1 \cdots \sigma^n e^{i(g_1\Phi_1 - g_2\Phi_2)} + \text{h.c.}. \tag{3.38}$$

The full strong-coupling tunneling Hamiltonian follows by summing over all subsector pairs. Several comments are now in order:

1. The above discussion also holds if one of the subsectors $\mathcal{B}_{1,2}$ contains just a single lead, where Eq. (3.38) applies as soon as the other subsector enters strong coupling.

2. Phase differences between individual $\tilde{\varphi}_j$ (or $\tilde{\varphi}_k$) in Eq. (3.37) are pinned by the potential terms of the respective subsector, cf. Eq. (2.55). Therefore, also the inter-sector differences $\tilde{\varphi}_j - \tilde{\varphi}_k$ are fixed, and all contributions to $J_{\mathcal{B}_1\mathcal{B}_2}^{(\{\sigma\})}$ in Eq. (3.37) add up with a collective inter-sector phase $\varphi_{\mathcal{B}_1\mathcal{B}_2}^{(\{\sigma\})}$.

3. Equation (3.38) implies a drastic reduction in the number of boson fields at strong coupling. However, the parameter g_0 in Eq. (3.34) implies that the collective fermionic lead obtained from ϕ_0 in general will represent an interacting fermion theory. To see this, note that $\tilde{g} = 1/g_0^2 = M$ acts like a Luttinger liquid parameter [Nayak, 1999, Béri, 2017]. For $M > 1$, thus attractive electron-electron interactions are present.

4. One might encounter multiple tunneling paths with distinct Pauli strings connecting both subsectors, in particular, for systems with closed loops. The strong-coupling Hamiltonian then contains a center-of-mass term as in Eq. (3.38) for each of these non-equivalent tunneling paths. Their relative phase,

   $$\varphi^{\text{loop}} = \varphi_{\mathcal{B}_1\mathcal{B}_2}^{(\{\sigma\})} - \varphi_{\mathcal{B}_1\mathcal{B}_2}^{(\{\sigma'\})}, \tag{3.39}$$

   coincides with the loop phase in Eq. (3.20).

The strong-coupling projection of bosonic subsectors to center-of-mass fields is not limited to a specific setup. In particular, the same idea allows one to elegantly discuss nonequilibrium effects due to applied bias voltages in simply-coupled systems [Béri, 2017]. For the resulting effective models, similar to the discussion in Sec. 3.2.1, the here discussed approach only depends on whether tunneling paths between a pair of subsectors contain overall commuting or anticommuting Pauli strings. For mutually commuting operators, one arrives at RG equations as in Eqs. (3.15) and (3.16). Now one might consider two tunneling operators with couplings $J_{\mathcal{B}_1\mathcal{B}_2}^{(\{\sigma\})}$ and $J_{\mathcal{B}_2\mathcal{B}_3}^{(\{\sigma'\})}$, which connect subsector $\mathcal{B}_2$ with subsectors $\mathcal{B}_1$ and $\mathcal{B}_3$, respectively, cf. Fig. 3.4. If the corresponding Pauli strings anticommute, no RG contributions will be generated for arbitrary couplings $J_{\mathcal{B}_1\mathcal{B}_3}^{(\{\sigma''\})}$ between $\mathcal{B}_1$ and $\mathcal{B}_3$. However, if two (or more) paths between a *pair* of subsectors contain anticommuting Pauli strings, one obtains the hybridisation and feedback contributions discussed in Sec. 3.2.1.

3.3.2 Decoupling fields via hybridisation terms

Another key ingredient concerns a decoupling of certain linear combinations of boson fields from cotunneling operators with Pauli strings. Such strategies go back to the work of Emery and Kivelson (EK) [Emery, 1992] and are often used for Kondo systems, see [Gogolin, 2004, Fabrizio, 1995, Landau, 2017]. In particular, they show that the relevant low-energy degrees of freedom at strong coupling usually differ from those at weak coupling. After an orthogonal rotation of the original set of lead boson fields $\{\phi_j(x)\}$ to a new set of boson fields $\{\phi_\alpha(x)\}$, which corresponds to a highly non-local operation in terms of the underlying fermions, a unitary rotation involving Pauli operators and the boundary phase fields $\Phi_\alpha = \phi_\alpha(0)$ can be performed. One thereby trades off the coupling of some boson species with a Pauli operator in favour of a hybridisation term. These generalised EK decoupling schemes can allow for exact results at special parameter choices (Toulouse points) [Gogolin, 2004], where the bare hybridisation, cf. Sec. 3.2.1, is precisely compensated by the effects of the unitary transformation.

This strategy can be used to decouple relative ('spin') fields in the cotunneling regime of charge-quantised coupled box systems. As an example, one might focus on the single-MZM two-lead junction described by the junction Hamiltonian $\mathcal{H}_{1,2}$ in Eq. (3.8), see Fig. 3.2(c) and Sec. 3.1.2, where the boson fields $\Phi_{x,y}$ refer to the two leads coupled to a single MZM.

First, one switches to linear combinations of the lead bosons, $\phi_{c,s}(x) = (\phi_x(x) \pm \phi_y(x))/\sqrt{2}$, and analogously for the conjugate θ_ν fields. The transformation is written as $\Phi_c = (\Phi_x + \Phi_y)/\sqrt{2}$ and $\Phi_s = (\Phi_x - \Phi_y)/\sqrt{2}$, with the implicit understanding that the transformation is also carried out in the bulk. From Eq. (3.8), one then obtains

$$\mathcal{H}_{1,2} = \left(\lambda_x \sigma_x e^{i\frac{\Phi_s}{\sqrt{2}}} + \lambda_y \sigma_y e^{-i\frac{\Phi_s}{\sqrt{2}}}\right) e^{i\left(\frac{\Phi_c}{\sqrt{2}} - \varphi\right)} + \text{h.c.}, \tag{3.40}$$

where only the Φ_s field couples in an essential manner to the Pauli operators $\sigma_{x,y}$.

At this point, one applies the unitary transformation $U = e^{i\sigma_z \Phi_s/\sqrt{2}}$. Switching to $\sigma_\pm = (\sigma_x \pm i\sigma_y)/2$, the transformed junction Hamiltonian, $\tilde{\mathcal{H}}_{1,2} = U\mathcal{H}_{1,2}U^\dagger$, is given by

$$\tilde{\mathcal{H}}_{1,2} = \left[\lambda_x \left(\sigma_+ + \sigma_- e^{\sqrt{2}i\Phi_s}\right) - i\lambda_y \left(\sigma_- + \sigma_+ e^{-\sqrt{2}i\Phi_s}\right)\right] e^{i\left(\frac{\Phi_c}{\sqrt{2}} - \varphi\right)} + \text{h.c.} \tag{3.41}$$

In addition, transformation of the lead Hamiltonian generates a hybridisation term, which is of the form $(v_F/\sqrt{2})\sigma_z \Theta_s'$. The $\lambda_{x/y}$ terms now contain rapidly oscillating phase exponentials of Φ_s. In the spirit of the rotating wave approximation, one can drop such highly irrelevant tunneling operators. Thereby, the boundary Hamiltonian reduces to

$$\tilde{H}_b = \left(\lambda_x \sigma_+ - i\lambda_y \sigma_-\right) e^{i\left(\frac{\Phi_c}{\sqrt{2}} - \varphi\right)} + \text{h.c.} + \Lambda \sigma_z \Theta_s', \tag{3.42}$$

where Λ includes a bare coupling value and the above $v_F/\sqrt{2}$ term. Thus, the field Φ_s has been decoupled at the cost of an interaction between the lead density $\sim \Theta_s'$ and the Pauli operator σ_z. However, at the special Toulouse point, which is determined by $\Lambda = 0$, the spin-field combination disappears completely.

For a discussion of a similar decoupling strategy applied to a system with near-degenerate box charge states see [Gau, 2018]. In the remainder of this section, see also Sec. 3.4, the above ideas are employed to study the strong-coupling regime for the applications discussed from the weak-coupling RG perspective in Sec. 3.2.2 and Sec. 3.2.3.

3.3.3 Two tetron device

For the two-box device in Fig. 3.3, according to the strategy in Sec. 3.3.1, one first identifies the important boson fields that should be kept in the strong-coupling analysis. There are four such fields, namely the center-of-mass fields for the left/right box, $\Phi_{L/R}$, with $g_{L/R} = 1/\sqrt{M_{L/R}}$ in Eq. (3.34), and the left/right central lead fields, $\Phi_{l/r}$, with $g_{l/r} = 1$. Hence, five different inter-sector couplings remain: J_Z, $J_{X,l/r}$, and $J_{Y,r/l}$. Since those effective couplings are obtained by summing over individual leads, they include enhancement factors $\sim M_{L,R}$, cf. Sec. 3.3.1. From the cotunneling Hamiltonian in Eqs. (3.22) and (3.23), the effective strong-coupling theory follows as

$$\mathcal{H}_{\text{eff}} = \sum_{\nu=L,R,l,r} \mathcal{H}_{\text{leads}}[\phi_\nu, \theta_\nu] - \frac{1}{2}\left(\Gamma_b + \Gamma_b^\dagger\right), \tag{3.43}$$

with the boundary operator

$$\begin{aligned} \Gamma_b &= J_{X,l}\sigma_x e^{i(\Phi_l - g_L\Phi_L)} + J_{X,r}\sigma_x e^{i(\Phi_r - g_R\Phi_R)} + J_{Y,l}\sigma_y e^{i(\Phi_l - g_R\Phi_R)} \\ &+ J_{Y,r}\sigma_y e^{i(\Phi_r - g_L\Phi_L)} + iJ_Z\sigma_z e^{i(g_L\Phi_L - g_R\Phi_R)}. \end{aligned} \tag{3.44}$$

For arbitrary device parameters, further analytical progress is difficult even though at least one of the charge/spin combinations of the central lead fields, $\Phi_{c,s} = (\Phi_l \pm \Phi_r)/\sqrt{2}$, can be decoupled by an EK transformation, see Sec. 3.3.1. For instance, when studying transport between L/R leads, a decoupling of Φ_s is most sensible. In any case, numerical approaches can provide another option to investigate the physics encoded by Eq. (3.44). Instead, the focus lies on a simpler yet non-trivial two-box setup, which does allow for analytical progress. Such a device is shown in Fig. 3.1, where in contrast to the case depicted in Fig. 3.3, one only has a single central lead (Φ_l). The strong-coupling Hamiltonian for this device follows directly from Eqs. (3.43) and (3.44) by putting $J_{X/Y,r} = 0$. The remaining couplings are given by

$$J_x = J_{X,l}, \quad J_y = J_{Y,l}, \quad J_z = J_Z. \tag{3.45}$$

One then performs an EK transformation with $U = e^{i\sigma_z(\Phi_l - g_R\Phi_R)}$. Following the steps in Sec. 3.3.1, the transformed Hamiltonian, $\tilde{\mathcal{H}}_{\text{eff}} = \mathcal{H}_{\text{leads}} + \tilde{\mathcal{H}}_b$, contains the boundary term

$$\begin{aligned} \tilde{\mathcal{H}}_b &= -\frac{1}{2}\left(\tilde{\Gamma}_b + \tilde{\Gamma}_b^\dagger\right) + \Lambda\sigma_z\left(\Theta_l' - g_R\Theta_R'\right), \\ \tilde{\Gamma}_b &= (J_x\sigma_+ - iJ_z\sigma_z)e^{-i(g_L\Phi_L - g_R\Phi_R)} - iJ_y\sigma_+. \end{aligned} \tag{3.46}$$

The hybridisation parameter $\Lambda = \Lambda_0 - v_F$ includes a bare coupling Λ_0, where v_F is due to the EK transformation of $\mathcal{H}_{\text{leads}}$. Next, one performs an orthogonal rotation of the $\phi_{L/R}(x)$ phase fields,

$$\begin{pmatrix} \phi_1 \\ \phi_2 \end{pmatrix} = \frac{1}{\bar{g}}\begin{pmatrix} g_L & -g_R \\ g_R & g_L \end{pmatrix}\begin{pmatrix} \phi_L \\ \phi_R \end{pmatrix}, \quad \bar{g} = \sqrt{g_L^2 + g_R^2}, \tag{3.47}$$

resulting in

$$\tilde{\mathcal{H}}_b = -\frac{1}{2}\left((J_x\sigma_+ - iJ_z\sigma_z)e^{-i\bar{g}\Phi_1} + \text{h.c.} + J_y\sigma_y\right) + \frac{\Lambda}{\bar{g}}\sigma_z\left(\bar{g}\Theta_l' + g_R^2\Theta_1' + g_Rg_L\Theta_2'\right). \tag{3.48}$$

The setup with $M_L = M_R = 2$ in Fig. 3.1 now gives access to an exact solution at the Toulouse point, $\Lambda = 0$, via the refermionisation approach [Gogolin, 2004]. Indeed, for

$\bar{g} = 1$, which only holds for $M_L = M_R = 2$, the operator $e^{-i\bar{g}\Phi_1}$ in Eq. (3.48) can be expressed as fermion annihilation operator (up to a Klein factor), and $\tilde{\mathcal{H}}_{\text{eff}}$ thus reduces to a non-interacting fermion theory for $\Lambda = 0$. In the remainder of this subsection, $M_L = M_R = 2$ are assumed, but for now still allow for $\Lambda \neq 0$.
At this stage, one can employ Eq. (2.41) backwards to obtain chiral fermion operators $\psi_\nu(x)$ associated with the respective boson field ϕ_ν, where the mode index is given by$\nu = 1, 2, l$. Using $\Psi_\nu = \psi_\nu(0)$ and recalling that $\Psi_\nu^\dagger \sim \kappa_\nu e^{i\Phi_\nu}$, see Eq. (2.41), Klein factors (κ_ν) are again represented as Majorana operators. In addition, one expresses Pauli operators as Majorana bilinears, $\sigma_{\alpha=x,y,z} = i\gamma_\alpha\gamma_0$, with the overall parity constraint $\gamma_0\gamma_x\gamma_y\gamma_z = 1$. Noticing that $\kappa_{\nu=1}$ is the only Klein factor which explicitly appears in $\tilde{\mathcal{H}}_{\text{eff}}$, and that $i\gamma_0\kappa_1 = \pm 1$ is conserved, $i\gamma_0\kappa_1 = -1$ can be chosen. Hence, Eq. (3.48) yields

$$\begin{aligned}\tilde{\mathcal{H}}_b &= J_x\gamma_x\left(\Psi_1^\dagger - \Psi_1\right) + i\left(J_x\gamma_y - J_z\gamma_z\right)\left(\Psi_1^\dagger + \Psi_1\right)\\ &- \frac{iJ_y}{2}\gamma_z\gamma_x + i\Lambda\gamma_y\gamma_x : 2\Psi_l^\dagger\Psi_l + \Psi_1^\dagger\Psi_1 - \Psi_2^\dagger\Psi_2 :,\end{aligned} \tag{3.49}$$

where : : indicates normal-ordering and $1/\sqrt{\alpha}$ factors from the short-distance cutoff in Eq. (2.41) have been absorbed in $J_{x,z}$. In the Toulouse limit, one indeed has non-interacting fermions. In the final step, one switches to chiral MFs by writing

$$\psi_\nu(x) = \left[\xi_\nu(x) + i\eta_\nu(x)\right]/\sqrt{2}, \tag{3.50}$$

where $\xi_\nu(x) = \xi_\nu^\dagger(x)$ and $\eta_\nu(x) = \eta_\nu^\dagger(x)$ obey the algebra $\{\xi_\nu(x), \eta_{\nu'}(x')\} = \delta(x - x')\delta_{\nu\nu'}$. The bulk Hamiltonian then takes the form

$$\mathcal{H}_{\text{leads}} = -\frac{iv_F}{2}\sum_\nu \int_{-\infty}^{\infty} dx\left(\xi_\nu\partial_x\xi_\nu + \eta_\nu\partial_x\eta_\nu\right), \tag{3.51}$$

and the Toulouse Hamiltonian is given by

$$\mathcal{H}_{\text{Toul}} = \mathcal{H}_{\text{leads}} - i\sqrt{2}J_x\gamma_x\eta_1(0) + i\sqrt{2}(J_x\gamma_y - J_z\gamma_z)\xi_1(0) - \frac{iJ_y}{2}\gamma_z\gamma_x. \tag{3.52}$$

Interaction corrections to the above Toulouse Hamiltonian are discussed in [Gau, 2018]. Finally, noting that $\Psi_1 \sim e^{-i\Phi_1} = e^{-i(\Phi_L - \Phi_R)/\sqrt{2}}$, one observes that the central lead (Ψ_l) decouples at the Toulouse point, i.e. no current will flow through this lead. A detailed discussion of nonequilibrium transport for this setup is given in Sec. 3.4.

3.3.4 Loop qubit device

As a last example, the strong-coupling regime of the loop qubit device depicted in Fig. 3.5 is discussed. While a limiting case of the problem, cf. Eq. (3.53) below, has already been addressed in [Plugge, 2016a], in view of the experimental interest in this device, [Gau, 2018] provides a more complete picture. Following the strategy in Sec. 3.3.1, one first defines a center-of-mass field for the M outer leads, $\Phi_L = g_L\sum_{j=1}^{M}\Phi_j$ with $g_L = 1/\sqrt{M}$. Also recall that Φ_c denotes the boson field for the central lead contacting two MZMs on the box, see Fig. 3.5. The weak-coupling analysis in Sec. 3.2.3 has identified two qualitatively different candidate strong-coupling fixed points.
The first type is stable and describes an RG flow towards loop phase $\varphi_0 = \pm\pi/2$. Without loss of generality, one might choose $\varphi_0 = +\pi/2$, where the complex-valued cotunneling

amplitude L_+ is dominant and the amplitude L_- vanishes, cf. Eq. (3.30). One then obtains the strong-coupling theory, $\mathcal{H}_{\text{eff}} = \mathcal{H}_{\text{leads}} + \mathcal{H}_{\varphi_0=\pi/2}$, with

$$\mathcal{H}_{\varphi_0=\pi/2} = -J_+\sigma_+ e^{i(g_L\Phi_L-\Phi_c)} + \text{h.c.} + \Lambda\sigma_z\Theta_c', \tag{3.53}$$

where $J_+ = ML_+/\sqrt{2}$ and $\Lambda = 2(\Lambda_c - \tilde{\Lambda})$, see Sec. 3.2.3. For $M = 1$, [Plugge, 2016a] found that this model can be mapped onto a fully anisotropic single-channel Kondo model. For $M \geq 2$, the central lead Φ_c instead dynamically decouples from the outer leads which in turn develop a TKE for $M \geq 3$.

The second fixed point, taken as $\varphi_0 = 0$ without loss of generality, is unstable with respect to phase variations $\delta\varphi_0$, see [Gau, 2018]. This fixed point is qualitatively different from the first one, as it implies $L_+ = L_-$ and $\Lambda \sim \sin\varphi_0 = 0$. The strong-coupling theory follows from Eqs. (3.29) and (3.30),

$$\mathcal{H}_{\varphi_0=0} = -(J_x\sigma_x + J_y\sigma_y)e^{i(g_L\Phi_L-\Phi_c)} + \text{h.c.} \tag{3.54}$$

with $J_{x,y} \sim \lambda_{x,y}$ in Eq. (3.29). Next, the local fermion parity representation of Pauli operators, $\sigma_{x,y} = i\gamma_{x,y}\kappa$, can be used. Since both J_x and J_y are real, with fixed ratio during the RG flow, one can construct a new Majorana operator

$$\gamma = (J_x\gamma_x + J_y\gamma_y)/J, \quad J = \sqrt{J_x^2 + J_y^2}. \tag{3.55}$$

The central contact thus couples to a single Majorana operator γ only, since the relative tunneling phase between the lead and the two original MZMs is zero (or π). For other values of φ_0, such a reduction is not possible. However, the above reasoning is not restricted to the cotunneling regime. The same steps also apply for the tunneling Hamiltonian in Eq. (3.29), and hence one expects this effect to always appear so long as $\varphi_0 = 0 \bmod \pi$. Finally, note that Eq. (3.54) has conserved fermion parity $i\gamma\kappa = \pm 1$. Choosing $i\gamma\kappa = 1$, one obtains

$$\mathcal{H}_{\varphi_0=0} = -2J\cos(g_L\Phi_L - \Phi_c). \tag{3.56}$$

Using the results of [Béri, 2017], where Eq. (3.56) also appears, the full nonequilibrium transport characteristics between the central lead and an arbitrary number $M \geq 2$ of outer leads are accessible.

The loop qubit device in Fig. 3.5 is likely most relevant as a starting point to more complicated Majorana multi-junctions and networks. To guide such experimental tests, it is expedient to summarise how quantum transport is expected to depend on the loop phase φ_0. Since experiments are performed at small but finite temperature and bias, features of the unstable fixed point should appear in a region around $\varphi_0 = 0 \bmod \pi$ with small but non-zero hybridisation. When considering the case $M = 1$. If $\varphi_0 \approx 0$, the here discussed theory predicts qualitatively the same behaviour as for a two-terminal mesoscopic Majorana wire [Hützen, 2012]. While transport for half-integer n_g, i.e. at a charge-degeneracy point, exhibits the quantised zero-temperature conductance $G_0 = e^2/h$, transport in the cotunneling regime will be strongly suppressed. Conversely, as φ_0 is increased, the conductance should approach G_0 largely independent of n_g. Here, tunneling of charges is not due to charge-degenerate states but rather caused by a Kondo resonance [Plugge, 2016a]. The latter arises due to many-body screening of the spin-$1/2$ impurity $\sim (\sigma_x, \sigma_y, \sigma_z)$ built from three Majorana operators, two at the central and one at the simply-coupled lead. Next, the case $M \geq 2$ is considered, i.e. a multi-terminal measurement of conductance between the central lead and outer leads in Fig. 3.5. Starting again with $\varphi_0 \approx 0$, the device should display the transport behaviour expected for the

TKE, cf. Sec. 2.3.4, with fractional conductance values at zero temperature and non-Fermi liquid power laws in the temperature- and/or voltage-dependent conductance. In the loop qubit device, experiments typically include probing the finite-bias conductance through the central lead, which, for $\varphi_0 \approx 0$, should reveal the features discussed in [Béri, 2017]. For increasing φ_0, the ensuing hybridisation Λ at the central (and all other) leads will gap out the MF pair involved in $\sigma_z = i\gamma_y\gamma_x$. As a consequence, transport involving the central lead will be blocked at temperatures and/or voltages below the Kondo temperature T_K of the box. Thus, one predicts drastically different low-energy conductance behaviour depending on both the loop phase φ_0 and the number of attached leads.

3.4 Transport in a two tetron device

In this section, nonequilibrium transport properties for the two-box device in Fig. 3.1 are studied by employing the strong-coupling theory in Sec. 3.3.3. The system is considered at the Toulouse point, with the non-interacting Hamiltonian $\mathcal{H}_{\mathrm{Toul}}$ in Eq. (3.52). The resulting physics is expected to be generic since interaction corrections around the Toulouse point are RG irrelevant [Gau, 2018]. For closely related models, an exact solution for the full counting statistics of charge transport has been described in [Gogolin, 2006] and [Landau, 2017]. In the following, those results are adapted to the setup in Fig. 3.1.

To that end, one can first recall that at the Toulouse point, the central lead ψ_l will dynamically decouple from the transport problem, see Sec. 3.3.3.Thus, the focus lies on a transport configuration, where the $M_L = 2$ ($M_R = 2$) leads attached via simple contacts to the left (right) box are held at chemical potential $+eV/2$ ($-eV/2$). In particular, there are no voltages applied between leads attached to the same box. If the latter were present, quick equilibration of leads at each box is expected due to the large intra-sector coupling. On the contrary, the inter-box coupling may be small and equilibration is perturbed by the central non-simple junction. One then considers the outcome of a two-terminal measurement of the fluctuating time-dependent current, $I(t)$, flowing between individual pairs of leads on different sides. During a measurement time t_m, the charge $q = \int_0^{t_m} dt' I(t')$ is transferred between the two leads, where the full counting statistics of q follows from a cumulant generating function $\chi(\lambda)$. In particular, by taking derivatives with respect to the counting field λ, all cumulants can be obtained from the relation $\langle \delta^n q\rangle = (-i)^n \partial_\lambda^n \ln \chi(\lambda = 0)$. Below, only the average current I, and the current noise S, are discussed. They are given by

$$I = \frac{e}{t_m}\left\langle \delta q\right\rangle, \quad S = \frac{2e^2}{t_m}\left\langle \delta^2 q\right\rangle. \tag{3.57}$$

Next, one relates the transport between individual leads attached to the left and right box, respectively, to the transformed fermion basis at strong coupling, cf. Sec. 3.3.3. To this end, note that the application of the operator $\Psi_1 \sim e^{-i(\Phi_L - \Phi_R)/\sqrt{2}}$ on an arbitrary system state amounts to transporting one unit of charge between the left and right side. Per tunneling event, the charge transferred at each individual lead reads $e^* = e/2$. Thus, one can include the counting field by letting $\Psi_1 \to e^{+(-)i\lambda/4}\Psi_1$ on the forward (backward) time branch of the Keldysh partition function for $\mathcal{H}_{\mathrm{Toul}}$ [Gogolin, 2006]. Since the projected theory in Eq. (3.52) contains only Ψ_1, the inclusion of a counting field is relevant only for one out of the four fermion species in the ensuing two-channel Kondo model [Landau, 2017].

Following [Gogolin, 2006, Landau, 2017], where only the Green's functions for the three impurity-Majorana operators $\gamma_{x,y,z}$ in Eq. (3.52) have to be updated, one obtains the zero-temperature generating function,

$$\ln \chi(\lambda) = \frac{t_m}{2\pi} \int_0^{eV/2} d\omega \ln\left(1 + \mathcal{T}(\omega)[e^{i\lambda} - 1]\right), \tag{3.58}$$

with the frequency-dependent transparency

$$\mathcal{T}(\omega) = \frac{\left(\Gamma_z \omega^2 - \Gamma_x J_y^2\right)^2}{(\Gamma_x^2 + \omega^2)\left[(\omega^2 - J_y^2)^2 + \omega^2(\Gamma_x + \Gamma_z)^2\right]}. \tag{3.59}$$

Here, the energy scales $\Gamma_{x,z} \sim J_{x,z}^2$ are defined, where the proportionality constant also takes into account the rescaling of $J_{x,z}$ due to the short-distance cutoff in Eq. (2.41), see Sec. 3.3.3.

Since the Toulouse Hamiltonian in Eq. (3.52) contains not only different transport mechanisms between left and right leads but also a Majorana hybridisation, multiple scenarios are possible depending on $J_{x,y,z}$. First, the predictions of Eq. (3.58) for the current-voltage characteristics and for shot noise in this system for $J_y = 0$ are discussed. Afterwards, Sec. 3.4.2 extends the discussion to the case of a finite Majorana hybridisation, i.e. $J_y \neq 0$.

3.4.1 No Majorana hybridisation

Starting with the case $J_y = 0$, where the MZM operators γ_x and γ_z are not hybridised, one can define the channel hybridisations

$$\Gamma_1 = \Gamma_x, \quad \Gamma_2 = \Gamma_x + \Gamma_z \tag{3.60}$$

such that Eq. (3.59) takes the simpler form

$$\mathcal{T}_{J_y=0}(\omega) = \frac{(\Gamma_1 - \Gamma_2)^2 \omega^2}{(\omega^2 + \Gamma_1^2)(\omega^2 + \Gamma_2^2)}. \tag{3.61}$$

Equation (3.61) gives the transparency of two competing Majorana channels coupled by the respective channel hybridisation $\Gamma_{1,2}$ to a single impurity, and therefore describes the asymmetric two-channel Kondo effect [Fabrizio, 1995, Landau, 2017]. The current-voltage characteristics readily follow from Eqs. (3.57)–(3.61),

$$I = \frac{e}{h}\frac{\Gamma_2 - \Gamma_1}{\Gamma_2 + \Gamma_1}\left[\Gamma_2 \tan^{-1}\left(\frac{eV}{2\Gamma_2}\right) - \Gamma_1 \tan^{-1}\left(\frac{eV}{2\Gamma_1}\right)\right]. \tag{3.62}$$

It is instructive to consider several limiting cases of Eq. (3.62).

First, the current (3.62) between the left and the right side vanishes identically for the channel-symmetric case with $\Gamma_2 - \Gamma_1 = \Gamma_z \to 0$. In fact, this result is plausible, because the dependence of Γ_z on the microscopic tunnel amplitudes implies that both boxes are decoupled in that limit, i.e. $\sqrt{\Gamma_z} \sim J_z \sim \lambda_L \lambda_R t_{LR}/E_C^2 \to 0$.

Second, a related observation is that by increasing Γ_x at a fixed value of Γ_z, the current in Eq. (3.62) will also decrease. Indeed, for $\Gamma_x/\Gamma_z \to \infty$, Eq. (3.60) implies that one effectively revisits the limit $\Gamma_1 = \Gamma_2$, where the current vanishes. Note that in order to increase $\sqrt{\Gamma_x} \sim J_x \sim \lambda_L \lambda_l / E_C$ at fixed Γ_z, the tunnel coupling λ_l between the left box and the central lead has to be increased. Although charge transfer at the central contact is dynamically blocked, the coupling Γ_x still has profound effects on the system. In particular, for $\Gamma_x \neq 0$, the central junction is effectively driven out of resonance by a

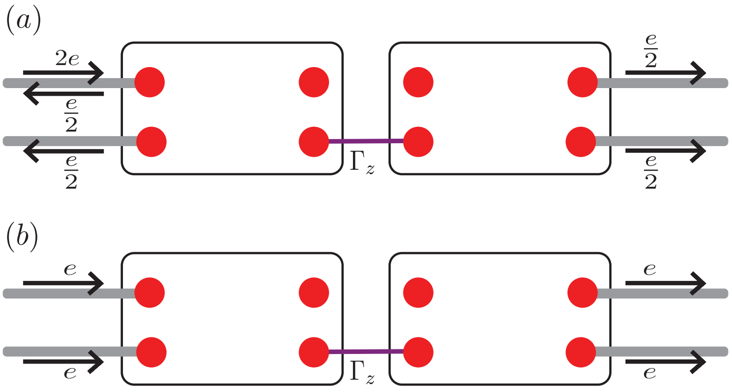

Figure 3.6: Cross-correlated Andreev reflections (AR) generated from individual correlated AR processes in the two-box device with $J_y = 0$ and $\Gamma_x \to 0$, see Sec. 3.4.1. (a) A single AR at the top left lead, followed by the emission of charge $e/2$ into all four leads, forms a correlated AR process as in the TKE, cf. Sec. 2.3.4. (b) A sequence of two correlated ARs, one each at top and bottom left leads, comprises a cross-correlated AR. This allows for the cotunneling of a Cooper pair by subsequent crossed ARs between left (in) and right (out) leads. [Gau, 2018]

misalignment of the spin direction $\sim (\sigma_x, \sigma_y, \sigma_z)$ with respect to the left-right transport direction $\sim \Gamma_z$.

Finally, in the opposite limit $\Gamma_x/\Gamma_z \to 0$, one instead approaches the single-channel case with transparency

$$\mathcal{T}_{\Gamma_x = J_y = 0}(\omega) = \frac{\Gamma_z^2}{\omega^2 + \Gamma_z^2}, \tag{3.63}$$

where $\Gamma_1 = \Gamma_x = 0$ in Eq. (3.60) implies $\Gamma_2 = \Gamma_z$.

For $(eV, \Gamma_x) \ll \Gamma_z$ the transport observables are obtained from Eq. (3.57)

$$\begin{aligned} I &= \frac{e}{2h}\left[eV - 2\Gamma_x \tan^{-1}\left(\frac{eV}{2\Gamma_x}\right)\right], \\ S &= \frac{2e^2}{h}\left[\frac{\Gamma_x}{2}\tan^{-1}\left(\frac{eV}{2\Gamma_x}\right) - \frac{\Gamma_x^2}{(eV)^2 + 4\Gamma_x^2}eV\right]. \end{aligned} \tag{3.64}$$

Defining the backscattered current $I_b = (e^2/2h)V - I$, one observes that for $\Gamma_x \ll eV \ll \Gamma_z$, the shot noise power is given by $S = 2e^* I_b$ with elementary charge $e^* = e/2$. The shot noise comes from the weakly coupled (Γ_1) channel, while the strongly coupled (Γ_2) channel is fully transmitted (with the two-channel Kondo value of the conductance, $G = e^2/2h$) and thus noiseless. Equation (3.64) yields the same fractional Fano factor, $F = S/2I_b = e^*/e = 1/2$, as recently found in a related two-channel charge Kondo system [Landau, 2017]. In the here discussed case, a single additional Majorana operator enters the low-energy theory for $\Gamma_x > 0$, given by the Klein factor κ_l at the central lead, see Fig. 3.1. In Eq. (3.52), it is represented by the Majorana operator γ_x. This causes the backscattering processes in Eq. (3.64), described by the fractional charge $e^* = e/2$.

For $\Gamma_x \to 0$, one also can draw an interesting link to the single-impurity TKE. Indeed, since the left and right boxes are now joined by a strong coupling Γ_z, this two-box setup should be related to the TKE for a single large box with $M = M_L + M_R = 4$ attached leads, cf. Sec. 3.2.2. For the two-terminal conductance measurement in Eq. (3.64), one finds $G_{jk} = e^2/2h$ between any pair of individual leads j and k. Instead, for collective inter-sector transport, [Gau, 2018] shows that the left-right conductance is given by $G_{LR} =$

$2e^2/h$. The latter arises by summing the current over all leads in the respective subsectors, and it comprises cross-correlated Andreev reflections involving the Cooper pair charge $e^*_{LR} = 2e$. The generation of these processes is detailed in Fig. 3.6. Thus, one can predict the appearance of different effective charges due to hybridisation with the central lead ($e^* = e/2$) and finite-energy corrections in collective left-right inter-sector transport ($e^*_{LR} = 2e$).

3.4.2 Finite Majorana hybridisation

Next, one can include the effects of a finite Majorana hybridisation $J_y \neq 0$. In order to obtain a qualitative understanding, the limit $J_y \gg \max(\Gamma_{x,z}, eV)$ is analysed first, where the impurity term $-i(J_y/2)\gamma_z\gamma_x$ in $\mathcal{H}_{\text{Toul}}$ implies the fixed parity $i\gamma_z\gamma_x = +1$. Eq. (3.52) can therefore be projected to a simpler single-channel model, $\mathcal{H}'_{\text{Toul}} = \mathcal{H}_{\text{leads}} + i\sqrt{2}J_x\gamma_y\xi_1(0)$, where a single MZM ($\gamma_y$) is coupled to a single chiral Majorana mode (ξ_1). The parity constraint $i\gamma_z\gamma_x = +1$ here effectively blocks the other chiral Majorana channel $\sim \eta_1$. Indeed, for $J_y \to \infty$, the general transparency expression in Eq. (3.59) reduces to the single-channel result

$$\mathcal{T}_{J_y\to\infty}(\omega) = \frac{\Gamma_x^2}{\omega^2 + \Gamma_x^2}, \tag{3.65}$$

but with active channel $\sim \Gamma_x$ instead of Γ_z in Eq. (3.63). Thus, the single-channel results for conductance and shot noise are obtained, with Γ_x as the only remaining parameter. Left-right transport then takes place exclusively by cotunneling via the central lead l in Fig. 3.3.

Next, one can discuss the voltage dependence of the nonlinear conductance $G = I/V$, which is plotted for typical parameters in Fig. 3.7. The shown curves have been obtained by numerical evaluation of Eqs. (3.57)–(3.59). First, the conductance for $\Gamma_1 = J_y = 0$ (black solid curve) illustrates the single-channel case in Sec. 3.4.1, where Eq. (3.64) gives $G = e^2/2h$ for $eV \ll \Gamma_2$, in accordance with Fig. 3.7. Second, turning to $\Gamma_1 \ll \Gamma_2$ but still keeping $J_y = 0$ (dashed green curve, with $\Gamma_1/\Gamma_2 = 0.001$), one observes that the conductance vanishes for very low voltages but recovers to a large value near $e^2/2h$ within the interval $\Gamma_1 \ll eV \ll \Gamma_2$. Such a behaviour is consistent with the analytical result in Eq. (3.62), which describes the asymmetric two-channel Kondo effect with two competing Majorana channels coupled to an impurity.

The remaining two curves in Fig. 3.7 include the effects of a finite Majorana hybridisation J_y, which now can cause antiresonances or resonances in the voltage dependence of the conductance. First, for $J_y \gg \max(\Gamma_{1,2}, eV)$, cf. the red dash-dotted curve for $\Gamma_1/\Gamma_2 = 0.001$ and $J_y/\Gamma_2 = 100$, two of the three impurity-Majorana operators $\gamma_{x,y,z}$ are gapped out by the large J_y. One thus observes single-channel physics of the weaker channel, with coupling $\Gamma_1 = \Gamma_x$ in Eq. (3.65). Next, for $\Gamma_1 \ll J_y \ll \Gamma_2$ (blue dotted curve, $\Gamma_1/\Gamma_2 = 0.001$ and $J_y/\Gamma_2 = 0.1$), after approaching the single-channel value at $eV \simeq \Gamma_2$, the voltage dependence of the conductance reveals an antiresonance for $\Gamma_1 \lesssim eV \lesssim J_y$ with subsequent recovery at $eV \lesssim \Gamma_1$. Here, in the low-bias regime, a combined channel as in Eq. (3.65) is activated. Finally, for general non-zero couplings $\Gamma_{1,2}$ and J_y, one observes a complex interplay between the asymmetric two-channel Kondo effect and impurity hybridisation phenomena. However, for the here discussed case with three coupled impurity-Majorana operators, the low-frequency transparency in Eq. (3.59) always approaches the unitary limit, $\mathcal{T}(\omega \to 0) = 1$. This behaviour can be rationalised by noting that at sufficiently low energies, one (rotated) Majorana pair will effectively be gapped out for $J_y \neq 0$. The third Majorana operator then remains free. This MZM provides a single-channel transport

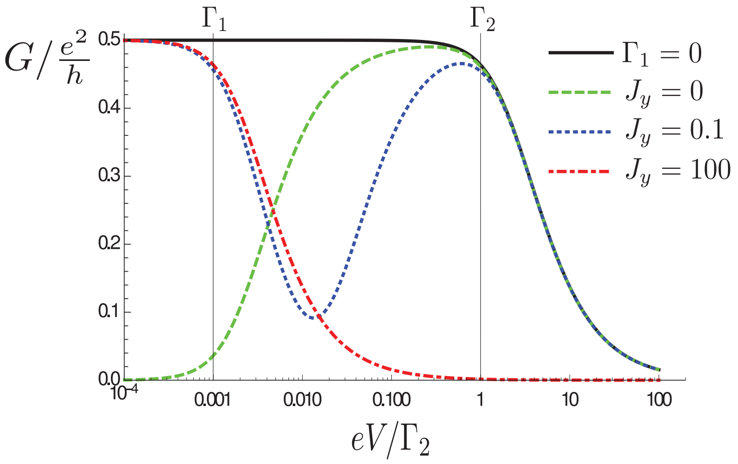

Figure 3.7: Two-terminal conductance $G = I/V$ vs voltage V between two leads attached to different boxes in the two-box device of Fig. 3.1. The shown results hold at the Toulouse point, see Eq. (3.52), and follow from Eqs. (3.57)–(3.59). [Gau, 2018]

resonance pinned to the Fermi level, with the universal zero-bias conductance $G = e^2/2h$.

3.5 Summary

In this chapter quantum transport through coupled Majorana box devices was studied. Since Majorana boxes represent an attractive platform for realising topological qubits, coupled box devices are of current interest for quantum information processing applications, see Sec. 2.4. When normal leads are tunnel-coupled to such a system, the spin-1/2 degrees of freedom representing MBQs will be subject to Kondo screening via cotunneling processes, culminating in the topological Kondo effect. Consequently, when different boxes are connected, one encounters competing Kondo effects and related phenomena.

For general systems of this type, a powerful and versatile theoretical framework for studying the low-energy physics and quantum transport was introduced, cf. Sec. 3.2. The discussed theory employs Abelian bosonisation of the lead fermions together with the Majorana-Klein fusion method. For a single box, the resulting problem is purely bosonic and admits an asymptotically exact solution for the corresponding non-Fermi liquid fixed point. However, for coupled-box systems additional local sets of Pauli operators due to non-conserved local fermion parities must be taken into account. Despite the complexity of the resulting problem, it is possible to make analytical progress. Approaching the physics from the weak-coupling side (see Sec. 3.2) and further analysing it in the strong-coupling regime (see the effective low-energy theory for the most relevant collective degrees of freedom in Sec. 3.3), a rich interplay between different types of single- or multi-box topological Kondo effects has been encountered.

The transport characteristics of two basic devices, where non-conserved fermion parities play a central role, were addressed in Sec. 3.3. One of these includes the loop qubit device suggested in [Karzig, 2017]. Importantly, the methods put forward in this work also allow one to obtain non-perturbative transport results in moderately complex setups, cf. Sec. 3.4. This aspect should be especially valuable in view of the fact that transport measurements could give clear and unambiguous nonlocality signatures for Majorana states in such devices.

Chapter 4

Driven dissipative Majorana boxes

In this chapter, driven dissipative (DD) Majorana platforms are introduced, which allow for the stabilisation and manipulation of robust quantum states. The proposed DD Majorana-based platforms rely on the constructive interplay of topological protection mechanisms and the autonomous quantum error correction capabilities of engineered driven dissipative systems, see also [Diehl, 2008] and[Diehl, 2011]. Thereby, one can engineer systems stabilising Majorana states for an indefinite time. Once a working Majorana platform becomes available, only standard hardware requirements are needed to implement the here discussed ideas.
In order to address state stabilisation in DD Majorana devices, Sec. 4.1 introduces the model of a Majorana box, cf. Sec. 2.2.1, in the presence of environmental electromagnetic noise and with tunnel couplings to quantum dots. For general single-box setups this section shows that the time evolution of the Majorana sector is governed by a Lindblad master equation over a wide parameter range, cf. Sec. 2.5. In Sec. 4.2 this Lindbladian is then studied intensively by using the techniques summarised in Sec. 2.5. As the DD Majorana box allows for the stabilisation of arbitrary single qubit states, Sec. 4.2 starts with the discussion of Pauli eigenstates. The robustness of the DD protocol is then emphasised by targeting a magic state, [Nielsen, 2010], and by discussing the effects of temperature and a small Majorana hybridisation. Interestingly, in some cases such a hybridisation does not lead to an additional dephasing mechanism, which is not the case for the native MBQ in Sec. 2.3. Nevertheless, one can use read-out mechanisms and state initialisation protocols of the native MBQ, making the single DD Majorana box an effectively self-correcting quantum memory. For the purpose of quantum computation, it is beneficial to stabilise a degenerate manifold of dark states, a dark space. Here, Sec. 4.3 provides the physical ingredients to formulate a Lindbladian for a two-box setup allowing for space stabilisation. Moreover, this section includes the stabilisation of maximally entangled states, where the stabilisation protocol can also be used to initialise a specific state within the dark space. Sec. 4.3 also provides details on an alternative architecture, which allows for Bell state stabilisation on very short time scales. Finally, Sec. 4.4 contains the discussion of the dark space stabilisation, where the obtained dark space is equivalent to a qubit space. Since initialisation, read-out, and manipulation of the quantum information stored in the stabilised dark space are discussed in Sec. 4.4, one might view this section as first step towards autonomously error correcting Majorana devices. In Sec. 4.5, the shown results are summarised.

This chapter is essentially a reproduction of the included publications, [Gau, 2020a] and [Gau, 2020b], where the pedagogical nature of this thesis allows for some additional results, which are not present in the publications.

4.1 Driven dissipative Majorana dynamics

In this section, the theoretical concepts and physical ingredients are established, which are needed for the DD stabilisation and manipulation of dark states using a single Majorana box, see Fig. 4.1, and the dynamical equations are derived. The model is introduced in Sec. 4.1.1, where the dissipation arises from environmental electromagnetic fluctuations and the drive is applied to a pair of QDs. Afterwards, the Lindblad equation governing the time evolution of the combined QD-Majorana system is derived in Sec. 4.1.2, where numerical solutions to this Lindblad equation provide first insights to the dynamics of the system. Remarkably, up to initial transient behaviours, one can describe the dynamics in the Majorana sector in terms of a reduced Lindblad equation, where the QD degrees of freedom have been traced out. This step is described in Sec. 4.1.3, along with a discussion of the conditions under which this reduced Lindblad equation applies.

4.1.1 Model and low-energy theory

In this subsection, the model for the DD Majorana setup illustrated in Fig. 4.1 is introduced. The hardware ingredients needed for implementing the here discussed dark state stabilisation and manipulation protocols are outlined as well. Additionally, the effective low-energy Hamiltonian is considered, which one obtains after the high-energy charge states on the Majorana island are projected away.

Starting with the Majorana box, cf. Sec.3.1.1, one considers the setup depicted in Fig. 4.1, where a floating topological superconductor island harbours M zero-energy MBSs. In this case one has $M = 4$, but for generality, one can allow for general (even) values of M. The MBSs correspond to the Majorana operators $\gamma_\nu = \gamma_\nu^\dagger$, with anticommutator $\{\gamma_\nu, \gamma_{\nu'}\} = 2\delta_{\nu\nu'}$ and $\nu = 1, \ldots, M$. As indicated in Fig. 4.1, they could be realised as end states of two parallel InAs/Al nanowires [Lutchyn, 2018]. For concreteness, one considers class-D topological superconductor wires, where time reversal symmetry is broken by a magnetic field, cf. Sec. 2.1.3. Both nanowires are electrically connected by a superconducting bridge such that the entire island has a common charging energy, $E_C = e^2/(2C)$, with typical values of the order $E_C \approx 1$ meV [Lutchyn, 2018]. The isolated island ('box') has the Hamiltonian

$$\mathcal{H}_{\text{box}} = E_C(\hat{N} - N_g)^2. \tag{4.1}$$

The operator $\hat{N}$ refers to the total electron number on the box, and N_g is a tunable backgate parameter. In Eq. (4.1), hybridisation energies resulting from a finite overlap between different MBS pairs are neglected. These energy scales are exponentially small in the respective MBS-MBS distance. As will be discussed in Sec. 4.2.4, a small hybridisation between MBSs is often tolerable for DD-generated dark states or dark spaces. For the native Majorana qubit, such effects cause dephasing.

The here discussed theory requires several conditions to be satisfied. First, one assumes that the DD protocols only involve energy scales well below both E_C and the superconducting (proximity) gap Δ. This assumption implies that the ambient temperature satisfies $T \ll \min\{E_C, \Delta\}$. Then, one can neglect the effects of above-gap continuum quasiparticles, as has tacitly been assumed in Eq. (4.1), which otherwise constitute an intrinsic source of dissipation in the Majorana sector. In practice, one also needs to ensure that accidental low-energy Andreev states are not accessible, see [Manousakis, 2020]. Second, one considers Coulomb valley conditions, cf. Sec. 2.2.1, i.e. N_g is tuned close to an integer value and the box is only weakly coupled to the QDs in Fig. 4.1. In this case, $\mathcal{H}_{\text{box}}$ leads to charge quantisation, which dictates the fermion number parity of the island.

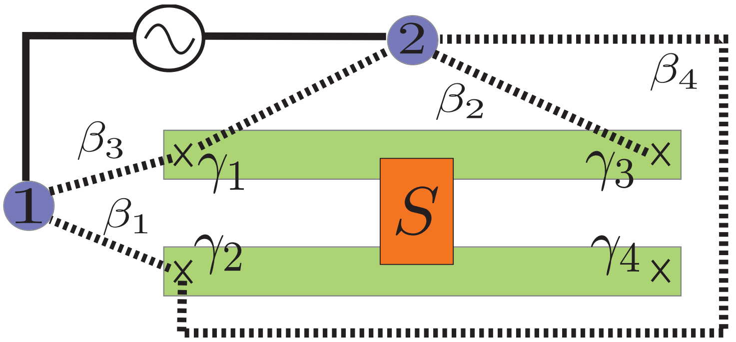

Figure 4.1: Schematic sketch of a driven dissipative Majorana box setup. The superconducting island harbours four Majorana operators γ_ν, three of which are tunnel-coupled to two single-level quantum dots (QDs, in blue). The Majoranas could be realised as end states of two parallel topological superconductor nanowires (green) which are electrically connected by a superconducting bridge (orange) [Plugge, 2017]. The tunnel links connecting QDs to MBSs are shown as dashed lines. The phases β_j in Eq. (4.44) are also indicated. Due to the large box charging energy, transport between different QDs through the Majorana island proceeds only via cotunneling processes. These cotunneling processes can be inelastic, involving the emission or absorption of photons from the dissipative electromagnetic environment. In addition, a driving field can pump electrons via a tunnel link between the QDs (solid line). [Gau, 2020b]

At temperatures well below the superconducting gap, only the Majorana sector of the full Hilbert space of the box has to be kept [Fu, 2010]. For $M = 4$, one arrives at a parity constraint in the Majorana sector, $\gamma_1\gamma_2\gamma_3\gamma_4 = \pm 1$, cf. 2.2.2, and the lowest-energy island state is then doubly degenerate. The corresponding Pauli operators associated with the resulting Majorana qubit are represented by Majorana bilinears, see Sec. 2.2.2

$$X = i\gamma_1\gamma_3, \quad Y = i\gamma_3\gamma_2, \quad Z = i\gamma_1\gamma_2. \tag{4.2}$$

The fact that Pauli operators correspond to spatially separated pairs of Majorana operators allows for unusually versatile qubit access options.

Next, the Hamiltonian describing the two QDs, $\mathcal{H}_\mathrm{d}$, in Fig. 4.1 is introduced. One starts from a general single-dot Hamiltonian, $\mathcal{H}_\mathrm{QD} = \sum_\alpha h_\alpha d_\alpha^\dagger d_\alpha + \epsilon_C\left(\hat{n} - n_g\right)^2$, where α labels electron spin and orbital degrees of freedom, d_α are fermion operators with $\hat{n} = \sum_\alpha d_\alpha^\dagger d_\alpha$, h_α describes a single-particle energy, and ϵ_C is the (large) dot charging energy [Karzig, 2017, Flensberg, 2011, Nazarov, 2010, Altland, 2010]. On low energy scales, the dot can be effectively described by a single spinless fermion level. Denoting the corresponding level energy by ϵ_j for QD $j = 1, 2$, one arrives at

$$\mathcal{H}_\mathrm{d} = \sum_{j=1,2} \epsilon_j d_j^\dagger d_j, \tag{4.3}$$

see [Karzig, 2017] for details. The energies ϵ_j can be controlled by variation of the gate voltage parameter n_g. Without loss of generality, $\epsilon_2 > \epsilon_1$ is assumed throughout, where both energies should satisfy $|\epsilon_j| \ll \min\{E_C, \Delta\}$. Additionally, one employs a time-dependent electromagnetic driving field which can pump single electrons between the two QDs via a tunnel link. To this end, a suitable AC voltage can be applied to a gate electrode located near this link. The respective Hamiltonian contribution is given by [Platero, 2004]

$$\mathcal{H}_\mathrm{drive}(t) = w(t) d_1^\dagger d_2 + \mathrm{h.c.}, \quad w(t) = t_{12} + 2A\cos\left(\omega_0 t\right), \tag{4.4}$$

where ω_0 denotes the drive frequency and A the drive amplitude. In the following, one assumes that the static contribution vanishes, $t_{12} = 0$, because a small coupling $t_{12} \neq 0$ will not affect the dissipator in the Lindblad equation, which is derived below, and thus does not change the physics in a qualitative manner.
For the discussed systems one considers the Coulomb valley regime where the total charge on the box is fixed by the charging term in Eq. (4.1) on time scales $\delta t > 1/E_C$ [Romito, 2014]. The total particle number on the QDs, $N_\mathrm{d} = \sum_j d_j^\dagger d_j$, is therefore also conserved on such time scales. For even $N_\mathrm{d} \in \{0, 2\}$, the inter-QD dynamics is effectively frozen out. Thus, the focus lies on the case $N_\mathrm{d} = 1$, where the pair of QDs forms a spin-1/2 degree of freedom corresponding to Pauli operators $\tau_{x,y,z}$ with $\tau_\pm = (\tau_x \pm i\tau_y)/2$,

$$\tau_+ = \tau_-^\dagger = d_1^\dagger d_2, \quad \tau_z = d_1^\dagger d_1 - d_2^\dagger d_2 = 2\tau_+\tau_- - 1. \tag{4.5}$$

Next, the tunnel couplings connecting the QDs to the island are discussed.

In the above parameter regime, tunneling to the box has to proceed via MBSs since no other low-energy island states are available. Such processes can be inelastic due to the coupling to a bosonic environment. One here considers the case of a dissipative electromagnetic environment, which can be modeled by including fluctuating phases $\theta_{j\nu}$ in the tunneling matrix elements[Nazarov, 2010, Devoret, 1990, Girvin, 1990],

$$\hat{\lambda}_{j\nu} = \lambda_{j\nu} e^{i\theta_{j\nu}}, \tag{4.6}$$

with dimensionless complex-valued parameters $\lambda_{j\nu}$ subject to $\max\{|\lambda_{j\nu}|\} = 1$. Here, $\lambda_{j\nu}$ determines the transparency of the tunnel link between the QD fermion d_j and the Majorana state γ_ν in the absence of electromagnetic noise [Zazunov, 2016]. With the overall hybridisation energy t_0 characterising the QD-MBS couplings, the tunneling Hamiltonian is given by [Nazarov, 2010, Devoret, 1990, Girvin, 1990]

$$\mathcal{H}_\mathrm{tun} = t_0 e^{-i\hat{\phi}} \sum_{j,\nu} \hat{\lambda}_{j\nu} d_j^\dagger \gamma_\nu + \mathrm{h.c.} \tag{4.7}$$

The phase operator $\hat{\phi}$ of the island obeys the commutator $[\hat{N}, \hat{\phi}] = -i$ with the number operator $\hat{N}$ in Eq. (4.1). The $e^{i\hat{\phi}}$ ($e^{-i\hat{\phi}}$) factor in Eq. (4.7) thus ensures that an electron charge is added to (subtracted from) the island in a tunneling process, cf. Sec. 2.2.1. It is well known that the electromagnetic potential fluctuations predominantly couple to the phase of the wave function [Devoret, 1990, Girvin, 1990]. This fact is expressed by the appearance of the fluctuating tunnel couplings $\hat{\lambda}_{j\nu}$, see Eq. (4.6), in the tunneling Hamiltonian (4.7).
For concreteness, one assumes that the electromagnetic environment can be modeled by a single bosonic bath, see also [Munk, 2019]. Representing the bath by an infinite set of harmonic oscillators [Weiss, 2007, Breuer, 2006], the environmental Hamiltonian reads $\mathcal{H}_\mathrm{env} = \sum_m E_m b_m^\dagger b_m$, with the energy $E_m > 0$ of the photon mode described by the boson annihilation operator b_m. In practice, the relevant bath energies E_m are strongly suppressed above a cutoff frequency ω_c. With dimensionless real-valued couplings $g_{j\nu,m}$, the stochastic phase operators $\theta_{j\nu}$ are written as

$$\theta_{j\nu} = \sum_m g_{j\nu,m} \left(b_m + b_m^\dagger\right). \tag{4.8}$$

Clearly, they commute, meaning $[\theta_{j\nu}, \theta_{j'\nu'}] = 0$.

Low-energy theory

In the following the effective low-energy theory is established. The parameter regime of interest is defined by the conditions

$$\max\{T, A, t_0, \omega_0, \omega_c, |\epsilon_j|\} \ll \min\{E_C, \Delta\}. \tag{4.9}$$

The parameters on the left side of Eq. (4.9) affect the dissipative transition rates in the Lindblad equation, which is derived below. These rates in turn set the time scale on which dark states are approached. In the following, a concise description is adopted, whereby, for engineering a stabilisation protocol targeting a specific dark state, it suffices to adjust the complex-valued tunnel link parameters $\lambda_{j\nu}$. In practice, those *state design parameters* can be changed via gate voltages. Note that under the conditions in Eq. (4.9), boson-assisted processes can neither excite above-gap quasi-particles nor higher-energy charge states on the island.

The full Hamiltonian can then be projected onto the doubly degenerate ground-state space of the box, $\mathcal{H}(t) \to \mathcal{H}_{\text{eff}}(t)$. Using a Schrieffer-Wolff transformation, cf. Sec. 2.3.2, to implement this projection, and noting that $\mathcal{H}_{\text{box}}$ reduces to an irrelevant constant energy shift, one arrives at the effective low-energy Hamiltonian

$$\mathcal{H}_{\text{eff}}(t) = \mathcal{H}_{\text{d}} + \mathcal{H}_{\text{env}} + \mathcal{H}_{\text{drive}}(t) + \mathcal{H}_{\text{cot}}, \tag{4.10}$$

with the drive term in Eq. (4.4) and the cotunneling contribution

$$\mathcal{H}_{\text{cot}} = g_0 \sum_{j,k=1,2} \hat{W}_{jk} \left(2d_j^\dagger d_k - \delta_{jk}\right), \quad g_0 \equiv \frac{t_0^2}{E_C}. \tag{4.11}$$

One here uses the operators

$$\hat{W}_{jk} = \sum_{1\le\mu<\nu\le M} \left(\hat{\lambda}_{j\nu}\hat{\lambda}_{k\mu}^\dagger - \hat{\lambda}_{j\mu}\hat{\lambda}_{k\nu}^\dagger\right)\gamma_\mu\gamma_\nu. \tag{4.12}$$

Equation (4.11) describes cotunneling paths through the box, where the energy of the intermediate virtual state has been approximated by E_C, cf. Eq. (4.9), and photon emission and absorption processes are encoded by the $\hat{\lambda}$ factors in Eq. (4.6).

For even QD occupation number N_{d}, Eq. (4.11) reduces to

$$\mathcal{H}_{\text{cot}}^{(N_{\text{d}}=0,2)} = g_0 \,\text{sgn}(N_{\text{d}} - 1) \sum_j \hat{W}_{jj}. \tag{4.13}$$

For $N_{\text{d}} = 1$, using the notation

$$\hat{W}_+ \equiv \hat{W}_{12}, \quad \hat{W}_x = \hat{W}_+ + \hat{W}_-, \quad \hat{W}_y = i(\hat{W}_+ - \hat{W}_-), \quad \hat{W}_z = \hat{W}_{11} - \hat{W}_{22}, \tag{4.14}$$

where $\hat{W}_- = \hat{W}_+^\dagger$, one finds that Eq. (4.11) can instead be expressed in the form

$$\mathcal{H}_{\text{cot}}^{(N_{\text{d}}=1)} = g_0 \sum_{a=x,y,z} \hat{W}_a \tau_a, \tag{4.15}$$

with the QD Pauli operators τ_a in Eq. (4.5). It is worth mentioning that like the $\hat{W}_{jk}$ operators in Eq. (4.12), the $\hat{W}_a$ still contain the phase fluctuation operators due to the electromagnetic environment. In order to realise the most general qubit-qubit exchange coupling between the QD spin $\{\tau_a\}$ and the $M = 4$ Majorana box spin (X, Y, Z) in the

cotunneling regime, one has to specify nine independent (tunable) real-valued coupling constants. For the $M = 4$ case in Fig. 4.1, taking into account gauge invariance — which allows one to set one of the $\lambda_{j\nu}$ to a real value —, the five different complex-valued hopping parameters $\lambda_{j\nu}$ are sufficient. On top of that, the direct tunnel amplitude between the QDs is assumed to be real-valued after setting $t_{12} = 0$ in Eq. (4.4).
To simplify the subsequent analysis, one assumes that the dominant contribution to the environmental electromagnetic noise comes from the long wavelength part. In effect, such contributions will cause dephasing of the QDs, e.g. due to the presence of a backgate electrode. This assumption is also consistent with the picture of a single bath. To good accuracy, the couplings $g_{j\nu,m}$ in Eq. (4.8) then do not depend on the Majorana index ν, i.e. $g_{j\nu,m} = g_{j,m}$. As a consequence, also the fluctuating phases (4.8) become ν-independent, $\theta_{j\nu} = \theta_j$. In this case, the diagonal entries $\hat{W}_{jj}$ are insensitive to electromagnetic noise and the bath completely decouples for even N_d, see Eq. (4.13).
From now on, the focus lies on the case of a single electron shared by the QDs, $N_\mathrm{d} = 1$. Defining the phase operator

$$\theta \equiv \theta_1 - \theta_2 = \sum_m (g_{1,m} - g_{2,m}) \left(b_m + b_m^\dagger\right), \tag{4.16}$$

Eq. (4.15) then yields

$$\mathcal{H}_\mathrm{cot} = 2g_0 \left(e^{i\theta} W_+ \tau_+ + \mathrm{h.c.}\right) + g_0 W_z \tau_z. \tag{4.17}$$

The operators W_+ and W_z correspond to 'undressed' ($\theta_{j\nu} \to 0$) versions of $\hat{W}_+$ and $\hat{W}_z$, respectively. These operators act only on the Hilbert space sector describing Majorana states. Comparing to Eq. (4.12), one has

$$W_{jk} = \sum_{\mu<\nu}^{M} \left(\lambda_{j\nu}\lambda_{k\mu}^* - \lambda_{j\mu}\lambda_{k\nu}^*\right) \gamma_\mu \gamma_\nu. \tag{4.18}$$

For the device in Fig. 4.1, the W_{jk} operators can be expressed in terms of the Pauli operators (X, Y, Z) in Eq. (4.2), see below.

In order to allow for the derivation of the Lindblad master equation, cf. Sec. 2.5.1, for the here discussed system, the interaction Hamiltonian in Eq. (4.17) has to be rewritten in normal-ordered form, i.e. with respect to its bath expectation value. Therefore, the electromagnetic environment is first characterised by its correlations function to properly define such averaged quantities. The equilibrium density matrix of the thermal environment is given by

$$\rho_\mathrm{env} = Z_\mathrm{env}^{-1} e^{-H_\mathrm{env}/T} \quad \text{with} \quad Z_\mathrm{env} = \mathrm{tr}_\mathrm{env}\, e^{-H_\mathrm{env}/T}, \tag{4.19}$$

where 'tr_env' denotes a trace operation over the environmental bosons. Using $\langle \hat{O} \rangle_\mathrm{env} \equiv \mathrm{tr}_\mathrm{env}(\hat{O}\rho_\mathrm{env})$, one can define the correlation function [Weiss, 2007]

$$J_\mathrm{env}(t) = \langle [\theta(t) - \theta(0)]\theta(0) \rangle_\mathrm{env} = \int_0^\infty \frac{d\omega}{\pi} \frac{\mathcal{J}(\omega)}{\omega^2} \left\{ [\cos(\omega t) - 1] \coth\left(\frac{\omega}{2T}\right) - i \sin(\omega t) \right\}, \tag{4.20}$$

with the spectral density

$$\mathcal{J}(\omega) = \pi \sum_m (g_{1,m} - g_{2,m})^2 E_m^2 \delta(\omega - E_m). \tag{4.21}$$

Switching to the continuum limit in bath frequency space, one focuses on the practically most important Ohmic case with $\mathcal{J}(\omega) \propto \omega$ in the low-frequency limit. In concrete calculations, the model spectral density [Weiss, 2007] is used

$$\mathcal{J}(\omega) = \alpha\omega e^{-\omega/\omega_c}, \tag{4.22}$$

where α is a dimensionless system-bath coupling and frequencies above ω_c are exponentially suppressed. For a related discussion in the context of Majorana qubits, see [Munk, 2019]. The parameter α is related to the environmental impedance $Z(\omega)$, cf. [Devoret, 1990],

$$\alpha = \frac{e^2}{2h}\mathrm{Re}Z(\omega = 0). \tag{4.23}$$

In the following $\alpha < 1$ is considered.

For the subsequent discussion, one rewrites $\mathcal{H}_{\mathrm{cot}}$ in normal-ordered form relative to the phase fluctuations,

$$\mathcal{H}_{\mathrm{cot}} = \mathcal{H}_{\mathrm{cot}}^{(0)} + V, \tag{4.24}$$

where $\mathcal{H}_{\mathrm{cot}}^{(0)}$ is the expectation value of $\mathcal{H}_{\mathrm{cot}}$ with respect to phase fluctuations and V represents the coupling of the combined QD-MBS system to phase fluctuations. Since $\langle\theta^2\rangle_{\mathrm{env}}$ diverges in the Ohmic case, one has $\langle e^{i\theta}\rangle_{\mathrm{env}} = 0$, resulting in

$$\mathcal{H}_{\mathrm{cot}}^{(0)} \equiv \langle\mathcal{H}_{\mathrm{cot}}\rangle_{\mathrm{env}} = g_0 W_z \tau_z. \tag{4.25}$$

The interaction term in Eq. (4.24) is then given by

$$V = 2g_0\left(e^{i\theta}W_+\tau_+ + \mathrm{h.c.}\right). \tag{4.26}$$

By construction, $\langle V\rangle_{\mathrm{env}} = 0$. Correlation functions of exponentiated phase fluctuations are given by ($s = \pm 1$)

$$\langle e^{is\theta(t)}e^{-is\theta(0)}\rangle_{\mathrm{env}} = e^{J_{\mathrm{env}}(t)} \tag{4.27}$$

with $J_{\mathrm{env}}(t)$ in Eq. (4.20).

From now on, one shall switch to the interaction picture with respect to $\mathcal{H}_{\mathrm{d}} + \mathcal{H}_{\mathrm{env}}$. The Hamiltonian then takes the form, see Eqs. (4.10) and (4.24),

$$\mathcal{H}_{\mathrm{eff},I}(t) = \mathcal{H}_{0,I}(t) + V_I(t), \qquad \mathcal{H}_{0,I}(t) = \mathcal{H}_{\mathrm{drive},I}(t) + \mathcal{H}_{\mathrm{cot},I}^{(0)}(t). \tag{4.28}$$

For simplicity, the 'I' index (for interaction picture) is dropped in what follows and one focuses on resonant drive conditions,

$$\omega_0 = \epsilon_2 - \epsilon_1. \tag{4.29}$$

In the regime $\omega_0 \gg T$ considered below, one can apply the rotating wave approximation (RWA) [Gardiner, 2004]. As a consequence, $\mathcal{H}_{\mathrm{drive}}(t) \to \tilde{\mathcal{H}}_{\mathrm{drive}}$ with

$$\tilde{\mathcal{H}}_{\mathrm{drive}} = A\left(d_1^\dagger d_2 + d_2^\dagger d_1\right) = A\tau_x, \tag{4.30}$$

resulting in a time-independent drive Hamiltonian in the interaction picture. If the drive frequency is slightly detuned, $\omega_0 = \epsilon_2 - \epsilon_1 + \delta\omega_0$, a residual time dependence remains, $\mathcal{H}_{\mathrm{drive}}(t) = e^{-i\delta\omega_0 t}Ad_1^\dagger d_2+$ h.c., after applying the RWA. However, one finds that the final Lindblad equation for the dynamics of the Majorana sector in Sec. 4.1.3 is not affected to leading order in $\delta\omega_0$. The here discussed DD protocols are therefore robust with respect to a mismatch in the resonance condition (4.29). In the following $\delta\omega_0 = 0$ is assumed.

4.1.2 Markov master equations

In this subsection, the time evolution of the reduced density matrix, $\rho(t)$, describing the coupled system defined by the MBSs and the pair of QD fermions is considered. After tracing over the environmental bosons, one arrives at a Lindblad master equation for the dynamics of $\rho(t)$. With $\omega_0 = \epsilon_2 - \epsilon_1$ and $g_0 = t_0^2/E_C$, one considers the regime

$$g_0 \ll T \ll \omega_0, \quad A \leq g_0. \tag{4.31}$$

In particular, $T \ll \omega_0$ is needed to justify the RWA, while $g_0 \ll T$ is required for the Born-Markov approximation, cf. Sec. 2.5.1. In addition, the regime $g_0 \ll T$ enables to neglect emission and absorption processes taking place only in the Majorana sector since the bath is then unable to resolve such transitions. Of course, boson-assisted inter-QD transitions resulting from cotunneling processes are accounted for. Finally, Eq. (4.31) states that one studies a weakly driven system with drive amplitude $A \leq g_0$. The opposite strongly driven case is briefly discussed in App. A of [Gau, 2020b]. Note that inelastic corrections to the drive Hamiltonian due to electromagnetic phase fluctuations, see Eq. (4.19), can be neglected by the secular approximation, cf. Sec. II.B of [Shavit, 2019].

The master equation governing the dynamics of the density matrix $\rho(t)$ for the combined system (QDs and Majorana sector) is obtained by following the standard derivation of Born-Markov master equations, see Sec. 2.4.1. One assumes a factorised initial (time $t = 0$) density matrix of the total system, $\rho_{\text{tot}}(0) = \rho(0) \otimes \rho_{\text{env}}$, with ρ_{env} in Eq. (4.19). Starting from the von-Neumann equation for $\rho_{\text{tot}}(t)$ subject to $H_{\text{eff}}(t)$ in Eq. (4.28), one traces over the environmental modes and applies the Born-Markov approximation [Weiss, 2007, Breuer, 2006, Gardiner, 2004]. As a result, $\rho(t)$ obeys the master equation

$$\partial_t \rho(t) = -i\left[\mathcal{H}_0(t), \rho(t)\right] - \operatorname{tr}_{\text{env}} \int_0^\infty d\tau \left[V(t), \left[V(t-\tau) + \mathcal{H}_0(t-\tau), \rho(t) \otimes \rho_{\text{env}}\right]\right], \tag{4.32}$$

where one has used that, by construction, $\operatorname{tr}_{\text{env}}\left[V(t), \rho(0) \otimes \rho_{\text{env}}\right] = 0$. Similarly, the mixed term involving $V(t)$ and $\mathcal{H}_0(t-\tau)$ vanishes identically. Then, one is left with the coherent evolution term due to $\mathcal{H}_0(t)$, and the double commutator containing two V terms.

Unfolding the double commutator, one arrives at a master equation of Lindblad type, see [Lindblad, 1976] and [Lindblad, 1983],

$$\partial_t \rho(t) = -i\left[H_{\text{L}}, \rho(t)\right] + \sum_{\pm} \Gamma_{\pm} \mathcal{D}[J_{\pm}]\rho(t). \tag{4.33}$$

The subscript ‘L’ in H_{L} is meant to clarify that this Hamiltonian appears in a Lindblad equation. The dissipator $\mathcal{L}$ acts as superoperator on ρ [Breuer, 2006], see Eq. (2.90). The two *jump operators* in Eq. (4.33) are given by

$$J_{\pm} = 2W_{\pm}\tau_{\pm} = J_{\mp}^{\dagger}, \tag{4.34}$$

with the corresponding dissipative transition rates,

$$\Gamma_{\pm} = 2g_0^2 \, \mathrm{Re}\Lambda_{\pm}. \tag{4.35}$$

Here, one defines the quantities

$$\Lambda_{\pm} = \int_0^\infty dt \, e^{\pm i\omega_0 t} e^{J_{\text{env}}(t)}, \tag{4.36}$$

with the bath correlation function (4.20). Their imaginary parts give Lamb shift parameters,

$$h_\pm = g_0^2\,\mathrm{Im}\Lambda_\pm, \tag{4.37}$$

which appear in the Hamiltonian governing the coherent time evolution in Eq. (4.33),

$$H_\mathrm{L} = A\tau_x + g_0 W_z\tau_z + \sum_\pm h_\pm J_\pm^\dagger J_\pm. \tag{4.38}$$

The first two terms in H_L originate from $\mathcal{H}_0$ in Eq. (4.30), while the third term contains the Lamb shifts (4.37).

Next one observes that Eq. (4.20) implies the general relation

$$J_\mathrm{env}\left(-t - i/T\right) = J_\mathrm{env}(t) \tag{4.39}$$

in the complex-time plane. Using Eq. (4.39) in Eq. (4.36) then results in a detailed balance relation, $\Lambda_- = e^{-\omega_0/T}\Lambda_+$. As a consequence, for arbitrary parameters, one finds

$$\Gamma_- = e^{-\omega_0/T}\Gamma_+, \quad h_- = e^{-\omega_0/T}h_+. \tag{4.40}$$

In particular, for $T \ll \omega_0$, the dissipative rate Γ_- associated with the jump operator J_- will be exponentially suppressed against the rate Γ_+. The dissipative part of the Lindblad equation (4.33) is therefore completely dominated by the jump operator J_+.

It is a distinguishing feature of the here introduced DD platform that jump operators can be directly implemented by designing *unidirectional* inelastic cotunneling paths connecting pairs of QDs via the box, with the overall energy scale g_0. The QDs are also directly coupled by a driven tunnel link $w(t)$, see Eq. (4.4), with overall energy scale A. For $T \ll \omega_0$, as far as inter-dot transitions via the box are concerned, only photon emission processes are relevant. As a consequence, only transitions from the energetically higher QD 2 to QD 1 may take place, corresponding to the jump operator $J_+ \propto \tau_+$, see Eqs. (4.5) and (4.34). Such transitions act on the Majorana state according to the operator W_+. As shown below, this operator can be engineered at will by adjusting the tunneling parameters $\lambda_{j\nu}$, which in turn is possible by changing suitable gate voltages. The driving field pumps the dot electron in the opposite direction, i.e. from QD $1 \to 2$, and for a small pumping rate, $A \leq g_0$, one obtains a steady state circulation $1 \to 2 \to 1$ by alternating pumping and cotunneling processes. On the contrary, for $A > g_0$, pumping processes will dominate and the cotunneling channel is effectively suppressed.

To facilitate analytical progress, one might consider the case $\omega_0 \ll \omega_c$. One then finds [Weiss, 2007]

$$J_\mathrm{env}(t) \simeq -2\alpha\ln\left(\frac{\omega_c}{\pi T}\sinh(\pi T t)\right) - i\pi\alpha\,\mathrm{sgn}(t), \tag{4.41}$$

and with the Gamma function $\Gamma(z)$, one arrives at

$$\Gamma_+ \simeq \Gamma(1-2\alpha)\sin(2\pi\alpha)\left(\frac{\omega_0}{\omega_c}\right)^{2\alpha}\frac{2g_0^2}{\omega_0}, \qquad h_+ \simeq \frac{1}{2}\cot(2\pi\alpha)\Gamma_+. \tag{4.42}$$

For the device in Fig. 4.1, using the Pauli operators (4.2), the jump operators $J_\pm = J_\mp^\dagger$ follow from Eq. (4.34) in the general form $J_+ = \tilde{J}_+\tau_+$ with

$$\tilde{J}_+ = 2ie^{i\beta_2}|\lambda_{23}|\left(e^{-i\beta_3}|\lambda_{11}|X - e^{-i\beta_1}|\lambda_{12}|Y\right) - 2i\left[e^{-i\beta_1}|\lambda_{12}\lambda_{21}| - e^{i\beta_4}|\lambda_{11}\lambda_{22}|\right]Z, \tag{4.43}$$

where the phases $\beta_{1,2,3,4}$ are indicated in Fig. 4.1. They are connected to the phases $\chi_{j\nu}$ in the tunneling parameters, $\lambda_{j\nu} = |\lambda_{j\nu}|e^{-i\chi_{j\nu}}$, by the relations

$$\beta_1 = \chi_{12}, \quad \beta_2 = \chi_{23}, \quad \beta_3 = \chi_{11}, \quad \beta_4 = \chi_{22}, \tag{4.44}$$

with the gauge choice $\chi_{21} = 0$. In particular, $\beta_1 - \beta_3$ (β_2) is the loop phase accumulated along the shortest closed tunneling trajectory involving only QD 1 (QD 2), cf. Eq. (4.46). These phases, as well as the absolute values $|\lambda_{j\nu}|$, can be experimentally varied, e.g., by changing the voltages on nearby gates. Note that $\tilde{J}_+$ is fully determined by selecting the state design parameters $\lambda_{j\nu}$. The Hamiltonian H_{L} then follows as

$$H_{\mathrm{L}} = A\tau_x + 2g_0\tilde{J}_z\tau_z + \sum_{\pm} h_\pm J_\pm^\dagger J_\pm, \tag{4.45}$$

$$\begin{aligned}\tilde{J}_z = {} & \frac{1}{2}\bar{\lambda}^2 + \sin\beta_2|\lambda_{21}\lambda_{23}|X + \sin\left(\beta_4 - \beta_2\right)|\lambda_{22}\lambda_{23}|Y \\ & + \left[\sin\beta_4|\lambda_{21}\lambda_{22}| - \sin\left(\beta_1 - \beta_3\right)|\lambda_{11}\lambda_{12}|\right] Z,\end{aligned} \tag{4.46}$$

where $\bar{\lambda}^2 \equiv |\lambda_{11}|^2+|\lambda_{12}|^2+|\lambda_{21}|^2+|\lambda_{22}|^2+|\lambda_{23}|^2$. It is worth mentioning that the operators $\tilde{J}_\pm$ and $\tilde{J}_z$ act only on the Majorana subsector.

To illustrate the above general expressions, one might consider a simple example, where the stabilisation parameters are taken subject to the conditions

$$|\lambda_{11}| = |\lambda_{12}|, \quad \lambda_{22} = 0, \quad \beta_1 = -\beta_2 = \pi/2, \quad \beta_3 = \beta_4 = 0. \tag{4.47}$$

Using Eq. (4.43), the dominant jump operator contributing to the Lindbladian is then given by

$$J_+ = 2|\lambda_{11}|\left(2|\lambda_{23}|\sigma_+ + |\lambda_{21}|Z\right)\tau_+, \tag{4.48}$$

where $\sigma_\pm = (X \pm iY)/2$. For $|\lambda_{23}| \gg |\lambda_{21}|$, the Lindbladian will then automatically drive an arbitrary Majorana state ρ_{M} towards $|0\rangle\langle 0|$, with the Z-eigenstate $|0\rangle$ to eigenvalue $+1$, i.e., $Z|0\rangle = |0\rangle$. Here, the reduced density matrix $\rho_{\mathrm{M}}(t)$ describes the Majorana sector only, see Sec. 4.1.3. However, the operator $\tilde{J}_z$ appearing in the Hamiltonian H_{L} still contains a small X component, see Eq. (4.46), which could potentially disrupt the action of the dissipator. Nonetheless, one finds that for small $|\lambda_{21}|$, the desired state $|0\rangle$ is approached with high fidelity, regardless of the initial system state $\rho(0)$. An optimised parameter choice for stabilising $|0\rangle$ will be discussed in Sec. 4.2.

Numerical results

Next, a numerical integration of Eq. (4.33) using the approach of [Johansson, 2012, Johansson, 2013] is used to motivate simplifying the Lindbladian. Numerical results for the above parameters are shown in Figs. 4.2 and 4.3. While the goal of the DD protocol is to stabilise a selected state in the Majorana sector, it is useful to also study the dynamics in the QD sector, see Fig. 4.2. One starts from a pure initial state, $\rho(0) = |\Psi(0)\rangle\langle\Psi(0)|$, with $|\Psi(0)\rangle = |+\rangle \otimes |0\rangle_{\mathrm{d}}$, where the $\tau_z = +1$ QD eigenstate, $|0\rangle_{\mathrm{d}}$, describes an electron located in the energetically lower QD 1, with QD 2 left empty, see Eq. (4.5). The initial Majorana state has been chosen as the X-eigenstate $|+\rangle$ with eigenvalue $+1$. In [Gau, 2020b] it was checked that the same long-time limit of $\rho(t)$ is reached for other initial states. One defines the purity of the system state as

$$P_s(t) = \mathrm{tr}\rho^2(t). \tag{4.49}$$

The upper left panel of Fig. 4.2 shows that the purity approaches a value close to the largest possible value ($P_s = 1$) at long times. As observed from Fig. 4.3, the DD protocol steers the Majorana state towards the pure state $|0\rangle$, i.e. towards the north pole of the corresponding Bloch sphere. For the shown example, the QD state ρ_{d} has most probability

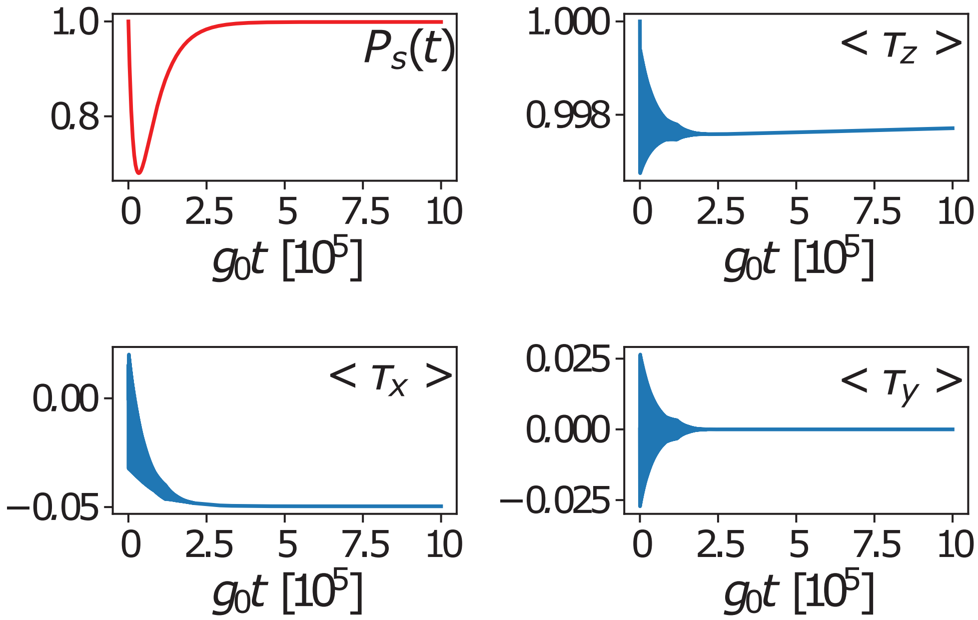

Figure 4.2: Driven dissipative dynamics for the setup in Fig. 4.1, illustrating the time-dependent expectation values of the Pauli operators $\tau_{x,y,z}$ describing the QDs, see Eq. (4.5). It also shows the purity, $P_s(t)$, of the system state, see Eq. (4.49). All results were obtained by numerical integration of the Lindblad equation (4.33) for the density matrix ρ describing the QDs and the Majorana sector, with $H_{\rm L}$ in Eq. (4.46). The parameters were chosen as in Eq. (4.47), with $T/g_0 = 4$, $\omega_0/g_0 = 40$, $\omega_c/g_0 = 200$, $A/g_0 = 0.1$, $\alpha = 1/4$, $|\lambda_{11}| = |\lambda_{12}| = |\lambda_{23}| = 1$, and $|\lambda_{21}| = 0.1$. Fast transient oscillations in $\langle \tau_a(t) \rangle$ are not resolved on the shown time scale, corresponding to shaded regions. The respective dynamics in the Majorana sector is depicted in Fig. 4.3. [Gau, 2020b]

weight in the energetically lower QD 1. Indeed, Fig. 4.2 shows that at long times, the electron shared by the two QDs will predominantly relax to QD 1, corresponding to the state $|0\rangle_{\rm d}$. Nonetheless, it is of crucial importance that the occupation probability p for encountering the electron in the energetically higher QD 2 (corresponding to the state $|1\rangle_{\rm d}$) remains finite at long times. One finds $p \approx 0.001$ for the parameters in Fig. 4.2.
One concludes that the system state factorises at long times, $\rho(t) \simeq \rho_{\rm M} \otimes \rho_{\rm d}$ with $\rho_{\rm M} = |0\rangle\langle 0|$. The approach of the Majorana state towards $|0\rangle$ takes place on a time scale given by the inverse of the dissipative gap of the reduced Lindbladian describing the Majorana sector only, see Sec. 4.2 below. The relaxation time scales for the QD subsystem can be longer, compare Figs. 4.2 and 4.3.
Finally, one can remark that for the special case of $\lambda_{21} = 0$, the electron shared by the two QDs will *not* predominantly relax to the energetically lower QD 1. Here, there are only two cotunneling paths between both QDs, namely the constituents forming the operator $4|\lambda_{11}\lambda_{23}|\sigma_+$ in Eq. (4.48). Both paths interfere destructively once the Majorana island is stabilised in the state $|0\rangle$. An arbitrarily weak drive can then overcome all dissipative effects in the long-time limit. In contrast to what happens for $\lambda_{21} \neq 0$, the QDs will thus realise an equal-weight mixture of $|0\rangle_{\rm d}$ and $|1\rangle_{\rm d}$. Nonetheless, the reduced Lindblad equation (4.52) below still applies, with $p \to 1/2$ and $p_\perp \to 0$ in Eq. (4.51).

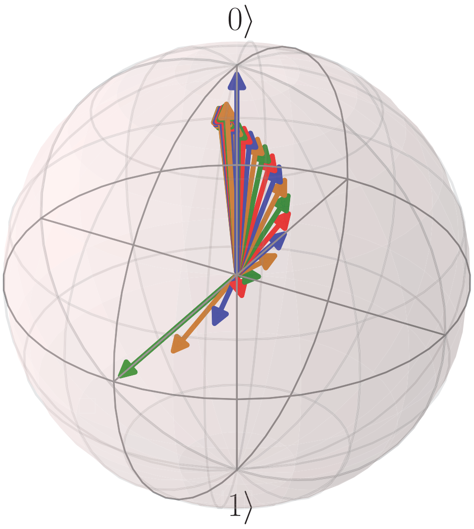

Figure 4.3: Time evolution of the Bloch vector, $(\langle X\rangle, \langle Y\rangle, \langle Z\rangle)(t)$, describing the Majorana state $\rho_{\mathrm{M}}(t)$ for the same parameters as in Fig. 4.2. The expectation value is computed by numerically integrating the Lindblad equation. Starting from the initial X-eigenstate $|+\rangle$, the DD protocol stabilises the dark state $|0\rangle$ at long times, corresponding to the north pole of the Bloch sphere. The intermediate states (with alternating colors) were obtained at times $g_0 t \in \{5\times 10^3, 10\times 10^3, \ldots, 15\times 10^4\}$. [Gau, 2020b]

4.1.3 Lindblad master equation for the Majorana sector

The observations in Sec. 4.1.2 allow to derive a reduced Lindblad equation, which directly describes the dynamics of $\rho_{\mathrm{M}}(t)$ in the Majorana sector alone. To that end, one now traces also over the QD subspace. For long times, the above numerical simulations generically show that $\rho(t)$ factorises into a Majorana part, $\rho_{\mathrm{M}}(t)$, and a QD contribution, $\rho_{\mathrm{d}}(t)$,

$$\rho(t\to\infty) \simeq \rho_{\mathrm{M}}(t)\otimes\rho_{\mathrm{d}}(t). \tag{4.50}$$

For tracing over the QD part, one can effectively use a time-independent *Ansatz*,

$$\rho_{\mathrm{d}} = \begin{pmatrix} 1-p & p_\perp \\ p_\perp^* & p \end{pmatrix}, \tag{4.51}$$

written in the basis $\{|0\rangle_{\mathrm{d}}, |1\rangle_{\mathrm{d}}\}$ selected by the coupling to the QDs. Here, $p\neq 0$ refers to the occupation probability of the energetically higher QD 2. This probability can be determined by numerically solving Eq. (4.33), cf. Sec. 4.1.2, or it may be treated as phenomenological parameter. A simple estimate predicts $p\approx \max(A, g_0)/\omega_0$. Noting that a small but finite expectation value $\langle\tau_x\rangle\neq 0$ is observed in Fig. 4.2 at long times, one has to also included an off-diagonal term $(p_\perp)$ in Eq. (4.51).
Inserting Eq. (4.50) into Eq. (4.33) and tracing over the QD subsystem, one arrives at a Lindblad equation for the 2×2 density matrix $\rho_{\mathrm{M}}(t)$ only,

$$\partial_t\rho_{\mathrm{M}}(t) = -i[\tilde{H}_{\mathrm{L}}, \rho_{\mathrm{M}}] + \sum_{s=\pm}\tilde{\Gamma}_s\mathcal{L}[\tilde{J}_s]\rho_{\mathrm{M}}(t), \tag{4.52}$$

where the jump operators $\tilde{J}_\pm$ have been defined in Eq. (4.43). The dissipative transition rates $\tilde{\Gamma}_\pm$ in Eq. (4.52) are given by

$$\tilde{\Gamma}_+ = p\Gamma_+, \quad \tilde{\Gamma}_- = (1-p)\Gamma_-, \tag{4.53}$$

cf. Eqs. (4.35) and (4.42). The coherent time evolution in Eq. (4.52) is governed by the Hamiltonian

$$\tilde{H}_{\mathrm{L}} = 2(1-2p)g_0\tilde{J}_z + \sum_{\pm} \tilde{h}_{\pm}\tilde{J}_{\pm}^{\dagger}\tilde{J}_{\pm}, \tag{4.54}$$

where $\tilde{J}_z$ has been specified in Eq. (4.46) and the Lamb shifts $\tilde{h}_{\pm}$ are given by

$$\tilde{h}_{+} = ph_{+}, \quad \tilde{h}_{-} = (1-p)h_{-}. \tag{4.55}$$

The drive amplitude A then appears only implicitly through the dependence $p = p(A)$. Note that within the RWA, no contributions $\propto p_{\perp}$ appear in Eq. (4.52). Indeed, the RWA allows one to neglect terms $\propto \tau_{+}\rho\tau_{+}$, which stem from $p_{\perp} \neq 0$.

Importantly, apart from the initial transient behaviour, all of the numerical results for the Majorana dynamics obtained from the full Lindblad equation for the combined QD-MBS system, Eq. (4.33), are quantitatively reproduced by using the simpler Lindblad equation (4.52). This statement is valid for arbitrary model parameters subject to Eqs. (4.9) and (4.31). The integration over the QD degrees of freedom as carried out above relies on the facts that (i) the convergence towards the target state is dictated by the Majorana sector, and that (ii) the QD and MBS degrees of freedom always decouple in the long-time limit, see Eq. (4.50). The latter feature has been established by extensive numerical simulations of Eq. (4.33). The reduced Lindblad equation (4.52) is applicable as long as transient behaviours are not of interest. In particular, when studying, e.g. the dynamics of $\rho_{\mathrm{M}}(t)$ in the presence of time-dependent QD level energies $\epsilon_j(t)$, Eq. (4.52) should only be used for very slow (adiabatic) time dependences. For rapidly varying QD level energies, one has go back to the full Lindblad equation for the combined QD-MBS system in Eq. (4.33).

4.2 Dark state stabilisation

This section contains dark state stabilisation protocols for the single-box device in Fig. 4.1. It starts in Sec. 4.2.1 with the case of Pauli operator eigenstates, followed by the stabilisation of a magic state in Sec. 4.2.2. In Sec. 4.2.3, the role of increasing temperature on the stabilisation protocols is examined. Interestingly, as shown in Sec. 4.2.4, one finds that even a finite Majorana state overlap cannot deteriorate the fidelity of certain dark state stabilisation protocols. Finally, in Sec. 4.2.5, the readout dynamics is briefly discussed. Here, the analogy to the native MBQ allows to perform parity readout of the stabilised states in a topologically protected way.

4.2.1 Pauli operator eigenstates

As a starting point for the discussion of the DD protocol, Pauli operator eigenstates are targeted. Typical numerical results obtained by solving Eq. (4.52) are illustrated in Fig. 4.4. Following the method in Sec. 2.5.2, the $Z = \pm 1$ eigenstates can be realised by choosing

$$|\lambda_{11}| = |\lambda_{12}|, \quad \lambda_{21} = \lambda_{22} = 0, \quad \beta_1 - \beta_3 = \pm\pi/2, \tag{4.56}$$

with arbitrary λ_{23} and $\beta_{2,4}$, see Eq. (4.44). Note that for $\lambda_{23} = 0$, the phases $\beta_{2,4}$ are not defined. At this point, it is convenient to use the concept of a *dissipative map* $\hat{E}$ [Breuer, 2006], which is defined in terms of a jump operator mapping the system onto a specific state when acting inside the Lindblad dissipator. For example, the dissipative maps targeting the $Z = \pm 1$ eigenstates are

$$\hat{E}_{\pm} = \sigma_{\pm} = (X \pm iY)/2. \tag{4.57}$$

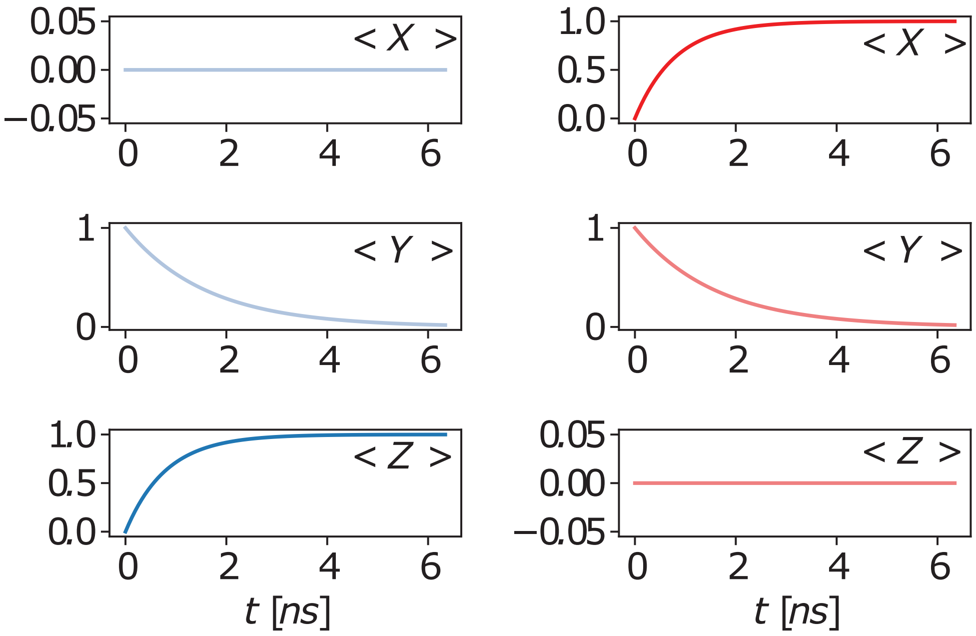

Figure 4.4: Dark-state stabilisation protocols for Pauli operator eigenstates. Left side panels (blue curves): Stabilisation of $|0\rangle$. Right side panels (red curves): Stabilisation of $|+\rangle$, where $X|+\rangle = |+\rangle$. In both cases, the Majorana island has initially been prepared in the Y-eigenstate with eigenvalue $+1$. The parameters were chosen as in Eq. (4.56) with $p = 1/2$, all other parameters are as in Fig. 4.2. With $E_C = 1$ meV and $g_0/E_C = 2.5\times10^{-3}$, the time units follow as shown. As explained in the main text, for the chosen parameter set, Rabi oscillations are absent. [Gau, 2020b]

For the stabilisation parameters in Eq. (4.56), the jump operator $\tilde{J}_+ \propto \hat{E}_\pm$, with the $\pm$ sign determined by Eq. (4.56), completely dominates the Lindbladian part of Eq. (4.52) at low temperatures, $T \ll \omega_0$. The dissipative dynamics then maps every input state to $|0\rangle$ (for the $+$ sign) or $|1\rangle$ (for the $-$ sign). At the same time, the Hamiltonian evolution in Eq. (4.52) originates from $\tilde{H}_{\rm L} \propto Z$, see Eq. (4.54). Evidently, this Hamiltonian commutes with the targeted state $\rho_{\rm M}(\infty)$, and therefore does not affect the dynamics towards the steady state generated by the dissipative map $\hat{E}_\pm$. The Majorana state $\rho_{\rm M}(t)$ is thus automatically steered towards the corresponding Z-eigenstate by the Lindbladian, with no obstruction from the Hamiltonian dynamics.
For the above protocol, the *dissipative gap* is given by, cf. Sec. 2.5.2,

$$\Delta_z = |4\lambda_{11}\lambda_{23}|^2 \sum_{s=\pm} \tilde{\Gamma}_s. \tag{4.58}$$

In general terms, the dissipative gap is defined as the real part of the smallest non-vanishing eigenvalue of the Lindbladian (the dark state itself has eigenvalue zero), see [Breuer, 2006]. The time scale on which the dark state will be approached is therefore given by Δ_z^{-1}. Moreover, the approach of the Bloch vector towards the dark state $|0\rangle$ is, in general, accompanied by damped oscillations in the (X, Y) components, where Δ_z is the damping rate and the Rabi frequency follows from Eq. (4.54) as

$$\Omega_z \simeq \left| 2g_0(1-2p)|\lambda_{11}|^2 - 8|\lambda_{11}\lambda_{23}|^2\tilde{h}_+ \right|. \tag{4.59}$$

For the special case of $\lambda_{21} = 0$ with $p = 1/2$, cf. Sec. 4.1.2, and noting that $\tilde{h}_+ = 0$ for $\alpha = 1/4$, cf. Eq. (4.42), one obtains $\Omega_z = 0$ in Eq. (4.59). The left panels in Fig. 4.4

therefore exhibit only damping in the (X, Y) components, without Rabi oscillations.
Next, $X = \pm 1$ eigenstates are realised by choosing

$$|\lambda_{21}| = |\lambda_{23}|, \quad \lambda_{11} = \lambda_{22} = 0, \quad \beta_2 = \mp\pi/2, \tag{4.60}$$

with the dissipative gap $\Delta_x = |4\lambda_{12}\lambda_{21}|^2 \sum_s \tilde{\Gamma}_s$. As shown in the right panels of Fig. 4.4, X-eigenstates, e.g. the state $|+\rangle$ for eigenvalue $+1$, can be stabilised using the setup in Fig. 4.1. As for the Z-stabilisation shown in the left panels, there are no Rabi oscillations for this parameter set.
Finally, for stabilising the Y-eigenstates with eigenvalue ± 1, one requires

$$|\lambda_{22}| = |\lambda_{23}|, \quad \lambda_{12} = \lambda_{21} = 0, \quad \beta_2 - \beta_3 - \beta_4 = \pm\pi/2, \tag{4.61}$$

with the dissipative gap $\Delta_y = |4\lambda_{11}\lambda_{22}|^2 \sum_s \tilde{\Gamma}_s$.
In all these examples, the target axis (say, $\hat{e}_z$ for Z-eigenstates) is controlled by selecting appropriate tunneling amplitude parameters $\lambda_{j\nu}$. Two links are switched off, and two are matched in amplitude such that the desired jump operator $\tilde{J}_+$ is implemented. For $T \ll \omega_0$, dissipative transitions are fully governed by this jump operator which is due to inelastic cotunneling transitions from QD $2 \to 1$. Under these conditions, $\tilde{H}_{\mathrm{L}}$ commutes with the Pauli operator $\hat{\sigma}$ corresponding to the target axis (e.g., $\hat{\sigma} = Z$ for Z-states). Finally, by adjusting the phases β_j, one can select the stabilised state, say, $|0\rangle$ or $|1\rangle$. It is a remarkable feature of the here discussed Majorana-based DD setup that the Hamiltonian $\tilde{H}_{\mathrm{L}}$ can be engineered to only generate $\hat{\sigma}$. As a consequence, the Lindbladian dissipator already drives the system to the desired dark state.

Stabilising mixed states

Since the phases β_j select the targeted state, one can also use the here discussed protocols for stabilising mixed states. To give an example, one considers changing the above phase conditions such that a mixture of Pauli eigenstates can be prepared as dark state. For instance, by choosing the state design parameters as in Eq. (4.56) but keeping $\bar{\beta} = \beta_1 - \beta_3$ arbitrary, one obtains the dark state

$$\rho_{\mathrm{M}}(\infty) = \frac{1 + \sin\bar{\beta}}{2}|0\rangle\langle 0| + \frac{1 - \sin\bar{\beta}}{2}|1\rangle\langle 1|. \tag{4.62}$$

The relative weight of the two components can then be altered by adjusting the phase difference $\bar{\beta}$.

4.2.2 Magic states

In order to highlight the power of the here discussed DD stabilisation protocols, one might consider the magic state

$$|m\rangle = e^{-i\frac{\pi}{8}Y}|0\rangle. \tag{4.63}$$

The practical importance of this state comes from the fact that a large number of ancilla qubits approximately prepared in the state $|m\rangle$ are needed for the magic state distillation protocol. The latter is an essential ingredient for implementing the T-gate required for universal surface code quantum computation, cf. Sec.2.4.1. Targeting $|m\rangle$, the stabilisation conditions now involve all tunnel links in Fig. 4.1 but one and are given by

$$|\lambda_{12}| = |\lambda_{23}|, \quad |\lambda_{21}| = |\lambda_{11}| = |\lambda_{23}|/\sqrt{2}, \quad \lambda_{22} = 0, \quad \beta_3 = \beta_1 + \beta_2, \quad \beta_2 = -\pi/2. \tag{4.64}$$

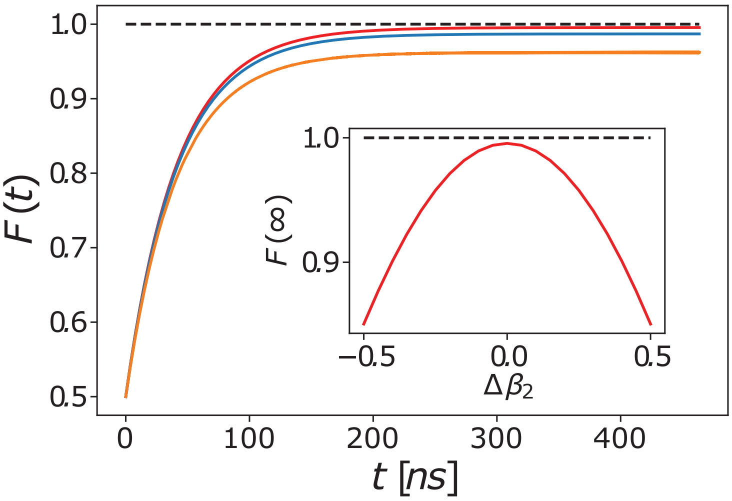

Figure 4.5: Fidelity for a stabilisation protocol targeting the magic state $|m\rangle$. Here, the Majorana state follows from numerical integration of Eq. (4.52) using the parameters in Eq. (4.64) with $|\lambda_{23}| = 1$. Other parameters are $E_C = 1$ meV, $g_0/E_C = 2.5 \times 10^{-3}$, $T/g_0 = 4$, $\omega_0/g_0 = 40$, $\omega_c/g_0 = 200$, $\alpha = 1/4$, and $p = 0.01$. Main panel: Time dependence of the fidelity for ideal parameters [Eq. (4.64)] (red curve), with a mismatch of order 10% in all state design parameters [$|\lambda_{11}| = -0.1 + 1/\sqrt{2}, |\lambda_{21}| = +0.1 + 1/\sqrt{2}, |\lambda_{12}| = |\lambda_{22}| = 0.9, \beta_3 = -\beta_2 = 11\pi/20$] (blue), and a mismatch of order 20% in the same parameters (orange). Inset: Steady-state fidelity vs deviation $\Delta\beta_2$ with otherwise ideal parameters, where $\beta_2 = -\frac{\pi}{2}(1 + \Delta\beta_2)$. [Gau, 2020b]

In analogy to Sec. 4.2.1 one can understand the state design parameters according to their effect on the jump operator. As the targeted state $|m\rangle$ is obtained by a $\frac{\pi}{4}$-rotation of $|0\rangle$ around the y-axis, its Bloch vector lies inside the x-z-plane of the Bloch sphere. Thus, the required dissipative map is a superposition of all three Pauli operators, which in turn implies that only λ_{22} can be switched off for convenience, cp. Eq. (4.43). Moreover two amplitudes are matched to guarantee equal contribution to the unidirectional process implementing the dissipative map. Finally, decreasing the remaining amplitudes by a factor of $1/\sqrt{2}$ with respect to the matched links ensures that the targeted axis is precisely the diagonal of the x-z-plane. Since the dark state is more complex compared to Pauli eigenstates, all remaining phases β_j have to be adjusted to target $|m\rangle$. Note that for $\beta_2 = +\pi/2$ the other magic state, obtained by a $\frac{\pi}{4}$-rotation of $|1\rangle$ around the y-axis, can be stabilised.

To quantify the power of the here discussed DD protocol one can define the *fidelity* of the state $\rho_{\mathrm{M}}(t)$ with respect to a specific pure state, $\rho_{\mathrm{M}}^{(0)} = |\psi\rangle\langle\psi|$, as

$$F(t) = \mathrm{tr}\left[|\psi\rangle\langle\psi|\rho_{\mathrm{M}}(t)\right]. \tag{4.65}$$

Numerical results for the magic state fidelity with $|\psi\rangle = |m\rangle$ are shown in Fig. 4.5, using the parameters in Eq. (4.64). One finds $F = 1$ at long times for the ideal parameter choice in Eq. (4.64). Figure 4.5 also illustrates the long-time fidelity when allowing for small deviations from Eq. (4.64), which are inevitable in practical implementations. Remarkably, even for sizeable deviations from the ideal parameter set, the fidelity remains close to unity. By determining the spectrum of the Lindbladian, one obtains the dissipative gap as

$$\Delta_m = |4\lambda_{11}\lambda_{23}|^2 \sum_s \tilde{\Gamma}_s. \tag{4.66}$$

Using the parameters in Fig. 4.5, one finds $\Delta_m^{-1} \simeq 80$ ns. Even though the here discussed magic state stabilisation protocol requires more parameter fine tuning than the stabilisation of $|0\rangle$, the dark state $|m\rangle$ is reached on essentially the same time scale.

4.2.3 Effect of temperature

Next, one can address the effect of raising temperature within the conditions set by Eq. (4.31), in particular $T \ll \omega_0$. Figure 4.6 shows numerical results for the T-dependent steady state fidelity $F(\infty)$ with respect to the states $|0\rangle$ and $|m\rangle$, choosing ideal parameters as in Eqs. (4.56) and (4.64), respectively. Since the transition rates in Eq. (4.42) are the same for all targeted single qubit states, i.e. they do not depend on the state design parameters, the here discussed effect of temperature is the same for all DD stabilisation protocols.

At very low temperatures, the fidelity stays very close to the ideal value ($F = 1$), since here only the rate $\tilde{\Gamma}_+$, see Eqs. (4.35) and (4.53), is significant. In this limit, corrections to $F = 1$ are exponentially small and appear to be governed by the dissipative gap, $1 - F \propto \exp(-\Delta_{z/m}/T)$. The same scaling behaviour also applies to the purity. As temperature increases, the thermal excitation rate $\tilde{\Gamma}_- = e^{-\omega_0/T}\tilde{\Gamma}_+$ cannot be neglected anymore. Focusing on the stabilisation of the state $|0\rangle$, one has $\tilde{J}_- \propto \sigma_-$. The Lindblad dissipator $\tilde{\Gamma}_-\mathcal{D}[\tilde{J}_-]$ will then target the 'wrong' Z-eigenstate $|1\rangle$. The competition between $\mathcal{D}[\tilde{J}_+]$ and $\mathcal{D}[\tilde{J}_-]$ implies that the fidelity will deteriorate as temperature increases.

This expectation is confirmed by numerical results. For the parameters in Fig. 4.6, the fidelity noticeably drops once T exceeds the crossover temperature $T_c \approx 250$ mK. Figure 4.6 also shows the temperature dependent purity of the steady state, $P(\infty) = \mathrm{tr}\rho_{\mathrm{M}}^2(t \to \infty)$. For $T \ll T_c$, one finds $P(\infty) \simeq 1$. As T increases, however, the maximally mixed state $\rho_{\mathrm{M}}(\infty) = \frac{1}{2}\mathbb{I}$ with $F(\infty) = P(\infty) = 1/2$ is approached, and consequently the purity also becomes smaller.

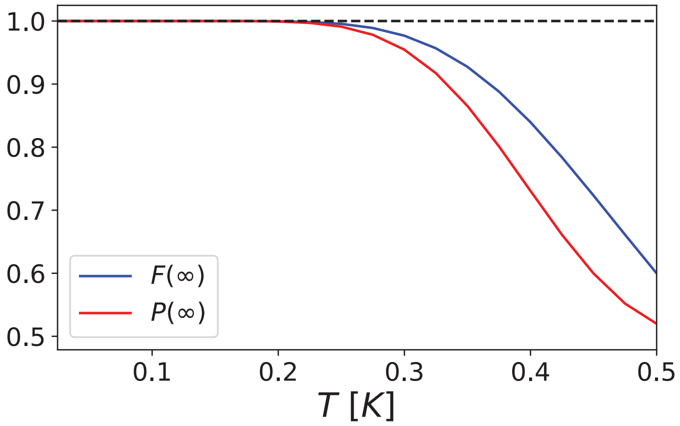

Figure 4.6: Steady-state fidelity, $F(\infty)$, and purity, $P(\infty)$, vs temperature (in Kelvin) for the state $|0\rangle$ and for the magic state $|m\rangle$. Ideal state design parameters, see Eqs. (4.56) and (4.64), are used with all other parameters as in Figs. 4.4 and 4.5, respectively. The numerical results for both states cannot be distinguished for these parameter choices on the shown scales. The frequency ω_0 corresponds to a temperature of ≈ 2.5 K. [Gau, 2020b]

4.2.4 Majorana hybridisation

So far, the overlap between different MBSs was assumed to be negligibly small. Here, an estimate of the effects of a finite (but small) hybridisation between different MBS pairs on the above stabilisation protocols is given. Such terms could arise, e.g. due to the finite nanowire length [Alicea, 2012]. They are described by a Hamiltonian term

$$\mathcal{H}' = \sum_{\nu<\nu'} i\epsilon_{\nu\nu'}\gamma_\nu\gamma_{\nu'}, \tag{4.67}$$

with hybridisation energies $\epsilon_{\nu\nu'}$. By construction, the above term survives the RWA and the Schrieffer-Wolff projection in Sec. 4.1 and thus contributes to the Hamiltonian $\tilde{H}_\mathrm{L}$ in the Lindblad equation (4.52) without affecting the Lindbladian dissipator. In the Pauli operator language, such terms act like a weak magnetic Zeeman field. If the corresponding field is parallel to the target axis of the dark state, it does not cause any dephasing. For instance, for the stabilisation of the Z-eigenstate $|0\rangle$, the hybridisation parameters ϵ_{12} and ϵ_{34} can be tolerated since they only couple to the Pauli operator Z in Eq. (4.2). Clearly, such couplings have no detrimental effects on the stabilisation protocols.

4.2.5 Readout dynamics

In order to read out a stabilised dark state, it is possible to use the same techniques suggested previously for the native Majorana qubit, see Sec. 2.4.2. In particular, one can perform capacitance spectroscopy using additional single-level QDs that are tunnel-coupled to MBS pairs. These QDs are used for measurements only, where the spectroscopic signal contains an interference term, cf. Eq. (2.67), which depends on the respective Pauli matrix in Eq. (4.2). This projective readout yields the Pauli eigenvalue ±1 with a state-dependent probability [Karzig, 2017]. Of course, this method can also be used to prepare the Majorana island in a Pauli eigenstate before the DD protocol is started.

In order for the readout not to interfere with the DD stabilisation protocol, one has to make sure that the characteristic projective measurement time scale (see [Plugge, 2017] and [Karzig, 2017] for detailed expressions) is much longer than the typical inelastic cotunneling time $\tilde{\Gamma}_+^{-1}$. Similarly, single-electron pumping protocols via a pair of QDs attached to different MBSs allow one to apply a Pauli operator to the tetron state in a topologically protected manner, see Sec. 2.4.3.

4.2.6 On the uniqueness of the dark state

So far, DD stabilisation protocols targeting a desired dark state were discussed. The dark space dimension for those protocols should therefore be $D = 1$, see Sec. 2.5.3, which corresponds to the steady-state solution being unique. As stabilisations of different dark states are linked to each other by adiabatically changing the state design parameters, it suffices to discuss the dark space dimension for a single protocol. One of the simplest examples is given by the $Z = \pm 1$ stabilisation in Sec. 4.2.1. Here the Hamiltonian is given by $H_\mathrm{L} \propto Z$ and the Lindbladian dissipator reads $\mathcal{D}[\sigma_\pm]\,\rho_\mathrm{M}(t)$. In Sec. 2.5.3, this Lindbladian was discussed in terms of its conserved quantities, which lead to $D = 1$. Since there is a unique dark state for a given choice of the state design parameters, one could utilise a DD single-box device as a self-correcting quantum memory. By means of adiabatic changes of the state design parameters, one can steer the Majorana state on its Bloch sphere. However, for general state manipulation protocols, it is advantageous to have access to a dark space manifold with $D > 1$, which may be engineered in systems with more than four MBSs. This case is addressed in the next section.

4.3 Dark space engineering

This section is dedicated to minimal DD Majorana box systems necessary for stabilising not a dark state, but a dark space. Such a degenerate manifold of dark states may be engineered by employing a device with at least two Majorana boxes as depicted in Fig. 4.7. After introducing the model and the corresponding Lindblad equation in Sec. 4.3.1, the main idea of implementing dissipative maps is emphasised. As first demonstration of the robustness of the DD two-box system, Sec. 4.3.2 includes the stabilisation of Bell states. Finally, Sec. 4.3.3 provides details on an alternative architecture, the hexon device, which allows for the stabilisation of Bell states on shorter time scales compared to the two Majorana box system in Fig. 4.7.

4.3.1 Lindblad equation for two coupled boxes

Following the discussion in Sec. 4.1.1, the two islands in Fig. 4.7 are described by $\mathcal{H}_{\text{box}} = \mathcal{H}_{\text{box},L} + \mathcal{H}_{\text{box},R}$, with $\mathcal{H}_{\text{box},L/R}$ as in Eq. (4.1). Here, the four MBSs on the left (right) box correspond to Majorana operators γ_ν^L (γ_ν^R). Both islands are separately operated under Coulomb valley conditions. For notational simplicity, one may assume that they have the same charging energy, $E_{C,L} = E_{C,R} = E_C$. Focussing on the long-wavelength components of the electromagnetic environment, one again works with a single bosonic bath, $\mathcal{H}_{\text{env}} = \sum_m E_m b_m^\dagger b_m$, where photons couple to the QDs and MBSs via fluctuating phases, θ_j, in the tunneling Hamiltonian, see Sec. 4.1.1. The setup in Fig. 4.7 requires up to three single-level QDs, $\mathcal{H}_{\text{d}} = \sum_{j=1}^{3} \epsilon_j d_j^\dagger d_j$, where QD 3 couples to both other QDs via independently driven tunnel links. Considering the regime $N_{\text{d}} = 1$, where on time scales $\delta t > 1/E_C$, the three QDs share a single electron.
Using the interaction picture with respect to the dot Hamiltonian $\mathcal{H}_{\text{d}}$, the full Hamiltonian is then given by

$$\mathcal{H}(t) = \mathcal{H}_{\text{box}} + \mathcal{H}_{\text{env}} + \mathcal{H}_{LR} + \mathcal{H}_{\text{drive}}(t) + \mathcal{H}_{\text{tun}}(t), \tag{4.68}$$

where a phase-coherent tunnel link couples the boxes. Without loss of generality, one assumes a real-valued tunneling amplitude $t_{LR} > 0$,

$$\mathcal{H}_{LR} = it_{LR}\gamma_4^L\gamma_2^R. \tag{4.69}$$

The drive Hamiltonian now has the form

$$\mathcal{H}_{\text{drive}}(t) = \sum_{j=1,2} 2A_j \cos(\omega_j t)\, e^{i(\epsilon_j - \epsilon_3)} d_j^\dagger d_3 + \text{h.c.}, \tag{4.70}$$

where the two driving fields have the respective amplitude $A_{1,2}$ and frequency $\omega_{1,2}$. In analogy to Eq. (4.7), the QD-MBS tunnel links are described by

$$\mathcal{H}_{\text{tun}}(t) = t_0 \sum_{j\nu,\kappa=L/R} \lambda_{j,\nu\kappa} e^{-i\phi_\kappa} e^{i\theta_j} e^{i\epsilon_j t} d_j^\dagger \gamma_\nu^\kappa + \text{h.c.}, \tag{4.71}$$

with the phase operators $\phi_{L/R}$ for the left/right Majorana island. Using the same approximations as in Sec. 4.1.1, the electromagnetic environment enters Eq. (4.71) through the

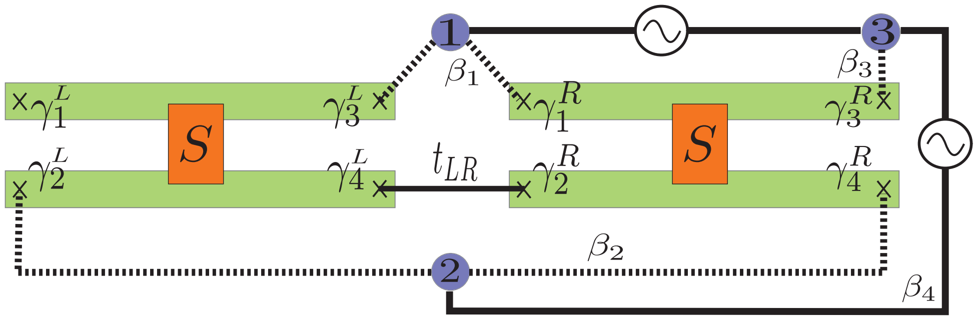

Figure 4.7: Schematic two-box layout for DD dark space stabilisation and manipulation protocols, cp. Fig. 4.1 for the single-box case. The left (right) box harbours four MBSs described by γ_ν^L (γ_ν^R). The tunneling bridge with amplitude t_{LR} connects γ_4^L and γ_2^R. QD 3 has independently driven tunneling bridges to QD 1 and to QD 2 (solid lines). The three QDs are operated in the single-electron regime, $N_\mathrm{d} = 1$. The electromagnetic environment affects the phases of the tunnel links betweens QDs and MBSs (dashed lines). The phases β_j for this geometry are also indicated. [Gau, 2020b]

fluctuating phases θ_j. With the overall energy scale t_0, the complex-valued parameters $\lambda_{j,\nu\kappa}$ parametrise the transparency of the tunnel contact between d_j and $\gamma_\nu^{\kappa=L/R}$. Similar to Eq. (4.44), the phases β_j in Fig. 4.7 follow from the phases of these parameters. Since β_4 can be absorbed by a renormalisation of β_3 for the purposes below, one can put $\beta_4 = 0$. To simplify the presentation, one can assume for QDs 1 and 2 to have the same energy level, $\epsilon_1 = \epsilon_2$. Moreover, one considers the case of equal drive frequencies, $\omega_1 = \omega_2 \equiv \omega_0$, and identical drive amplitudes, $A_1 = A_2 \equiv A$, and again impose a resonance condition, $\omega_0 = \epsilon_3 - \epsilon_1$. However, in analogy to the discussion in Sec. 4.1.1, one expects that overly precise fine tuning with respect to those conditions is not necessary.

Proceeding with the construction of an effective low-energy model, a Schrieffer-Wolff transformation to the lowest-energy charge state in each box is performed. One can then define Pauli operators $(X_\kappa, Y_\kappa, Z_\kappa)$ with $\kappa = L, R$ referring to the left and right box, respectively, using the Majorana representation

$$X_\kappa = i\gamma_1^\kappa\gamma_3^\kappa, \quad Y_\kappa = i\gamma_3^\kappa\gamma_2^\kappa, \quad Z_\kappa = i\gamma_1^\kappa\gamma_2^\kappa. \tag{4.72}$$

In the present case, it is crucial to keep all terms up to third order in the expansion parameters (4.9) when accounting for cotunneling trajectories connecting pairs of QDs, cf. Fig. 4.7. Note that for the single-box case in Sec. 4.1, it was sufficient to go to second order only. The electromagnetic environment then enters the low-energy theory via the three phase differences $\theta_j - \theta_k$ with $j < k$. This fact implies that, in general, one has six different spectral densities $\mathcal{J}_{jk;j'k'}(\omega)$. One models these spectral densities by the Ohmic form in Eq. (4.22), with system-bath couplings $\alpha_{jk;j'k'}$. For simplicity, one can employ an average value α for these couplings below. The bath is then described by a single spectral density $\mathcal{J}(\omega)$ again. It is important to note that the physics is not changed by this approximation. In particular, no additional jump operators appear when allowing for different $\alpha_{jk;j'k'}$.

Considering the weak driving regime with $T \ll \omega_0$, one can proceed along similar steps as in Sec. 4.1.2, and thereby obtain a Lindblad master equation for the density matrix, $\rho(t)$, describing both the Majorana sector and the QD degrees of freedom. In order to arrive at a Lindblad equation for the reduced density matrix, $\rho_\mathrm{M}(t)$, which refers only to the Majorana sector of both boxes, one next traces over the QD subsector, see Sec. 4.1.3.

For the QD steady-state density matrix, ρ_{d}, one uses the *Ansatz*

$$\rho_{\mathrm{d}} = \mathrm{diag}\left(\frac{1-p}{2}, \frac{1-p}{2}, p\right), \tag{4.73}$$

expressed in the basis $\{|100\rangle, |010\rangle, |001\rangle\}$ with QD occupation states $|n_1, n_2, n_3\rangle$ for $N_{\mathrm{d}} = 1$. Note that since $\epsilon_1 = \epsilon_2$ was assumed, the occupation probabilities of QDs 1 and 2 are equal. The occupation probability $0 < p \ll 1$ refers to the energetically highest QD 3. Equation (4.73) is consistent with numerical analysis of the Lindblad equation for $\rho(t)$, where one again finds a factorised density matrix at long times, $\rho(t) \simeq \rho_{\mathrm{M}}(t) \otimes \rho_d$. Furthermore, the dark space turns out to be independent of the concrete value of p.
Going through the corresponding steps in Sec. 4.1.3, one arrives at a Lindblad equation for $\rho_{\mathrm{M}}(t)$,

$$\partial_t \rho_{\mathrm{M}}(t) = -i[\tilde{H}_{\mathrm{L}}, \rho_{\mathrm{M}}(t)] + \sum_{a=1}^{6} \tilde{\Gamma}_a \mathcal{L}[K_a]\rho_{\mathrm{M}}(t). \tag{4.74}$$

The six jump operators are denoted by K_a, with the respective dissipative transition rates $\tilde{\Gamma}_a$. With $\lambda_{LR} \equiv t_{LR}/E_C \ll 1$, one obtains

$$\begin{aligned}
K_1 = K_4^\dagger &= ie^{i(\beta_3-\beta_1)}\frac{|\lambda_{1,1R}\lambda_{3,3R}|}{\lambda_{LR}} X_R - e^{i\beta_3}|\lambda_{1,3L}\lambda_{3,3R}| Z_L Y_R,\\
K_2 = K_5^\dagger &= -ie^{i(\beta_3-\beta_2)}\frac{|\lambda_{2,4R}\lambda_{3,3R}|}{\lambda_{LR}} Z_R + e^{i\beta_3}|\lambda_{2,2L}\lambda_{3,3R}| X_L Y_R,\\
K_3 = K_6^\dagger &= i\frac{|\lambda_{1,3L}\lambda_{2,2L}|}{\lambda_{LR}} Y_L - ie^{i(\beta_2-\beta_1)}\frac{|\lambda_{1,1R}\lambda_{2,4R}|}{\lambda_{LR}} Y_R\\
&\quad + e^{-i\beta_1}|\lambda_{1,1R}\lambda_{2,2L}|\, X_L Z_R - e^{i\beta_2}|\lambda_{1,3L}\lambda_{2,4R}|\, Z_L X_R.
\end{aligned} \tag{4.75}$$

The coherent evolution in Eq. (4.74) is governed by the Hamiltonian

$$\tilde{H}_{\mathrm{L}} = 2p\tilde{g}_0 K_z + \sum_{a=1}^{6} \tilde{h}_a K_a^\dagger K_a, \tag{4.76}$$

with the operator

$$K_z = \sin\beta_1 |\lambda_{1,1R}\lambda_{1,3L}| Z_L Z_R + \sin\beta_2 |\lambda_{2,2L}\lambda_{2,4R}| X_L X_R. \tag{4.77}$$

Here, the energy scale

$$\tilde{g}_0 = \lambda_{LR} g_0 = \frac{t_0^2 t_{LR}}{E_C^2} \tag{4.78}$$

was used, which characterises the relevant inelastic cotunneling processes in the double-box setup. The transition rates $\tilde{\Gamma}_a$ follow in the form

$$\begin{aligned}
\tilde{\Gamma}_1 = \tilde{\Gamma}_2 &= 2p\tilde{g}_0^2 \,\mathrm{Re}\int_0^\infty dt e^{i\omega_0 t} e^{J_{\mathrm{env}}(t)},\\
\tilde{\Gamma}_3 = \tilde{\Gamma}_6 &= (1-p)\tilde{g}_0^2 \,\mathrm{Re}\int_0^\infty dt e^{J_{\mathrm{env}}(t)},\\
\tilde{\Gamma}_4 = \tilde{\Gamma}_5 &= \frac{(1-p)}{2p} e^{-\omega_0/T}\tilde{\Gamma}_1,
\end{aligned} \tag{4.79}$$

and the Lamb shifts $\tilde{h}_a$ are given by

$$\tilde{h}_1 = \tilde{h}_2 = p\tilde{g}_0^2 \,\mathrm{Im}\int_0^\infty dt e^{i\omega_0 t} e^{J_{\mathrm{env}}(t)},$$

$$\begin{aligned}\tilde{h}_3 = \tilde{h}_6 &= \frac{1}{2}(1-p)\tilde{g}_0^2 \operatorname{Im}\int_0^\infty dt e^{J_{\mathrm{env}}(t)}, \\ \tilde{h}_4 = \tilde{h}_5 &= \frac{(1-p)}{2p} e^{-\omega_0/T}\tilde{h}_1.\end{aligned} \tag{4.80}$$

For $\omega_0 \ll \omega_c$, one can then make further analytical progress. Explicit expressions for $\tilde{\Gamma}_{1,2}$ and $\tilde{h}_{1,2}$ follow by comparison with Eq. (4.42). In addition, one finds

$$\begin{aligned}\tilde{\Gamma}_{3,6} &\simeq (1-p)\frac{\cos(\pi\alpha)\Gamma(\alpha)\Gamma(1-2\alpha)}{2^{1-2\alpha}\Gamma(1-\alpha)}\left(\frac{\pi T}{\omega_c}\right)^{2\alpha-1}\frac{2\tilde{g}_0^2}{\omega_c}, \\ \tilde{h}_{3,6} &= -\frac{1}{2}\tan(\pi\alpha)\tilde{\Gamma}_{3,6}.\end{aligned} \tag{4.81}$$

By following the derivation of the reduced master equation (4.74), one observes that the operator K_1 (K_2) originates from unidirectional transitions transferring an electron from the energetically high-lying QD 3 to QD 1 (QD 2) via the double-box setup, collecting all possible cotunneling trajectories allowed by third-order perturbation theory. Likewise, the jump operator K_4 (K_5) describes the reversed process, with a cotunneling transition from QD 1 (QD 2) to QD 3. For $T \ll \omega_0$, the transition rates $\tilde{\Gamma}_{4,5}$ and Lamb shifts $\tilde{h}_{4,5}$ are exponentially suppressed, $\propto e^{-\omega_0/T}$, against the respective contributions from $K_{1,2}$. Moreover, the jump operators K_3 and K_6 in Eq. (4.75) describe cotunneling transitions between QDs 1 and 2. Since these QDs are not directly connected by a driven tunnel link and have the same energy, $\epsilon_1 = \epsilon_2$, the corresponding rates and Lamb shifts coincide, $\tilde{\Gamma}_3 = \tilde{\Gamma}_6$ and $\tilde{h}_3 = \tilde{h}_6$. Importantly, for $1/2 < \alpha < 1$, these quantities are reduced by a factor $(T/\omega_0)^{2\alpha-1} \ll 1$ against $\tilde{\Gamma}_{1,2}$ and $\tilde{h}_{1,2}$, respectively. In the remainder of this section, this parameter regime is studied, where the most important jump operators in Eq. (4.74) are given by K_1 and K_2. Nonetheless, one retains the other jump operators in the numerical analysis as well.

Finally, note that all terms without the factor $\lambda_{LR}^{-1} \gg 1$ in Eqs. (4.75) and (4.77) stem from third-order processes. While one *a priori* expects that the corresponding dissipative terms in Eq. (4.74) are suppressed against second-order contributions, by careful tuning of the link transparencies $\lambda_{j,\nu\kappa}$, they can become of comparable magnitude. As a consequence, all relevant cotunneling paths will then have amplitudes corresponding to third-order processes. This means that for the present two-box setup, the energy scale $g_0 = t_0^2/E_C$ appearing in Eq. (4.31) has to be replaced by $\tilde{g}_0$ in Eq. (4.78). The Lindblad equation (4.74) describing the weak driving limit is therefore valid under the conditions

$$\tilde{g}_0 \ll T \ll \omega_0, \quad A \leq \tilde{g}_0. \tag{4.82}$$

Dissipative maps

Before entering the discussion of stabilisation protocols for the layout in Fig. 4.7, it is convenient to introduce the dissipative maps [Barreiro, 2011]

$$\hat{E}_{1,\pm} = (\mathbb{I} \pm Z_L Z_R)X_R, \quad \hat{E}_{2,\pm} = (\mathbb{I} \pm X_L X_R)Z_R. \tag{4.83}$$

These maps can be used to target the four Bell states,

$$|\psi_\pm\rangle = \frac{1}{\sqrt{2}}(|00\rangle \pm |11\rangle), \quad |\phi_\pm\rangle = \frac{1}{\sqrt{2}}(|01\rangle \pm |10\rangle), \tag{4.84}$$

which are eigenstates of both $Z_L Z_R = \pm 1$ and $X_L X_R = \pm 1$. One observes that $\hat{E}_{1,-}$ maps even-parity onto the respective odd-parity states, $\hat{E}_{1,-}|\psi_\pm\rangle = |\phi_\pm\rangle$, while odd-parity states do not evolve in time, $\hat{E}_{1,-}|\phi_\pm\rangle = 0$. Under this dissipative map, the system will thus be driven into the degenerate odd-parity subsector spanned by the $|\phi_\pm\rangle$ states. Similarly, $\hat{E}_{2,-}$ can drive the system into the antisymmetric subsector spanned by $|\phi_-\rangle$ and $|\psi_-\rangle$. The key idea in the DD protocols discussed below is to identify state design parameters such that the jump operators effectively realise the needed dissipative map(s) in Eq. (4.83). Recalling that a dissipative map breaks a number of conserved quantities (and therefore symmetries) in an open quantum system, see Refs. [Albert, 2014, Albert, 2016] and Sec. 2.5.3, one here employs this insight to either stabilise protected and maximally entangled two-qubit dark states, see Sec. 4.2.2, or to stabilise a dark space, see Sec. 4.3.

4.3.2 Bell state stabilisation

Next, the stabilisation of Bell states is discussed, where the minimal system is sketched in Fig. 4.7. Therefore, all six jump operators in Eq. (4.74) are present. In the low temperature regime, the Lindbladian term corresponding to K_2 contributes with the same transition rate, $\tilde{\Gamma}_2 = \tilde{\Gamma}_1$, as for K_1, see Eq. (4.79). Importantly, K_1 and K_2 break different conservation laws and thereby allow one to engineer stabilisation protocols targeting maximally entangled two-qubit states.

Starting with the Bell singlet state $|\phi_-\rangle$ in Eq. (4.84), where $Z_L Z_R = -1$ and $X_L X_R = -1$, one can choose the state design parameters as

$$\beta_1 = -\pi, \quad \beta_2 = 0, \quad \beta_3 = -\pi/2, \quad |\lambda_{1,1R}| = \lambda_{LR}|\lambda_{1,3L}|, \quad |\lambda_{2,4R}| = \lambda_{LR}|\lambda_{2,2L}|. \tag{4.85}$$

From Eq. (4.75), one observes that $K_1 \propto \hat{E}_{1,-}$ and $K_2 \propto \hat{E}_{2,-}$ are directly expressed in terms of the corresponding dissipative maps, see Eq. (4.83). The Lindbladian will therefore drive the system to the dark state $|\phi_-\rangle$. The dark space dimension is thus given by $D = 1$.

As shown in Fig. 4.8, the numerical solution of Eq. (4.74) confirms this expectation. For the stabilisation parameters in Eq. (4.85), the Bell singlet state is reached with nearly perfect fidelity when taking ideal parameter values. One can rationalise this by noting that the coherent evolution due to $\tilde{H}_\mathrm{L}$, see Eq. (4.76), involves only the operators $Z_L Z_R$ and $X_L X_R$. As a consequence, the dynamics induced by the dissipative maps $K_{1,2} \propto \hat{E}_{1/2,-}$ will not be disturbed. Note that the parameters in Fig. 4.8 were chosen such that $\tilde{\Gamma}_1 \gg \tilde{\Gamma}_3$ while staying in the regime specified in Eq. (4.82). Indeed, the observed small deviations from the ideal value $F = 1$, see Fig. 4.8, can be traced back to the jump operators K_3 and K_6, which give nominally subleading but practically important contributions to the Lindblad equation.

Figure 4.8 shows that the stabilisation protocol is rather robust against deviations of state design parameters from their ideal values in Eq. (4.85), see Sec. 4.2. Following the approach in Sec. 2.5.2, one finds that the dissipative gap for stabilising $|\phi_-\rangle$ is given by

$$\Delta_\mathrm{Bell} = |2\lambda_{3,3R}|^2 \left(|\lambda_{1,3L}|^2 + |\lambda_{2,2L}|^2\right) \sum_{a=1,2,4,5} \tilde{\Gamma}_a. \tag{4.86}$$

Due to the importance of third-order inelastic cotunneling processes, this dissipative gap is several orders of magnitude below the corresponding gaps in the single-box case, cf. Sec. 4.2. For the parameters in Fig. 4.8, one obtains the time scale $\Delta_\mathrm{Bell}^{-1} \approx 0.3$ ms.

The other Bell states in Eq. (4.84) can be targeted by changing the phases β_j in Eq. (4.85). The jump operators K_1 and K_2 will then directly implement the desired dissipative maps, with the dissipative gap still given by Eq. (4.86). For stabilisation of the Bell state $|\psi_+\rangle$

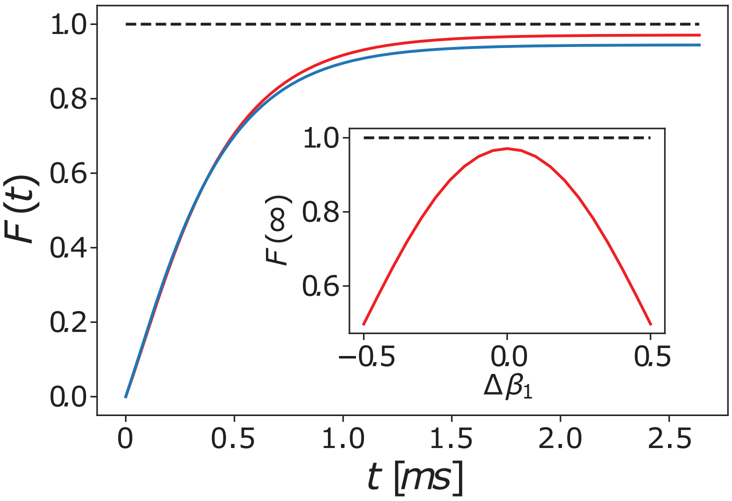

Figure 4.8: Fidelity for stabilising the Bell singlet state $|\phi_-\rangle$ in the setup of Fig. 4.7. Numerical results are shown, which are obtained from Eq. (4.74) with the parameters in Eq. (4.85) and $|\lambda_{1,3L}| = |\lambda_{2,2L}| = |\lambda_{3,3R}| = 1$, using the initial state $\rho_\mathrm{M}(0) = |00\rangle\langle 00|$. Other parameters are $E_C = 1$ meV, $\tilde{g}_0/E_C = 10^{-5}$, $T/\tilde{g}_0 = 2, \omega_0/\tilde{g}_0 = 2\times 10^3, \omega_c/\tilde{g}_0 = 10^4, \alpha = 0.99$, and $p = 0.01$. Main panel: Time dependence of $F(t)$ for ideal parameters [Eq. (4.85)] (red curve), and for a mismatch of order 10% in all state design parameters [$|\lambda_{1,1R}| = 1.1\lambda_{LR}|\lambda_{1,3L}|$, $|\lambda_{2,4R}| = 0.9\lambda_{LR}|\lambda_{2,2L}|$, $\beta_1 = -1.1\pi$, $\beta_3 = -9\pi/20$] (blue). Inset: Steady-state fidelity vs deviation $\Delta\beta_1$ from the ideal value, i.e., $\beta_1 = -\pi(1+\Delta\beta_1)$, with otherwise ideal parameters. [Gau, 2020b]

($|\psi_-\rangle$), one has to put $\beta_1 = 0$, $\beta_2 = \pi$ ($\beta_2 = 0$), and $\beta_3 = \pi/2$. Similarly, $|\phi_+\rangle$ is stabilised for $\beta_1 = -\pi, \beta_2 = \pi$, and $\beta_3 = -\pi/2$. One thus always has $\beta_3 - \beta_1 = \pi/2$, and the remaining two phases select the targeted Bell state. In particular, β_1 selects the parity of the target state while β_2 determines the symmetric vs antisymmetric state.

4.3.3 Alternative setup: the DD hexon

Instead of the DD two-box setup in Fig. 4.7, one can also work with the hexon architecture in Fig. 4.9, where a single Coulomb-blockaded topological superconductor island harbours six MBSs. The island has the charging energy E_C and is again operated under Coulomb valley conditions. It then harbours two Majorana qubits, see Sec. 2.2.2. A major advantage of the hexon architecture over the two-box setup in Fig. 4.7 is that one can formulate simpler and faster stabilisation protocols obviating the need for third-order cotunneling processes and the associated fine-tuned balancing of tunneling amplitudes. In any case, the methodological and conceptual steps discussed above apply for the hexon case as well.

For the modelling of the device in Fig. 4.9, one thus proceeds as in Sec. 4.1. In the interaction picture with respect to $\mathcal{H}_d + \mathcal{H}_\mathrm{env}$, the Hamiltonian is given by $\mathcal{H}(t) = \mathcal{H}_\mathrm{Box} + \mathcal{H}_\mathrm{drive}(t) + \mathcal{H}_\mathrm{tun}$, with the drive Hamiltonian in Eq. (4.30). One again assumes $\epsilon_1 = \epsilon_2$, $A_1 = A_2$, and $\omega_{1,2} = \omega_0 = \epsilon_3 - \epsilon_1$, cf. Sec. 4.3.1. Instead of Eq. (4.71), the inelastic tunneling Hamiltonian again takes the generic form, cf. Eq. (4.7). Here, in contrast to the two-box device, only one charge-conjugated phase ϕ exists.

In the low-energy sector, charge quantisation on the box implies the overall Majorana parity constraint $\gamma_1\gamma_2\gamma_3\gamma_4\gamma_5\gamma_6 = \pm i$. The island then hosts two Majorana qubits ($j = 1,2$) with the Pauli operators (X_j, Y_j, Z_j) encoded by bilinears of the six Majorana operators,

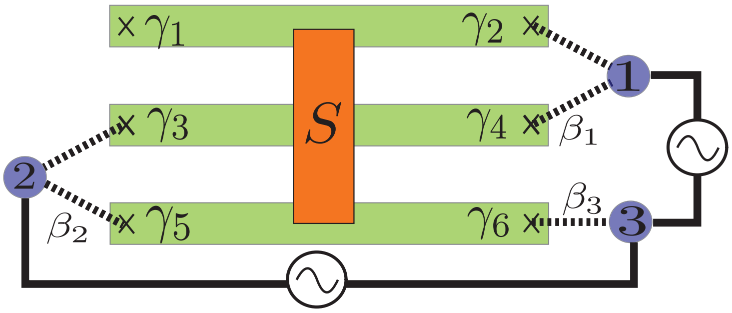

Figure 4.9: Sketch of a DD hexon setup with three single-level QDs and six MBSs described by γ_ν. QD 3 has independently driven tunneling bridges to QD 1 and to QD 2 (solid lines). The three QDs are operated in the single-electron regime, $N_d = 1$. The electromagnetic environment affects the phases of the tunnel links between QDs and MBSs (dashed lines).

cf. Sec. 2.2.2,

$$\begin{aligned} X_1 &= i\gamma_1\gamma_2, \quad Y_1 = i\gamma_2\gamma_3, \quad Z_1 = i\gamma_1\gamma_3 \\ X_2 &= i\gamma_4\gamma_6, \quad Y_2 = i\gamma_4\gamma_5, \quad Z_2 = i\gamma_5\gamma_6. \end{aligned} \tag{4.87}$$

The subsequent steps leading to the Lindblad master equation for the dynamics of the reduced density matrix, $\rho_{\mathrm{M}}(t)$, describing the two Majorana qubits in Eq. (4.87) are as before. One obtains

$$\partial_t \rho_{\mathrm{M}}(t) = -i\left[\tilde{H}_{\mathrm{L}}, \rho_{\mathrm{M}}(t)\right] + \sum_{a=1}^{6} \bar{\Gamma}_a \mathcal{D}\left[L_a\right]\rho_{\mathrm{M}}(t), \tag{4.88}$$

with the jump operators

$$\begin{aligned} L_1 &= L_4^\dagger = ie^{i(\beta_3-\beta_1)}|\lambda_{14}\lambda_{36}|X_2 - ie^{i\beta_3}|\lambda_{12}\lambda_{36}|Z_1Y_2 \\ L_2 &= L_5^\dagger = ie^{i(\beta_3-\beta_2)}|\lambda_{25}\lambda_{36}|Z_2 + ie^{i\beta_3}|\lambda_{23}\lambda_{36}|X_1Y_2 \qquad (4.89) \\ L_3 &= L_6^\dagger = i|\lambda_{12}\lambda_{23}|Y_1 + ie^{i(\beta_2-\beta_1)}|\lambda_{14}\lambda_{25}|Y_2 \\ &\qquad - ie^{-i\beta_1}|\lambda_{14}\lambda_{23}|X_1Z_2 + ie^{i\beta_2}|\lambda_{12}\lambda_{25}|Z_1X_2. \qquad (4.90) \end{aligned}$$

The coherent part in Eq. (4.88) is governed by the Hamiltonian

$$\tilde{H}_{\mathrm{L}} = 2pg_0L_z + \sum_{a=1}^{6} \bar{h}_a L_a^\dagger L_a, \tag{4.91}$$

with the operator

$$L_z = \sin\beta_1|\lambda_{12}\lambda_{14}|Z_1Z_2 + \sin\beta_2|\lambda_{23}\lambda_{25}|X_1X_2. \tag{4.92}$$

Comparing the above Lindbladian with the one for the two-box setup, cf. Eq. (4.74), one notices that all jump operators now stem from second-order cotunneling and thereby, the relevant energy scale is again $g_0 = \frac{t_0^2}{E_C}$, see Eq. (4.11). Therefore, the transition rates $\bar{\Gamma}_a$ and Lamb shifts $\bar{h}_a$ are given by Eq. (4.79) and Eq. (4.80) with $\tilde{g}_0 \to g_0$.

In analogy to Sec. 4.3.1, in the low temperature regime, i.e. for $T \ll \omega_0$, and in the regime $\frac{1}{2} < \alpha < 1$, the dominant contribution to the Lindblad equation originates from jump operators L_1 and L_2. To stabilise the system in the Bell singlet state $|\phi_-\rangle$, see Eq. (4.84), one chooses the state design parameters according to

$$\beta_1 = \frac{\pi}{2}, \quad \beta_2 = \frac{\pi}{2}, \quad \beta_3 = \pi, \quad |\lambda_{12}| = |\lambda_{14}|, \quad |\lambda_{23}| = |\lambda_{25}|. \tag{4.93}$$

It is then straightforward to check that $L_1 \propto \hat{E}_1 1,-$ and $L_2 \propto \hat{E}_{2,-}$, see Eq. (4.83), such that the dark state of the two-qubit system is indeed given by $|\phi_-\rangle$. The coherent part again does not obstruct the dissipative map. In contrast to the two-box case, the conditions in Eq. (4.93) ask for equal transparency for pairs of links, rather than having transparencies that parametrically differ by a factor $\lambda_{LR} = t_{LR}/E_C \ll 1$, see Sec. 4.1. As a consequence, the dissipative gap encountered for the hexon device is significantly larger,

$$\Delta_{\text{Bell,hex}} = |2\lambda_{3,6}|^2 \left(|\lambda_{12}|^2 + |\lambda_{23}|^2\right) \sum_{a=1,2,4,5} \bar{\Gamma}_a. \tag{4.94}$$

When compared to Δ_{Bell} in Eq. (4.94), one observes that this dissipative gap enjoys a large enhancement factor $1/\lambda_{LR}^2$. In fact, the dissipative gap (4.94) is of the same order as the gaps encountered for the single-box case. Using the hexon architecture, Bell states can thus be stabilised at about the same speed as the dark states in Sec. 4.2.

For the sake of completeness, the stabilisation conditions for the remaining Bell states are listed below. The $|\psi_\pm\rangle$ states are realised by changing the phases in Eq. (4.93) to $\beta_1 = -\pi/2$, $\beta_2 = \mp\pi/2$, and $\beta_3 = -\pi$. Furthermore, $|\phi_+\rangle$ will be stabilised for $\beta_1 = \pi/2$, $\beta_2 = -\pi/2$, and $\beta_3 = \pi$.

4.4 Driven dissipative Majorana dark spaces

In this section, it is shown that devices harbouring MBSs provide a particularly attractive platform for the DD stabilisation of degenerate dark spaces and for manipulating states in such spaces. As shown in Sec. 4.3.1, the dynamics in the Majorana sector is governed by a Lindblad equation, Eq. (4.52). In Sec. 4.4.1, this Lindbladian is used to demonstrate that the two-box system can be engineered to support a multi-dimensional degenerate dark space. The here discussed dark space is equivalent to a qubit space. To ensure that a generic initial state evolves towards a designated pure state within the dark space, one has to adiabatically break the degeneracy of the dark space during intermediate stages of the protocol. In Sec. 4.4.2 this is discussed as a paradigmatic protocol for the preparation of a state within a degenerate dark space. Additionally, this section contains information on how to optimise the speed of approach and the fidelity towards the designated dark space. Finally, Sec. 4.4.3 describes different ways of manipulating the dark state inside the dark space manifold. As initialisation, read-out, and manipulation are discussed in this section, one can view it as first step towards dark space quantum computation.

For recent experimental progress on autonomous error correction in different DD systems see also [Reiter, 2017] and [Puri, 2019].

4.4.1 Dark space stabilisation

As already indicated in Sec. 4.3, the two-box setup in Fig. 4.7 is sufficient to stabilise a dark space. Having a degenerate state manifold targeted by the DD protocol requires the Lindbladian to conserve more than one quantity, cf. Sec. 2.5.2. Therefore, the Lindblad master equation in Eq. (4.74) describes more dynamical processes than needed in this section. Conceptually, the stabilisation of a dark space is thus simpler compared to the stabilisation of maximally entangled states. For convenience, one therefore decouples QD 2 from the system by using the parameter choice

$$\lambda_{2,2L} = \lambda_{2,4R} = 0, \quad \beta_2 = 0. \tag{4.95}$$

Note that this is not the only possible parameter set for constructing a dark space. As a consequence of Eq. (4.95), many of the jump operators in Eq. (4.75) vanish identically, $K_2 = K_3 = K_5 = K_6 = 0$. The only jump operators left are then given by K_1 and K_4. At low temperatures, $T \ll \omega_0$, the ratios $\tilde{\Gamma}_4/\tilde{\Gamma}_1$ and $\tilde{h}_4/\tilde{h}_1$ are exponentially small, and therefore only the jump operator K_1 remains relevant. In analogy to Sec. 4.1, this operator can be traced back to unidirectional cotunneling transitions, where an electron is transferred from QD 3 to QD 1 by cotunneling through the double-box setup. In the steady state, a weak drive amplitude A is then responsible for pumping the dot electron back (from QD 1 → 2) via the driven tunnel link. Note that the parameters $A, \omega_0, \alpha, \omega_c$, and $\tilde{g}_0$ only affect the rates $\tilde{\Gamma}_n$ and Lamb shifts h_n, which in turn determine the speed of approach towards the dark space. The dark space itself, however, will be determined by the choice of the jump operator K_1, which can be engineered by tuning the state design parameters $\lambda_{j,\nu\kappa}$, see Eq. (4.75). These parameters can be adjusted via gate voltages. The ability to design jump operators via unidirectional cotunneling processes in such a manner is rooted in the non-local Majorana representation of the Pauli operators in Eq. (4.2), and thus in the underlying topological nature of the here discussed DD system.

Upon choosing the state design parameters according to

$$\beta_1 = -\pi, \quad \beta_3 = -\pi/2, \quad |\lambda_{1,1R}| = \lambda_{LR}|\lambda_{1,3L}|, \tag{4.96}$$

one can implement the dissipative map $\hat{E}_{1,-}$ in Eq. (4.83). Noting that $\hat{E}_{1,-} = X_R - iZ_L Y_R$, see Eq. (4.83), one indeed arrives at $K_1 \propto \hat{E}_{1,-}$ from Eq. (4.75). In addition, Eq. (4.76) shows that under the above conditions, $\tilde{H}_{\mathrm{L}}$ only generates terms $\propto Z_L Z_R$ which do not obstruct the dissipative dynamics. Following the procedure outlined in Sec. 2.5.3, one can identify four conserved quantities,

$$C_{1,\pm} = \frac{1}{2}(\mathbb{I} \pm Z_L), \quad C_{2,\pm} = \frac{1}{2}(X_L \pm iY_L)X_R. \tag{4.97}$$

The basis of the matrix Hilbert space corresponding to the dark space [Albert, 2014] then reads

$$M_{1,\pm} = \frac{1}{4}(\mathbb{I} \pm Z_L)(\mathbb{I} \mp Z_R), \quad M_{2,\pm} = \frac{1}{4}(X_L \pm iY_L)(X_R \mp iY_R). \tag{4.98}$$

The above DD protocol thus stabilises a degenerate dark space of dimension $D = 4$, where D is the number of conserved quantities in the matrix Hilbert space obtained after the Choi isomorphism, cf. Sec. 2.5.2. As this isomorphism maps an N-dimensional Hilbert space onto an N^2-dimensional matrix Hilbert space, $D = 4$ in turn coincides with the dark space dimension of a stabilised qubit space. This can also be rationalised by noting that $C_{2,+} = C_{2,-}^{\dagger}$ and $C_{1,+} + C_{1,-} = \mathbb{I}$.

The Pauli operators (X_D, Y_D, Z_D) for the resulting *dark Majorana qubit* can be chosen as

$$X_D = X_L X_R = -\gamma_1^L \gamma_3^L \gamma_1^R \gamma_3^R, \quad Y_D = Y_L X_R = \gamma_2^L \gamma_3^L \gamma_1^R \gamma_3^R, \quad Z_D = Z_L = i\gamma_1^L \gamma_2^L. \tag{4.99}$$

Alternative Majorana representations can be obtained by using $Z_L Z_R = -1$ and/or the above parity constraints on each box. Thereby, one can rewrite $X_D = -\gamma_2^L \gamma_4^L \gamma_2^R \gamma_4^R$ and $Y_D = -\gamma_1^L \gamma_4^L \gamma_2^R \gamma_4^R$. Note that the Majorana bilinear $i\gamma_4^L \gamma_2^R$ is essential for the above

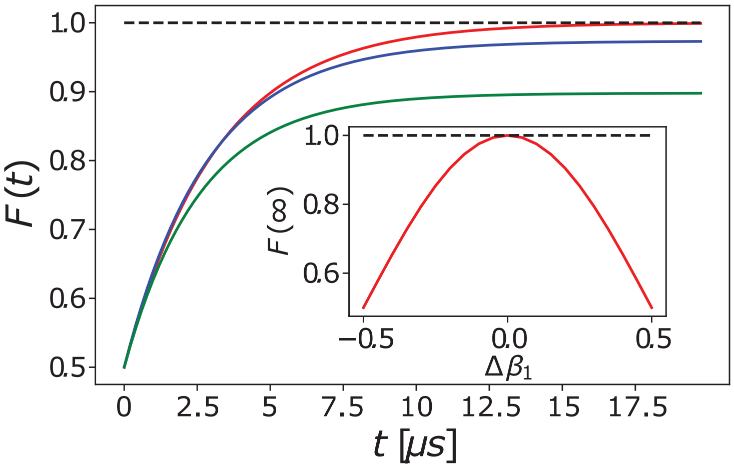

Figure 4.10: Fidelity for approaching the dark space starting from a maximally mixed initial state. Main panel: Fidelity vs time, with $E_C = 1$ meV, $\tilde{g}_0/E_C = 10^{-4}, T/\tilde{g}_0 = 2, \omega_0/\tilde{g}_0 = 200, \omega_c/\tilde{g}_0 = 10^3, \alpha = 0.99, p(A) = 0.01$, and $|\lambda_{2,3L}| = 1$. The red curve is for ideal state design parameters, see Eq. (4.96), with $|\lambda_{1,1R}| = 1$. The blue (green) curve depicts the fidelity for parameters with 10% (20%) deviation from their respective ideal values. Inset: Asymptotic ($t \to \infty$) fidelity vs percentage deviation $\Delta\beta_1$ from $\beta_1 = \pi$, with otherwise ideal parameters. [Gau, 2020a]

qubit encoding, which reflects the need of two boxes for the here discussed proposal. Therefore, the DD protocol effectively merges both tetrons and allows for the formation of a new qubit. The DD qubit encoding (4.99) is essential for fault tolerance, comparable to the formation of logical vs physical qubits in surface codes [Fowler, 2012]. In the here discussed case, the DD protocol adds an extra protection layer on top of the topological protection of a native Majorana qubit. In particular, pure states will thereby be stabilised for indefinite time.

Finally, methods for readout of the target state can be formulated as for the native Majorana qubit, see Sec. 4.2.5. By providing additional details on the approach of the dark space, the next subsection contains possible state initialisation protocols for the above dark Majorana qubit.

4.4.2 Approaching the dark space

Starting from an arbitrary initial state $\rho_{\mathrm{M}}(0)$, one can monitor the approach towards a pure target state $|\Psi\rangle$ in terms of the fidelity, $F(t) = \mathrm{tr}\left[|\Psi\rangle\langle\Psi|\rho_{\mathrm{M}}(t)\right]$, where $\rho_{\mathrm{M}}(t)$ is the solution of Eq. (4.52). During the time evolution, all symmetry properties of the initial state other than parity (Z_1Z_2) remain preserved. For example, starting with $\rho_{\mathrm{M}}(0) = |\psi_+\rangle\langle\psi_+|$, since $X_LX_R = +1$ is kept as one approaches the target state, one finds $|\Psi\rangle = |\phi_+\rangle$ within the dark space. In Fig. 4.10, we show the fidelity obtained by numerical integration of Eq. (4.52) for a maximally mixed initial state $\rho_{\mathrm{M}}(0) = \frac{1}{4}\mathbb{I} \otimes \mathbb{I}$, where the corresponding target state is $|\Psi\rangle = (|\phi_+\rangle + |\phi_-\rangle)/\sqrt{2}$. Note that if the initial state is not precisely known, one can first stabilise an arbitrary state inside the dark space, and subsequently drag that state towards the desired target state using the method described in Sec. 4.4.3. A convenient way to initialise the dark qubit is to employ the tunnel couplings to a third QD, see Sec. 4.3.2, and first stabilise a dark state. Afterwards, one can adiabatically switch off the tunnel couplings to QD 2 in Fig. 4.7 and stabilise the above discussed dark space. Figure 4.10 demonstrates that the dark-space fidelity is very robust against variations of the $\lambda_{j,\nu\kappa}$. Even when allowing for 'errors' of the order of 20% in all these parameters, the fidelity is still $F \approx 0.9$. The time scale for approaching the steady state is given by the inverse of the dissipative gap Δ_{diss}. For the above DD protocol, one again obtains $\Delta_{\text{diss}} \simeq |4\lambda_{1,3L}\lambda_{2,3R}|^2 \left(\tilde{\Gamma}_1 + \tilde{\Gamma}_4\right)$, resulting in $\Delta_{\text{diss}}^{-1} \approx 3$ μs for the parameters in Fig. 4.10. Comparing the characteristic time of approach for the dark space with the inverse of the Bell state gap, i.e. with $\Delta_{\text{Bell}}^{-1}$, one observes that the dark space is stabilised approximately 100-times faster. This nicely reflects the need to only map the Majorana states onto the odd-parity manifold, and thereby, avoid unwanted cotunneling processes connecting QD 1 and QD 2.

4.4.3 Manipulation of the dark Majorana state

Next, a general manipulation protocol is discussed, which allows to move an initial pure state in the dark space to an arbitrary final state in the dark space. This can be achieved by adiabatically switching on a perturbation, which breaks at least one conservation law in Eq. (4.97). Note that adiabaticity is crucial, because of the transient behaviour in the joint dynamics of the two boxes and the QDs. The perturbation breaks the qubit degeneracy during the protocol but once the perturbation is switched off, the degenerate dark space is fully stabilised again.

The main challenges are to avoid coupling the dark space to other Hilbert space sectors that are not part of the decoherence-free subspace, and to preserve the purity of the state. In particular, the drive should not connect odd- and even-parity sectors. One can guarantee this by only addressing the 'outer' MBSs involved in the dark Majorana qubit encoding, see Eq. (4.99). It is convenient to break two conserved quantities at any given time, leaving a two-fold degeneracy. The simplest protocol employs a 'Z_L-drive' realised by coupling γ_1^L and γ_2^L, see Eq. (4.99). One thus adds a term

$$\mathcal{H}_Z = iA_Z(t)\gamma_1^L\gamma_2^L = A_Z(t)Z_L. \tag{4.100}$$

The hybridisation energy $A_Z(t)$ can be adiabatically changed using a gate-tunable tunnel link. $\mathcal{H}_Z$ commutes with Z_LZ_R and thus conserves parity. Therefore, the evolution generated by $\mathcal{H}_Z$ automatically remains in the odd-parity sector. Since $[\mathcal{H}_Z, C_{2,\pm}] \neq 0$, see Eq. (4.97), dark state coherences now depend on time. This is confirmed by the numerical results for constant A_Z in Fig. 4.11, where one starts from $\rho_{\text{M}}(0) = |\phi_-\rangle\langle\phi_-|$ and finds oscillations in the real part, $\langle X_D(t)\rangle = \langle X_LX_R\rangle(t)$, and the imaginary part, $\langle Y_D(t)\rangle = \langle Y_LX_R\rangle(t)$, of the coherences. In the Bloch vector representation, the dark state periodically rotates in the xy-plane with oscillation period A_Z^{-1}, where $A_Z^{-1} \approx 6$ ns in Fig. 4.11. For a general adiabatic protocol $A_Z(t)$, it stands to reason that an arbitrary final state inside the dark space can be reached.

An alternative possibility is to employ single-electron pumping protocols, in analogy to previous proposals for native Majorana qubits, see Sec. 2.4.3.

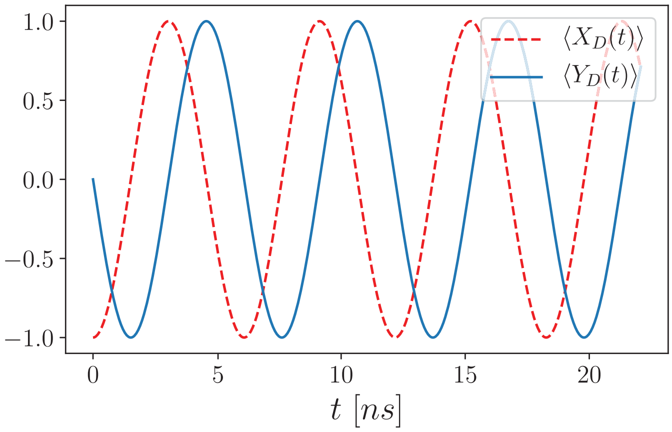

Figure 4.11: State manipulation by a Z_L-drive with $A_Z/E_C = 10^{-4}$. The state design parameters are chosen as in in Eq. (4.96) and other parameters are as in Fig. 4.10. The dynamics of the expectation values of the Pauli operators (4.99) reveals oscillatory qubit coherences. At all times, one numerically finds $\langle Z_D\rangle = 0$ and, of course, $\langle Z_L Z_R\rangle = -1$ (odd parity). [Gau, 2020a]

4.5 Summary

In this chapter, Majorana-based DD protocols for stabilising as well as manipulating dark states and dark spaces are described. The underlying topological nature of the Majorana states significantly boosts the power of DD schemes in several directions. First, the role of uncontrolled environmental noise sources should be suppressed compared to topologically trivial realisations, which is a key advantage for high-dimensional dark space constructions. Second, the fact that Pauli operators describing native Majorana qubits correspond to products of Majorana operators (pertaining to spatially separated MBSs) allows for unique addressability options. Only through this feature, which is rooted in its topology, it is possible to design the special unidirectional cotunneling paths, which directly implement the jump operators appearing in the Lindblad equation.

For devices with one or two Majorana boxes coupled to driven QDs and subject to electromagnetic noise, it was shown that the dynamics in the Majorana sector is accurately described by Lindblad master equations in a wide parameter regime, cf. Sec. 4.1. For a single-box architecture, Sec. 4.2 provided how to stabilise arbitrary pure dark states, i.e. states that are fault tolerant and stable on arbitrary time scales. Interestingly, the discussed DD stabilisation protocol is robust against detuning of state design parameters, temperature, and in some cases also a small Majorana hybridisation is tolerable. For multiple-box devices, one can also stabilise dark spaces, i.e. manifolds of degenerate dark states, as well as protected two-qubit Bell states, cf. Sec. 4.3. In Sec. 4.4 it was shown that a two-box device allows one to implement a dark Majorana qubit, which in turn could serve as basic ingredient for dark space quantum computation schemes. The here discussed stabilisation and manipulation protocols can be implemented with available hardware elements once a working Majorana platform becomes available.

Chapter 5

Summary and outlook

Within this chapter the thesis is briefly summarised starting with the fundamental principles. Furthermore, this chapter contains the contribution of the included publications to the Majorana field. Afterwards an outlook is given, where especially the driven dissipative Majorana box opens up various directions for further investigation.

In chapter 2, the Majorana basics were discussed. After an introduction to Majorana fermions, the Kitaev chain and its nanowire construction were considered. Charging effects allow to address the non-locally encoded quantum information by electron transport. Furthermore, charge quantisation significantly simplifies the representation of Majorana operators in terms of Pauli operators. Additionally, general techniques for studying quantum transport in a single Majorana island were introduced. For more than three Majorana bound states on a single box, phase-coherent transport facilitates the topological Kondo effect. As the here discussed Majorana boxes are key for Majorana-based quantum computers, chapter 2 also included the fundamentals of Majorana qubits and a discussion in terms of the criteria for quantum computation. Even though the quantum information stored on Majorana devices is topologically protected, natural dephasing mechanisms require active error correction. Finally, this chapter gave insight on the derivation of Lindblad master equations and different techniques to study such equations of motion.

Chapter 3 generalised the transport results for a single island to more complex systems. Here, the theoretical framework was established to study arbitrary coupled box systems, which might be used for future research. Consequently, [Gau, 2018] systematically described different coupled Majorana box systems, where different Majorana-lead junctions were emphasised. By coupling leads to Majorana islands in a non-simple fashion, one can intentionally create spins, which are non-locally distributed over boxes and leads. Furthermore, it revealed that for coupled systems attached to leads, the latter host strongly-correlated states, which can be probed by their exotic low-energy physics. This included quantum transport resonances and unconventional Kondo effects. This work was the first to study transport through coupled boxes, which could become essential once a working Majorana platform is available.

In chapter 4, the Majorana box was revisited in the context of an open quantum system. By carefully engineering the drive, one can benefit from the dissipation due to the electromagnetic environment, which is always present in experiments. Thereby, [Gau, 2020b] introduced a drive and dissipation cycle, which allows for the stabilisation of Majorana states for indefinite time. Comparing the performance of drive and dissipation protocols for Majorana boxes with protocols with non-topological building blocks, reveals that the

Majorana-based platform is superior. This is rooted in the spatial distribution of drive and dissipation, which in turn is based on the topology of the box. The proposed dark state stabilisation is also stable against temperature fluctuations and does not require a highly fine-tuned setup, which might become important for future experimental realisations. A coupled box setup allows to stabilise a degenerate state manifold, a dark space, which harbours a dark Majorana qubit. As shown in [Gau, 2020a], such a qubit is not only topologically protected, but also state manipulations experience an additional protection mechanism. Therefore, it stands to reason that based on the here discussed proposals, one can construct Majorana platforms allowing for quantum computing schemes without active feedback. Whereas state initialisation, manipulation, and read-out are discussed in chapter 4, there are several potential directions that allow for further investigation.

The above concepts and ideas raise many interesting perspectives for future research. First, one expects that one can devise robust Majorana braiding protocols, which are stabilised by working within a dark space manifold. Second, for chains of many boxes, DD stabilisation protocols may allow for interesting quantum simulation applications, e.g. a realisation of the topologically non-trivial ground state of spin ladders [Ebisu, 2019] or of the Affleck-Kennedy-Lieb-Tasaki (AKLT) spin chain [Kraus, 2008, Affleck, 1987]. Third, for superconducting qubits driven dissipative schemes and active error correction reinforce each other, [Liu, 2016], and thereby, optimise the stabilisation protocol. For the driven dissipative Majorana box one can envision similar effects, where the active error correction capabilities might come in handy when going to large-scale systems. Finally, the stabilisation of a dark space allows to study problems of fundamental interest. One could discuss several dark space manipulations allowing for the study of geometrical phases, [Snizhko, 2019], adiabatic conditions, or the optimisation of fidelity and purity, while performing rotations within the protected space.

List of publications

Here, the included publications will be listed and a short description of the contribution to the research will be given.

QUANTUM TRANSPORT IN COUPLED MAJORANA BOX SYSTEMS, PUBLISHED 16 MAY 2018 IN PHYSICAL REVIEW B

In this project, quantum transport in coupled Majorana box systems attached to normal leads is investigated. My contributions include the modelling of such box systems and the formulation of an effective low-energy theory allowing for further investigation. Here, I performed the above described Schrieffer-Wolff transformations, Abelian bosonisation and Majorana-Klein fusion techniques. Moreover, I derived the weak-coupling RG equations for arbitrary coupled systems and contributed to the numerical solution of those flow equations, where I found various conserved quantities and observed different flows towards isotropy, which allowed for the study of the strong-coupling regime. I was involved in the establishment of the strong-coupling theory by means of performing Emery-Kivelson-type rotations and studying different Toulouse points. Furthermore, I numerically analysed the transport equations and was responsible for all plotted results.

Reference: Matthias Gau, Stephan Plugge, and Reinhold Egger, *Quantum transport in coupled Majorana box systems*, Phys. Rev. B **97**, 184506 (2018). [Selected as *Editors' Suggestion*]

DRIVEN DISSIPATIVE MAJORANA DARK SPACES, SUBMITTED TO PHYSICAL REVIEW LETTERS, 30 MARCH 2020

In this project, driven dissipative Majorana box devices are shown to stabilise dark spaces, which are beneficial for quantum computing purposes. My contributions include the derivation of the Lindblad master equation for a two-box device. Furthermore, I studied the Lindbladian by means of calculating its spectrum and by discussing conserved quantities and thereby, symmetries of the open quantum system. The latter, I used to analytically find the dark space and write down an appropriate basis allowing for further investigation. I introduced different manipulation protocols and discussed how to initialise predesignated states within the dark space. Moreover, I performed all numerical calculations.

Reference: Matthias Gau, Reinhold Egger, Alex Zazunov, and Yuval Gefen, *Driven Dissipative Majorana Dark Spaces*, preprint arXiv:2003.13295 (2020)

TOWARDS DARK SPACE STABILIZATION AND MANIPULATION IN DRIVEN DISSIPATIVE MAJORANA PLATFORMS, SUBMITTED TO PHYSICAL REVIEW B, 31 MARCH 2020

This project contains details of driven dissipative Majorana platforms, where the main result is the stabilisation of topologically protected single- or two-qubit states for indefinite time. I was involved in the creation of a quantum dot based proposal, where the dissipation arises by tunneling between box and dot. Additionally, I modelled such systems and performed all required calculations in order to obtain an effective low-energy theory allowing for the derivation of a dynamical equation. Furthermore, I derived the Lindblad master equation for single- and two-box systems, and found that one can simplify the Lindbladian by additionally tracing over the quantum dots in a rather simple fashion. Moreover, I studied the spectrum of all obtained Lindblad master equations, and carried out various symmetry-based discussions allowing for the analytical study of different dark state stabilisations. All of the analytical results were augmented by numerical calculations, which were exclusively performed by me.

Reference: Matthias Gau, Reinhold Egger, Alex Zazunov, and Yuval Gefen, *Towards dark space stabilization and manipulation in driven dissipative Majorana platforms*, preprint arXiv:2003.13979 (2020)

Bibliography

Affleck, I., T. Kennedy, E.H. Lieb, and H. Tasaki (1987), Phys. Rev. Lett. **59**, 799.

Affleck, I., A.W.W. Ludwig, and B.A. Jones (1995), Phys. Rev. B **52**, 9528.

Aharonov, Y., and D. Bohm (1959), Phys. Rev. **115**, 485.

Albrecht, S.M., A.P. Higginbotham, M. Madsen, F. Kuemmeth, T.S. Jespersen, J. Nygård, P. Krogstrup, and C.M. Marcus (2016), Nature **531**, 206.

Alicea, J., Y. Oreg, G. Refael, F. von Oppen, and M.P.A Fisher (2011), Nature Phys. **7**, 412.

Alicea, J. (2012), Rep. Prog. Phys. **75**, 076501.

Albert, V. and L. Jiang (2014), Phys. Rev. A **89**, 022118.

Albert, V., B. Bradlyn, M. Fraas, and L. Jiang (2016), Phys. Rev. X **6**, 041031.

Altland, A. and B. Simons (2010), *Condensed Matter Field Theory*, 2nd ed. (Cambridge University Press).

Altland, A. and R. Egger (2013), Phys. Rev. Lett. **110**, 196401.

Altland, A., B. Béri, R. Egger, and A.M. Tsvelik (2014), Phys. Rev. Lett. **113**, 076401.

Avignone, F.T., S.R. Elliott, and J. Engel (2008), Rev. Mod. Phys. **80**, 481.

Bardyn, C.E., M.A. Baranov, C.V. Kraus, E. Rico, A. İmamoĝlu, P. Zoller, and S. Diehl (2013), New. J. Phys. **15**, 085001.

Barreiro, J. T., M. Müller, P. Schindler, D. Nigg, T. Monz, M. Chwalla, M. Hennrich, C.F. Roos, P. Zoller, and R. Blatt (2011), Nature **470**, 486.

Beenakker, C.W.J. (2013), Annu. Rev. Con. Mat. Phys. **4**, 113.

Béri, B. and N.R. Cooper (2012), Phys. Rev. Lett. **109**, 156803.

Béri, B. (2013), Phys. Rev. Lett. **110**, 216803.

Béri, B. (2017), Phys. Rev. Lett. **119**, 027701.

Bonderson, P., and C. Nayak (2013), Phys. Rev. B **87**, 195451.

Breuer, H.-P. and F. Petruccione (2006), *The Theory of Open Quantum Systems* (Oxford University Press).

Bruus, H., and K. Flensberg (2016), *Many-Body Quantum Theory in Condensed Matter Physics: An Introduction* (Oxford University Press).

Deng, M.T., S. Vaitiekenas, E.B. Hansen, J. Danon, M. Leijnse, K. Flensberg, J. Nygård, P. Krogstrup, and C.M. Marcus (2016), Science **354**, 1557.

Deng, M.T., S. Vaitiekénas, E. Prada, P. San-Jose, J. Nygård, P. Krogstrup, R. Aguado, and C.M. Marcus (2018), Phys. Rev. B **98**, 085125.

Devoret, M.H., D. Esteve, H. Grabert, G.-L. Ingold, H. Pothier, and C. Urbina (1990), Phys. Rev. Lett. **64**, 1824.

Diehl, S., A. Micheli, A. Kantian, B. Kraus, H.P. Büchler, and P. Zoller (2008), Nat. Phys. **4**, 878.

Diehl, S., E. Rico, M.A. Baranov, and P. Zoller (2011), Nat. Phys. **7**, 971.

DiVincenzo, D.P (2000), Fortschr. Phys. **48**, 771.

Ebisu, H., E. Sagi, and Y. Oreg (2019), Phys. Rev. Lett. **123**, 026401.

Emery, V.J. and S. Kivelson (1992), Phys. Rev. B **46**, 10812.

Fabrizio, M., A.O. Gogolin, and Ph. Nozières (1995), Phys. Rev. B **51**, 16088.

Flensberg, K. (2011), Phys. Rev. Lett. **106**, 090503.

Fowler, A. G., M. Mariantoni, J.M. Martinis, and A.N. Cleland (2012), Phys. Rev. A **86**, 032324.

Fu, L. (2010), Phys. Rev. Lett. **104**, 056402.

Gardiner, C. and P. Zoller (2004), *Quantum Noise: A Handbook of Markovian and Non-Markovian Quantum Stochastic Methods with Applications to Quantum Optics* (Springer Verlag).

Gau, M., S. Plugge, and R. Egger (2018), Phys. Rev. B **97**, 184506.

Gau, M., R. Egger, A. Zazunov, and Y. Gefen, arXiv:2003.13295

Gau, M., R. Egger, A. Zazunov, and Y. Gefen, arXiv:2003.13979

Gazibegovic, S., D. Car, H. Zhang, S.C. Balk, J.A. Logan, M.W.A. de Moor, M.C. Cassidy, R. Schmits, D. Xu, G. Wang, P. Krogstrup, R.L.M. Op het Veld, J. Shen, D. Bouman, B. Shojaei, D. Pennachio, J.S. Lee, P.J. van Veldhoven, S. Koelling, M.A. Verheijen, L.P. Kouwenhoven, C.J. Palmstrøm, and E.P.A.M. Bakkers (2017), Nature **548**, 434.

Girvin, S.M., L.I. Glazman, M. Jonson, D.R. Penn, and M. D. Stiles (1990), Phys. Rev. Lett. **64**, 3183.

Gogolin, A.O., A.A. Nersesyan, and A.M. Tsvelik (2004), *Bosonization and Strongly Correlated Systems* (Cambridge University Press).

Gogolin, A.O. and A. Komnik (2006), Phys. Rev. B **73**, 195301.

Goldman, N., J.C. Budich, and P. Zoller (2016), Nat. Phys. **12**, 639.

Herviou, L., K. Le Hur, and C. Mora (2016), Phys. Rev. B **94**, 235102.

Hützen, R., A. Zazunov, B. Braunecker, A. Levy Yeyati, and R. Egger (2012), Phys. Rev. Lett. **109**, 166403.

Hyart, T., B. van Heck, I.C. Fulga, M. Burrello, A.R. Akhmerov, and C.W.J. Beenakker (2013), Phys. Rev. B **88**, 035121.

Jayaprakash, C., H. R. Krishna-murthy, and J. W. Wilkins (1981), Phys. Rev. Lett. **47**, 737.

Johansson, J.R., P.D. Nation, and F. Nori (2012), Comp. Phys. Comm. **183**, 1760.

Johansson, J.R., P.D. Nation, and F. Nori (2013), Comp. Phys. Comm. **184**, 1234.

Jones, B.A., C.M. Varma, and J.W. Wilkins (1988), Phys. Rev. Lett. **61**, 125.

Karzig, T., C. Knapp, R.M. Lutchyn, P. Bonderson, M.B. Hastings, C. Nayak, J. Alicea, K. Flensberg, S. Plugge, Y. Oreg, C.M. Marcus, and M.H. Freedman (2017), Phys. Rev. B **95**, 235305.

Kashuba, O. and C. Timm (2015), Phys. Rev. Lett. **114**, 116801.

Kitaev, A.Y. (2001), Usp. Fiz. Nauk (Suppl) **171**, 131.

Kraus, B., H. P. Büchler, S. Diehl, A. Kantian, A. Micheli, and P. Zoller (2008), Phys. Rev. A **78**, 042307.

Landau, L.A., S. Plugge, E. Sela, A. Altland, S. M. Albrecht, and R. Egger (2016), Phys. Rev. Lett. **116**, 050501.

Landau, L.A., E. Cornfeld, and E. Sela (2017), arXiv:1710.03030.

Leghtas, Z., U. Vool, S. Shankar, M. Hatridge, S.M. Girvin, M.H. Devoret, and M. Mirrahimi (2013), Phys. Rev. A **88**, 023849.

Leijnse, M. and K. Flensberg (2012), Semicond. Sci. Techn. **27**, 124003.

Lindblad, G. (1976), Comm. Math. Phys. **48**, 119.

Lindblad, G. (1983), *Nonequilibrium Entropy and Irreversibility* (D. Reidel Pub. Co.).

Litinski, D., M.S. Kesselring, J. Eisert, and F. von Oppen (2017), Phys. Rev. X **7**, 031048.

Liu, Y., S. Shankar, N. Ofek, M. Hatridge, A. Narla, K.M. Sliwa, L. Frunzio, R.J. Schoelkopf, and M.H. Devoret (2016), Phys. Rev. X **6**, 011022.

Lutchyn, R.M., J.D. Sau, and S. Das Sarma (2010), Phys. Rev. Lett. **105**, 077001.

Lutchyn, R.M., E.P.A.M. Bakkers, L.P. Kouwenhoven, P. Krogstrup, C.M. Marcus, and Y. Oreg (2018), Nat. Rev. Mater. **3**, 52

Majorana, E. (1937), Il Nuovo Cimento **14** (4), 171.

Manousakis, J., C. Wille, A. Altland, R. Egger, K. Flensberg, and F. Hassler (2020), Phys. Rev. Lett. **124**, 096801.

Michaeli, K., L.A. Landau, E. Sela, and L. Fu (2017), Phys. Rev. B **96**, 205403.

Mourik, V., K. Zuo, S.M. Frolov, S.R. Plissard, E.P.A. Bakkers, and L.P. Kouwenhoven (2012), Science **336**, 1003.

Munk, M.I.K., R. Egger, and K. Flensberg (2019), Phys. Rev. B **99**, 155419.

Nayak, C., M.P.A. Fisher, A.W.W. Ludwig, and H.H. Lin (1999), Phys. Rev. B **59**, 15694.

Nayak, C., S.H. Simon, A. Stern, M. Freedman, and S. Das Sarma (2008), Rev. Mod. Phys. **80**, 1083.

Nazarov, Yu. V. and Ya. M. Blanter (2010), *Quantum Transport: Introduction to Nanoscience,* (Cambridge University Press).

Nichele, F., A.C.C. Drachmann, A.M. Whiticar, E.C.T. O'Farrell, H.J. Suominen, A. Fornieri, T. Wang, G.C. Gardner, C. Thomas, A.T. Hatke, P. Krogstrup, M.J. Manfra, K. Flensberg, and C.M. Marcus (2017), Phys. Rev. Lett. **119**, 136803.

Nielsen, M.A. and I.L. Chuang (2010), *Quantum Computation and Quantum Information* (Cambridge University Press).

Oreg, Y., G. Refael, and F. von Oppen (2010), Phys. Rev. Lett. **105**, 177002.

Platero, G. and R. Aguado (2004), Phys. Rep. **395**, 1.

Plugge, S., A. Zazunov, E. Eriksson, A.M. Tsvelik, and R. Egger (2016a), Phys. Rev. B **93**, 104524.

Plugge, S., L. A. Landau, E. Sela, A. Altland, K. Flensberg, and R. Egger (2016b), Phys. Rev. B **94**, 174514.

Plugge, S., A. Rasmussen, R. Egger, and K. Flensberg (2017), New J. Phys. **19**, 012001.

Puri, S., A. Grimm, P. Cammpagne-Ibarcq, A. Eickbusch, K. Noh, G. Roberts, L. Jiang, M. Mirrahimi, M.H. Devoret, and S.M. Girvin (2019), Phys. Rev. X **9**, 041009.

Read, N., and D. Green (2000), Phys. Rev. B **61**, 10267.

Reiter, F., A.S. Sørensen, P. Zoller, and C.A. Muschik (2017), Nat. Comm. **8**, 1822.

Romito , A. and Y. Gefen, Phys. Rev. B **90**, 085417 (2014).

Shavit, G., B. Horovitz, and M. Goldstein (2019), Phys. Rev. B **100**, 195436.

Snizhko, K., R. Egger, and Y. Gefen (2019), Phys. Rev. Lett. **123**, 060405.

Terhal, B.M. (2015), Rev. Mod. Phys. **87**, 307.

Touzard, S., A. Grimm, Z. Leghtas, S.O. Mundhada, P. Reinhold, C. Axline, M. Reagor, K. Chou, J. Blumoff, K.M. Sliwa, S. Shankar, L. Frunzio, R.J. Schoelkopf, and M.H. Devoret (2018), Phys. Rev. X **8**, 021005.

Weiss, U. (2007) *Quantum Dissipative Systems*, 4th ed. (World Scientific).

Yi, H. and C.L. Kane (1998), Phys. Rev. B **57**, R5579(R).

Yi, H. (2002), Phys. Rev. B 65, 195101.

Zazunov, A., A. Levy Yeyati, and R. Egger (2011), Phys. Rev. B **84**, 165440.

Zazunov, A., A. Altland, and R. Egger (2014), New J. Phys. **16**, 015010.

Zazunov, A., R. Egger, and A. Levy Yeyati (2016), Phys. Rev. B **94**, 014502.

Zhang, H., C.X. Liu, S. Gazibegovic, D. Xu, J.A. Logan, G. Wang, N. van Loo, J.D.S. Bommer, M.W.A. de Moor, D. Car, R.L.M. Op het Veld, P.J. van Veldhoven, S. Koelling, M.A. Verheijen, M. Pendharkar, D.J. Pennachio, B. Shojaei, J.S. Lee, C.J. Palmstrom, E.P.A.M. Bakkers, S. Das Sarma, and L.P. Kouwenhoven (2018), Nature **556**, 74.

Acknowledgements

The first person I would like to thank is my supervisor Prof. Dr. Reinhold Egger, who guided me through all phases of my academic life. I am deeply grateful for his useful advice, patience, his exceptional reachability for answering questions via email from places all over the world, and, most of all, for giving me the chance to do my PhD under his watch and for him making possible an extended stay at the Weizmann Institute of Science.

Secondly, I would like to thank PD Dr. Hermann Kampermann for becoming the second referent for my thesis, for being my mentor during all of my PhD, and for all his lectures on advanced quantum information theory.

Furthermore, I would like to thank Prof. Dr. Yuval Gefen for his council, patience, and for welcoming me during an extended stay in Israel. I am deeply grateful for the discussions with him, and for always taking time for me, even if being on vacation or at a conference in an exotic country.

I would like to thank all present and former members of Institut für Theoretische Physik IV at HHU. My gratitude goes to Dr. Alex Zazunov and Dr. Stephan Plugge for working with me on our projects, Dr. Francesco Buccheri for helpful discussions, and my office neighbours Kathrin and Albert for always lending a sympathetic ear to me. Especially, I would like to thank Dr. Laura Hagmeister for her good advice during my Bachelor and Master, and for rendering the start of my PhD even more enjoyable.

I appreciate all the friends I got to know in the last 8 years at HHU and I am thankful for the friends I have made long before starting at the university - I would not want to miss your amity. Special thanks go to Fiona Grüll, who not only started with me 8 years ago, but has accompanied me ever since - thank you for sharing the struggles of academic life.

I would like to thank my parents for always supporting me and giving me the freedom to be whatever I wanted to be for as long as I can remember. And at last but very definitely not least, I would like to thank Maureen Kluth for her invaluable support within the last years. I would not have been able to do this without you!

Selbstständigkeitserklärung

Ich versichere an Eides Statt, dass die Dissertation von mir selbständig und ohne unzulässige fremde Hilfe unter Beachtung der „Grundsätze zur Sicherung guter wissenschaftlicher Praxis an der Heinrich-Heine-Universität Düsseldorférstellt worden ist.
Weiterhin erkläre ich, dass ich die Dissertation keiner anderen Fakultät bereits vorgelegt habe und keinerlei vorherige erfolglose oder erfolgreiche Promotionsversuche vorliegen.
Darüber hinaus ist mir bekannt, dass jedweder Betrugsversuch zum Nichtbestehen oder zur Aberkennung der Prüfungsleistung führen kann.

Ort, Datum	Unterschrift